Distortional Buckling Formulation for the Analysis of Composite thin-walled beams

MohammadHossein Moradpoor Sheikhkanloo

A Thesis

in

The Department

of

Building, Civil and Environmental Engineering

Presented in Partial Fulfillment of the Requirements

for the Degree of Master of Applied Science (Civil Engineering) at

Concordia University

Montréal, Québec, Canada

November 2021

CONCORDIA UNIVERSITY
School of Graduate Studies

This is to certify that the thesis prepared

By: MohammadHossein Moradpoor Sheikhkanloo

Entitled: Distortional Buckling Formulation for the Analysis of Composite thin-walled beams

and submitted in partial fulfillment of the requirements for the degree of

MASc Civil Engineering

complies with the regulations of the University and meets the accepted standards with respect to originality and quality.

Signed by the final examining committee:

Dr. Lucia Tirca Chair

Dr. Ghazanfarah Hafeez Examiner

Dr. Lucia Tirca Examiner

Dr. Emre Erkmen Thesis Supervisor(s)

Approved by Dr. Mazdak Nik-Bakht
Chair of Department or Graduate Program Director

Dr. Mourad Debbabi
Dean Gina Cody School of Engineering and Computer Science

Abstract

Distortional Buckling Formulation for the Analysis of Composite thin-walled beams

MohammadHossein Moradpoor Sheikhkanloo, M.A. Sc.

Thin-walled beams are widely used in construction with various restraint arrangements and sizes. While lateral torsional buckling is a major design concern for thin-walled beams used as girders distortional effects may become important depending on restraint conditions as well as for beams with slender webs, stocky flanges, and/or shorter spans. This thesis introduces a novel beam-type nonlinear Finite Element formulation that is applicable for the analysis of I-sections that are prone to lateral-torsional buckling and distortion. A linearized buckling formulation has been derived as a special case of the nonlinear beam formulation under the assumption of no pre-buckling deformations. The material is assumed elastic. The formulation was also applied for composite laminated thin-walled beams. The effect of shear deformation on the flexural and lateral-torsional buckling predictions of composite-laminated thin-walled beams were illustrated without the distortional effects. For the analysis of composite-laminated thin-walled beams the finite element formulation has the flexibility to choose one of the alternative members of the Doyle-Ericksen family of strains. As such the developed formulation is an extension of both Engesser and Haringx column buckling formulas to shear deformable thin-walled beams with rigid webs. It is shown that alternative strain definitions lead to changes in the geometric stiffness matrices in finite element buckling analysis of thin-walled beams. The effect of the selected strain definition on the elastic buckling load predictions is illustrated in numerical tests including short sections and beams with low shear modulus.

To my beloved parents,

Araz Mohammad & Zohreh

Acknowledgments

I would like to begin by expressing my deepest gratitude to my supervisor, Dr. Emre Erkmen for his valuable guidance and suggestion, creative and critical thinking based on his extensive knowledge and research experience throughout this research work.

I am also thankful to the members of my thesis proposal committee; Dr. Lucia Tirca, and Dr. Ghazanfarah Hafeez for their thoughtful advice and encouragement.

I am extending my highest appreciations to my dear parents, ArazMohammad and Zohreh for their endless love and immense support for educating and preparing me for my future. I am truly blessed to have such wonderful parents. Thank you, my two lifelines!

I express my special thanks to my beloved sisters, Dr. Nona Moradpoor, Dr. Naghmeh Moradpoor, and Neda, my adorable niece Sophie, and my lovely nephews Houman and Homayoun for their unconditional love and valuable devotions.

Last but not least, I would like to say thanks to my dear friends, Ahmad Kalantari, Mohammadreza Rejali, Reihaneh Tamizkar, Robbie McDowall, and Mahyar Erfani for their encouragement and moral support.

Table of Contents

List of Figures

List of Tables

1. Chapter 1: Introduction

1.1. General View

Thin-walled beam structures constituted from connecting thin plates are extensively used in many fields such as civil construction because of their high stiffness to weight ratios. Thin-walled members can be defined as members with large depth to thickness ratio i.e., $\frac{d}{t} \geq 10$ (Figure 1.1). A number of theories were developed for the analysis of the behavior of the thin-walled members which are elaborated in section 1.4. Thin-walled beams with open cross-sections such as I-shaped wide flange beams suffer from inherently low torsional stiffness and therefore they are prone to several elastic buckling modes depending on their size and restraint conditions. Lateral-torsional buckling of steel joists is a major concern in building design while in bridge design girders of composite beam are prone to distortion of their web due to restraint conditions. Distortional effects gain significance in girder beams with slender webs, stocky flanges, and/or shorter spans. Shear deformation also becomes important as the beam spans get relatively short comparison to cross-sectional sizes. For safe and economical design modelling approaches that capture necessary modes of deformation for accurate analyses of thin-walled beams are required.

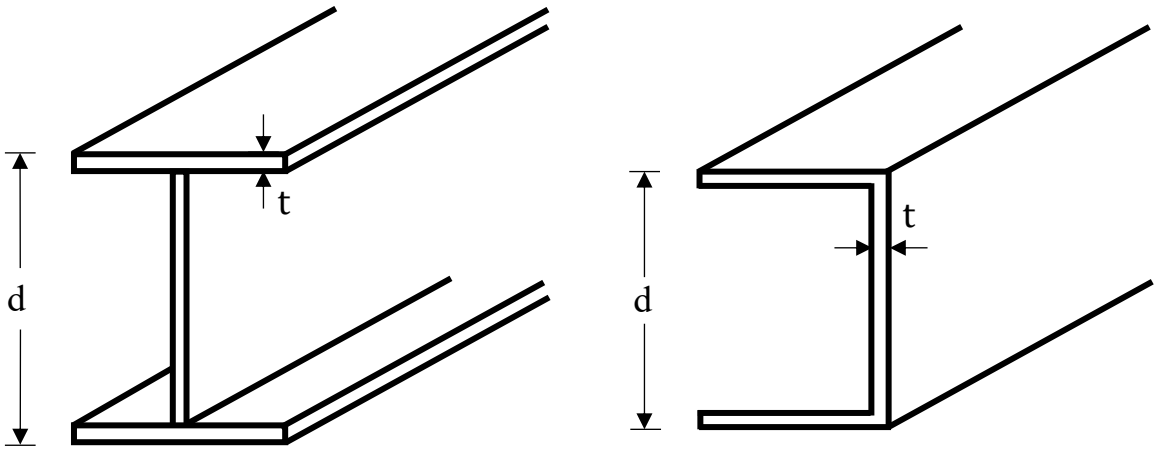

Figure 1.1 Thin-walled members with open cross-section

1.2. Motivation

The primary objective of the current thesis is to capture the effect of web distortion which is neglected in conventional beam theories plus considering the incorporation of shear deformation effects in buckling and static analysis of wide flange beams given that such effects can be eminent

in cross-sections with deep-slender webs. Therefore, it is rational to develop a computer program for numerical modelling thin-walled beams able to perform buckling analysis.

Developing a finite element formulation capable for a reliable elastic buckling behavior in steel structures incorporates the effects of web distortion which have commonly been neglected in buckling solutions. Adopting classical approaches in buckling analysis which ignore distortional effects on the cross-section were observed overpredict the buckling capacity of the member leading to unconservative buckling response predictions. A linearized buckling eigenvalue analysis is conducted to obtain critical load of thin-walled steel beams and results are verified with shell analysis model.

1.3. Thesis Organization

The current thesis presented a new finite element formulation for thin-walled members with open cross-section to predict their elastic buckling resistance which captures web distortional effects in order to avoid limitations in the conventional beam theories for static and buckling analysis. The present chapter includes introduction and provides a review of fundamental concepts of thin-walled beam kinematics and contains a literature review conducted on web flexibility.

Chapter 2 describes the beam kinematics and related displacement fields and correspondent first order and second order strain tensor in the buckling stages.

Chapter 3 the differential equilibrium equations for the condition of neutral stability for buckling consistent with the kinematics are developed based on the principle of virtual work.

Chapter 4 the finite element formulation for distortional beam as a treatment for classical approaches (rigid web assumption) is explained and expressions for the nodal displacements vector are presented. Additionally, finite element formulation for thin-walled beam with non-bendable web is represented as a special case for non-distortional buckling.

Chapter 5 the validity of the formulations is assessed for static analysis of a mono-symmetric cross-section throughout solving numerical examples and comparison with results based on shell FEA and thin-walled models, and other conventional beam solutions is conducted as well.

Chapter 6 several examples are provided to investigate the effect of web bending on buckling analysis of doubly symmetric sections incorporation thin-walled beam formulation which neglects

cross-sectional distortion to address the limitations of classical solutions and comparisons are provided against shell FEA solutions to verify the presented theory.

Chapter 7 is written in a paper format with its standalone literature review, a unified finite element formulation is developed for shear deformable FRP pultruded thin-walled beams with low shear modulus. In this chapter, however, the distortional effects are suppressed due to some complications of combining shear deformability with distortions effects in buckling analysis.

1.4. Theory of thin-walled members

1.4.1. Beam theories kinematics

This section is reviewing a few important bending theories for beams by describing their kinematic assumptions, related displacement fields and correspondent strains expressions. A right-handed coordinate system (x, y, z) is designated (see Figure 1.2), where z is directed along the longitudinal axis of the beam, the x axis is along the width of the beam, and the y axis is along the height of the beam which is considered positive in a downward direction. The corresponding displacement fields along the three axes of x, y, z are u, v, and w, respectively. Subsequently, the kinematics of deformation and displacement fields for various theories for steel beams such as Euler-Bernoulli, Timoshenko, Higher-order beams, Vlasov are presented.

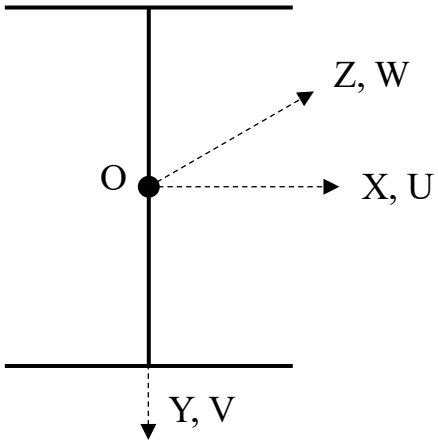

Figure 1.2 Right-handed coordinate system

1.4.2. Euler-Bernoulli Beam Theory

The Euler-Bernoulli beam theory or classical beam theory is the simplest beam theory for analysis of thin-walled structural components. This theory is developed on the basis of two primary assumptions:

- Cross-section of a beam remains planar and normal to the neutral axis of the beam after the beam deforms.
- Deformed angles (slopes) of the beam are assumed small.

According to the first assumption it can be seen that the angle of rotation of the cross-section and the slope angle of the neutral axis $\left({}^{dv}/_{dx}\right)$ are equal to each other (see Figure 1.3), and corresponding displacement fields can be written as below:

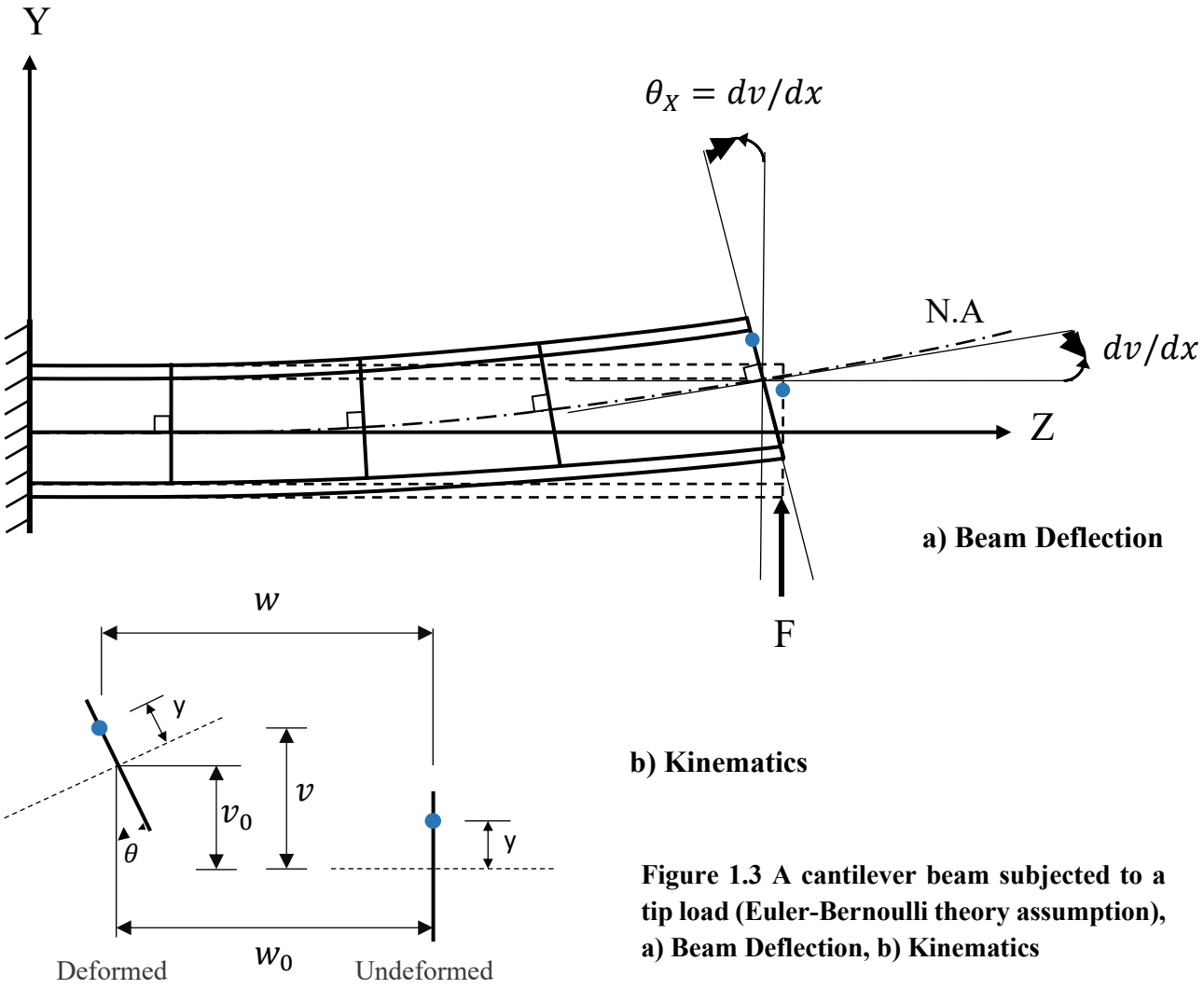

Figure 1.3 A cantilever beam subjected to a tip load (Euler-Bernoulli theory assumption), a) Beam Deflection, b) Kinematics

$$u(x,y,z) = 0 \qquad 1.1$$

$$w(x,y,z) = w_0(z) - y\sin\theta$$

$$v(x,y,z) = v_0(z) + y\cos\theta - y$$

Where $u(x,y,z)$, $w(x,y,z)$ and $v(x,y,z)$ are the displacement fields of an arbitrary point on a cross-section along x, z, and y directions, respectively, and $w_0(z)$ and $v_0(z)$ is the longitudinal and transvers displacement of a point on the beam centroidal axis located at (0, 0, z). Simultaneously, θ_X denotes the angle of rotation of the cross-section which is equal to the slope of the neutral axis ($\theta_X = dv/dx$).

According to the assumption of small deformation, we have

$$\cos\theta \approx 1$$

$$\sin\theta \approx \theta$$

Therefore, the equation 1.1 can be simplified as:

$$\begin{aligned} u(x,y,z) &= 0 \\ w(x,y,z) &= w_0(z) - y\theta = w_0(z) - yv_0{}' \\ v(x,y,z) &= v_0(z) \end{aligned} \qquad 1.2$$

The corresponding normal and shear strains can be written as below:

$$\begin{aligned} \varepsilon_{xz} &= \frac{1}{2}\left(\frac{\partial u}{\partial z} + \frac{\partial w}{\partial x}\right) = 0 \\ \varepsilon_{yz} &= \frac{1}{2}\left(\frac{\partial v}{\partial z} + \frac{\partial w}{\partial y}\right) = 0 \\ \varepsilon_{zz} &= \frac{\partial w}{\partial z} = -yv_0{}'' \end{aligned} \qquad 1.3$$

Furthermore, the bending moment about x axis due to the applied tip load can be calculated in terms of displacements as $\int ydF$, and based on the Hook's law $\sigma_{zz} = E\varepsilon_{zz}$, in which E refers to elasticity modulus:

$$M_x = \int ydF = \int_A y(\sigma_{zz}dA) = \int_A E\varepsilon_{zz}ydA = E\int_A(-yv_0{}'')ydA = -EI_xv_0{}'' \qquad 1.4$$

Where I_x and A are the second moment of inertia about x axis and area of the cross-section, respectively.

The shear internal force cannot be calculated from kinematics because it will lead to zero, and must be found from equilibrium equation:

$$Q_y = \int_A \tau_{yz} dA = \int_A (G\varepsilon_{yz}) dA = 0 \qquad 1.5$$

In Euler-Bernoulli beam theory, the shear deformation effects are completely ignored which states that the centroidal axis of the beam remains perpendicular to the cross-section after the deformations, and this can result in a stiffer behavior against those theories which include effects of shear deformation.

1.4.3. Timoshenko Beam Theory

Numerous investigations have been conducted by researchers for developing beam theories by including effect of shear deformation and rotary inertia which were the main limitations of the Euler-Bernoulli beam theory. Timoshenko [1] introduced a shear correction factor as a function of the shape of the cross-section as a treatment of the Euler-Bernoulli beam theory. He presumed that plane section remains plane, but normality condition between the cross-section and centroidal axis of the beam is relaxed (see Figure 1.4). Thus, due to considering the shear deformation effects, the angle of rotation of the cross-section is not equal to the slope of the neutral axis ($\theta_X \neq dv/dx$). Based on the kinematic assumptions of the Timoshenko beam theory, displacement fields can be expressed as

$$u(x, y, z) = 0 \qquad 1.6$$

$$w(x, y, z) = w_0(z) - y \sin\theta_X = w_0(z) - y\theta_X$$

$$v(x, y, z) = v_0(z)$$

In the above equations, θ_X is the rotation angle of the cross-section about the axis of bending, and $u(x, y, z)$, $w_0(z)$ and $v_0(z)$ are the lateral, longitudinal and vertical displacements terms.

And the normal and shear strain components can be written as:

$$\varepsilon_{xz} = \frac{1}{2}\left(\frac{\partial u}{\partial z} + \frac{\partial w}{\partial x}\right) = 0 \qquad 1.7$$

$$\varepsilon_{yz} = \frac{1}{2}\left(\frac{\partial v}{\partial z} + \frac{\partial w}{\partial y}\right) = \frac{1}{2}(v_0{}' - \theta_X)$$

$$\varepsilon_{zz} = \frac{\partial w}{\partial z} = -y\theta_X{}'$$

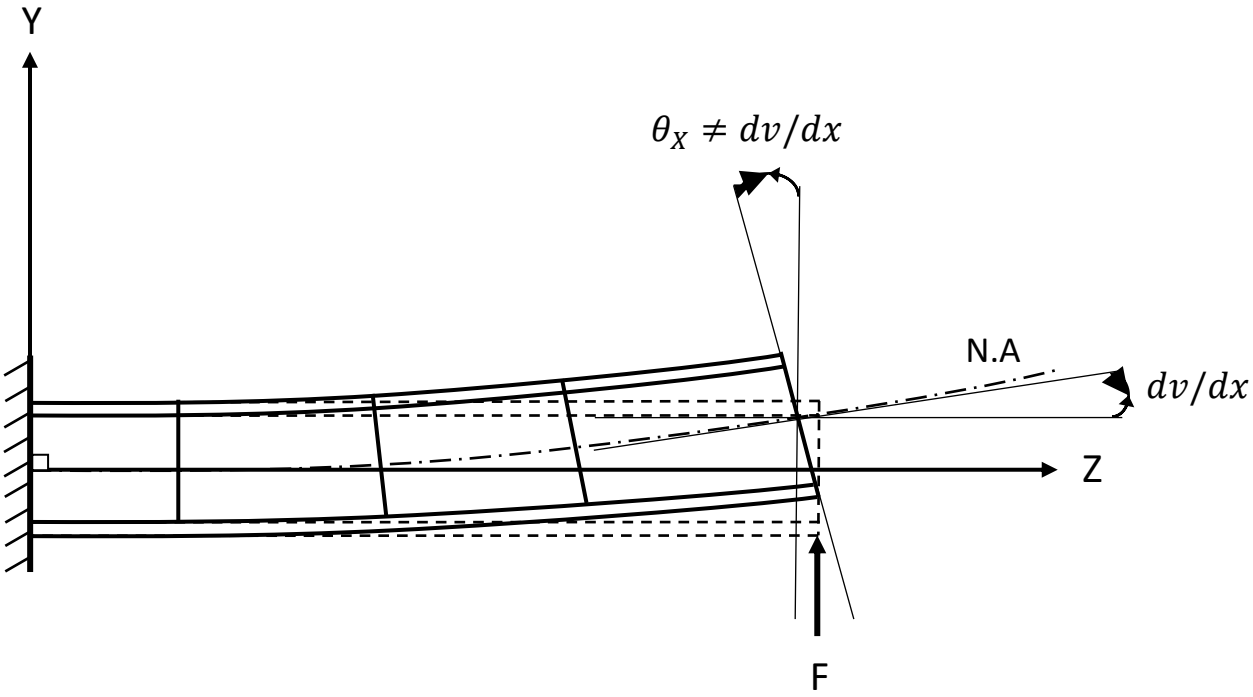

Figure 1.4 A cantilever beam subjected to a tip load (Timoshenko theory assumption)

The bending moment can be determined by the integration of normal stress of the area of the cross-section, and considering the Hook's law $\sigma_{zz} = E\varepsilon_{zz}$ as blow:

$$M_x = \int ydF = \int_A y(\sigma_{zz}dA) = \int_A E\varepsilon_{zz}ydA = E\int_A (-y\theta_X{}')ydA = -EI_x\theta_X{}' \qquad 1.8$$

Alternatively, many researchers calculated different values for the shear coefficient (e.g., Mindlin and Deresiewicz [3], Cowper [4], Reddy [5]) in order to predict more accurate response for the beam behaviors for engineering purposes. Therefore, the internal shear force over the area can be found as below:

$$Q_y = \int_A \tau_{yz}dA = \int_A k_s\left(G\varepsilon_{yz}\right)dA = k_sGA(v_0{}' - \theta_X) \qquad 1.9$$

Where A is the area of the cross-section, G is the elastic shear modulus and k_s is the shear correction factor as an approximate modification for traction boundary conditions (e.g., Batoz [10], Pilkey [7]) can be evaluated by:

$$k_s = \frac{A}{I_x^2}\int_A \left(\frac{S_x}{t}\right)^2 dA \qquad 1.10$$

Where t is the thickness and S_x is the first moment of area of the cross-section.

Generally, Timoshenko beam's theory shows more flexibility which means larger deflection comparison to Euler-Bernoulli beam. However, according to ε_{yz} in equation 1.7, the shear strain is distributed uniformly over the cross-section of the beam and the correspondent constant shear stress distribution which are not zero at the top and bottom surface of the beam. As a result, Timoshenko beam theory violates the traction boundary conditions at the top edge and bottom edge of the beam. Hence, to remedy this limitation and having more accurate kinematic assumption, higher order beam theory was developed to satisfy traction boundary conditions which will be discussed in the next section.

1.4.4. Higher-order Beam Theory

Shear deformation in Timoshenko beam is first order, and shear strain is constantly distributed along the beam's height which implies that the shear stress at the top and bottom surface of the beam does not vanish and that violates the shear stress-free boundary conditions at the top and bottom surface of the beam. Higher order shear deformation beam theory has been introduced by many researchers to remedy the limitation of first order shear deformation to get the zero-shear stress at the top and bottom surface of the beam. In higher order beam theory, nonlinear shear strain variation along the depth of the beam causes the cross-section to warp. As a result, not only the normality condition between the centroidal axis and the section is relaxed, but also the plane section will not remain plane after deformation.

It is interesting to note that in the mentioned higher order beam theories the transverse shear strain is distributed parabolically along the thickness of the plates, and in order to satisfy the shear free boundary conditions on the surfaces of the plate the longitudinal displacement of the beam take a cubic distribution. The assumed displacement fields can be written as below:

$$u(x,y,z) = 0 \tag{1.11}$$

$$w(x,y,z) = w_0(z) + y\theta_X(z) + y^3\psi(z)$$

$$v(x,y,z) = v_0(z)$$

And $\psi(z)$ which represent warping function can be obtained as:

$$\psi(z) = -(\frac{4}{3h^2})\left[\theta_X(z) + \frac{dv}{dx}\right] \tag{1.12}$$

Thus, the longitudinal displacement in the equation 1.11 is simplified as below:

$$w(x,y,z) = w_0(z) + y\theta_X(z) - (\frac{4y^3}{3h^2})\left[\theta_X(z) + \frac{dv}{dx}\right] \tag{1.13}$$

Where $\theta_X(z)$ and h represent the angle of rotation about bending axis and height of the cross-section, respectively. Also, the corresponding normal and shear strain components are:

$$\varepsilon_{xz} = \frac{1}{2}\left(\frac{\partial u}{\partial z} + \frac{\partial w}{\partial x}\right) = 0 \tag{1.14}$$

$$\varepsilon_{yz} = \frac{1}{2}\left(\frac{\partial v}{\partial z} + \frac{\partial w}{\partial y}\right) = \frac{1}{2}\left(1 - \frac{4y^2}{h^2}\right)(\theta_X + v_0{}')$$

$$\varepsilon_{zz} = \frac{\partial w}{\partial z} = y\left(1 - \frac{4y^2}{3h^2}\right)\theta_X{}' - \frac{4y^3}{3h^2}v_0{}''$$

Which ε_{yz} implies the quadratic distribution of the shear strain and the correspondent shear stresses which will vanish at the top and bottom surfaces of the beam $\left(y = \pm\frac{h}{2}\right)$. Hence, there is no need for shear correction factor in higher order beam theory. However, these developments are only for beams with rectangular cross-sections.

The bending moment can be determined directly by integration of the normal stresses $\sigma_{zz} = E\varepsilon_{zz}$ over the cross-sectional area A as:

$$M_x = \int \sigma_{zz} y dA = \int E\varepsilon_{zz} y dA = E\int \left[\left(y^2 - \frac{4y^4}{3h^2}\right)\theta_X{}' - \frac{4y^4}{3h^2}\right] v_0{}'' dA \qquad 1.15$$

$$= \frac{4}{5} EI_x \theta_X{}' - \frac{1}{5} EI_x v''$$

The internal shear force can be expressed as (Reddy [5]):

$$Q_y = \int_A \tau_{yz} dA - \frac{4}{h^2}\int_A \tau_{yz} y^2 dA + \frac{4}{3h^2}\int_A \frac{d\sigma_{zz}}{dz} y^3 dA \qquad 1.16$$

$$= \int_A \tau_{yz}\left(1 - \frac{4}{h^2} y^2\right) dA + \frac{4}{3h^2}\int_A y^3 \frac{d\sigma_{zz}}{dz} dA$$

$$= G\left(A - \frac{28}{5h^2} I_x\right)(\theta_X + v_0{}') + \frac{EI_x}{21}(\theta_X{}'' + v_0{}''')$$

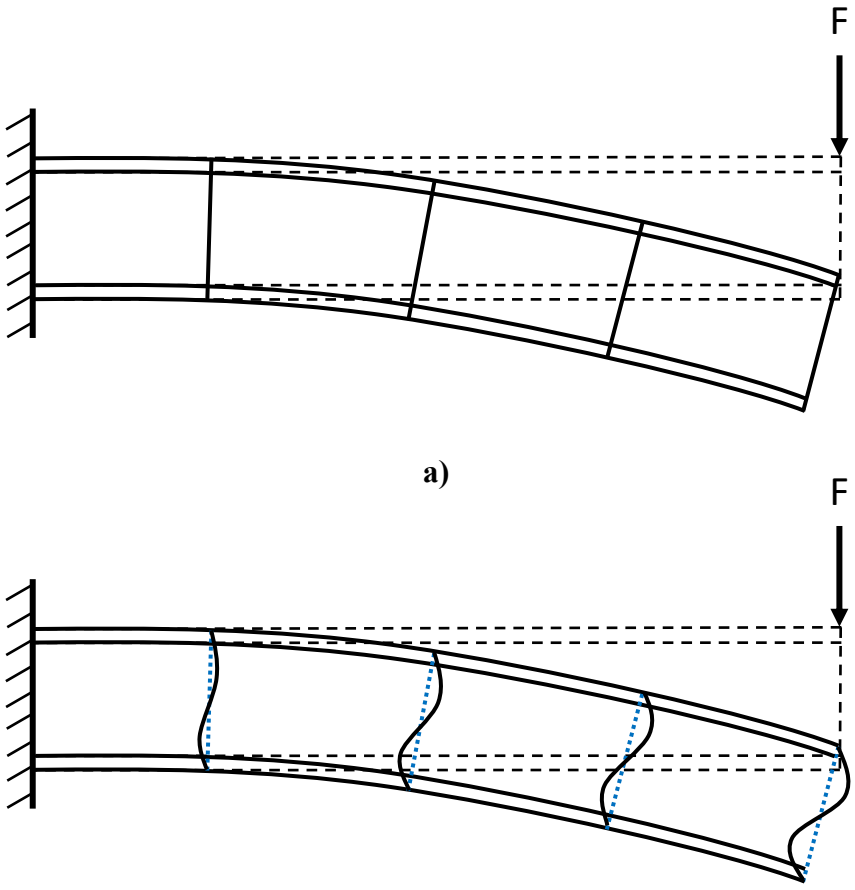

Figure 1.5 Deflection of a cantilever beam under a tip load, a) Without cross-sectional warping (Plane section remains plane), b) With cross-sectional warping (Plane section will not remain plane)

Figure 1.5 represents the major discrepancy between the deformed shape of the cross-section according to the elementary beam theories (e.g., Euler-Bernoulli and Timoshenko) and the higher order beam theory (e.g., Levinson [6], Bickford [8], and Heyliger and Reddy [9]). As illustrated, Figure 1.5a it is demonstrated that based on the elementary beam theories the plane section remains plane during the deformation, while in Figure 1.5b it can be observed that the plane section does not remain plane during the deformation and the longitudinal displacement of the plane section is non-uniform because of cross-sectional warping effect.

1.4.5. Thin-walled members under torsion

When a thin-walled member which is free to warp is subjected to opposite external torques at each end, the member undergoes uniform twisting along its longitudinal axis (z) which is passing through the shear center of the cross-section $S\ (x_s,\ y_s)$ under the assumption of the plane section will remain plane after the torques applied. This type of torsional behavior of a beam is known as pure torsion which was initially developed by Saint Venant and it is commonly the predominant behavior in beams with closed cross-sections such as circular hollow sections where the shear stresses distributed linearly through the thickness of the wall with zero value on the middle surface (see Figure 1.6).

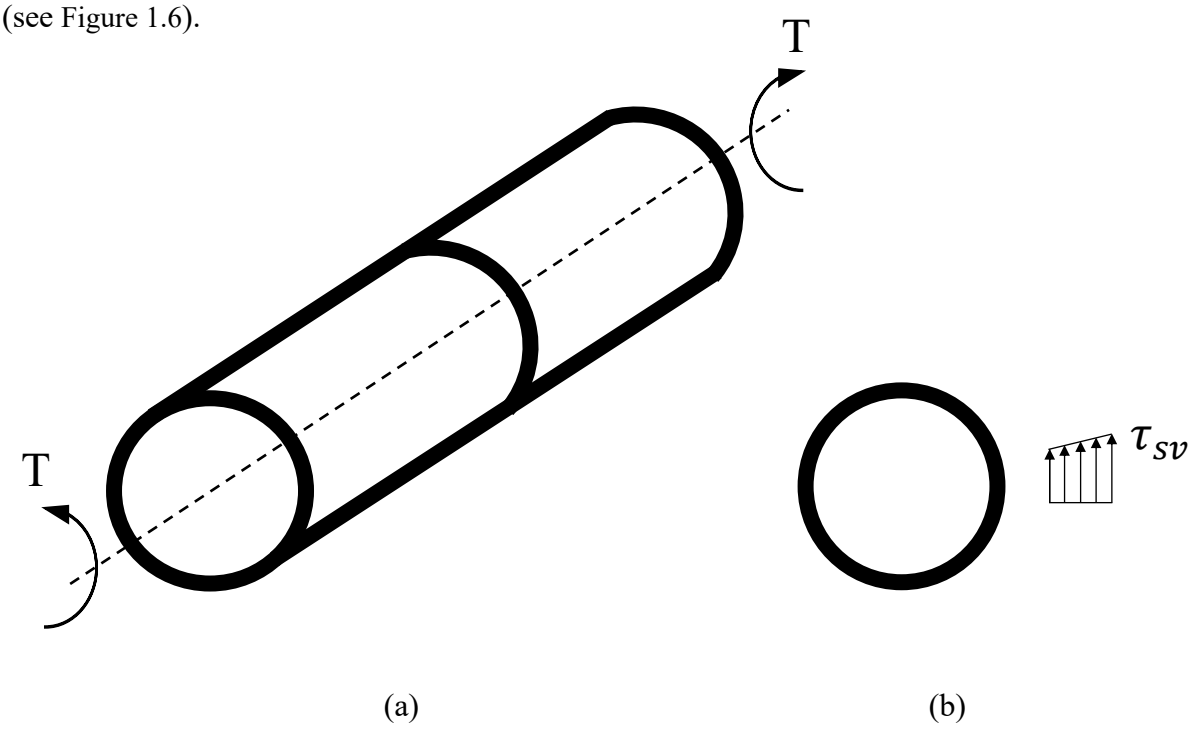

Figure 1.6 (a) A thin-walled member with closed cross-section under pure torsion, (b) Saint Venant's shear stress variation along the thickness

Based on the uniform torsion (Saint Venant) assumptions, the expression of the displacement field is:

$$u(x,y,z) = -(y - y_s)\theta_z(z) \tag{1.17}$$

$$w(x,y,z) = -\omega(x,y)\theta_z'$$

$$v(x,y,z) = (x - x_s)\theta_z(z)$$

Where $\omega(x,y)$ is the warping function and θ_z is the angle of twist which is linear. Therefore, the axial displacement $(\omega(x,y)\theta_z')$ is constant with respect to z. The strain components deduced from displacement field can be written as:

$$\varepsilon_{xz} = \frac{1}{2}\left(\frac{\partial u}{\partial z} + \frac{\partial w}{\partial x}\right) = \frac{1}{2}\left(y_s - y - \frac{\partial \omega}{\partial x}\right)\theta_z'(z) \tag{1.18}$$

$$\varepsilon_{yz} = \frac{1}{2}\left(\frac{\partial v}{\partial z} + \frac{\partial w}{\partial y}\right) = \frac{1}{2}\left(x - x_s - \frac{\partial \omega}{\partial y}\right)\theta_z'(z)$$

$$\varepsilon_{zz} = \frac{\partial w}{\partial z} = 0$$

The normal strain (ε_{zz}) and normal stress (σ_{zz}) of the cross-section vanish since the second derivative of the twist angle $(\theta_z''(z))$ is zero.

Based on the elastic and isotropic materials assumptions, the internal torque T_{SV} due to the applied torques can be calculated as

$$T_{SV} = \int_A \left[\tau_{yz}(x - x_s) - \tau_{xz}(y - y_s)\right] dA \tag{1.19}$$

Where shear stresses are $\tau_{yz} = G(2\varepsilon_{yz})$ and $\tau_{xz} = G(2\varepsilon_{xz})$, so the above equation can be simplified in terms of strain components as below:

$$T_{SV} = G\int_A \left[2\varepsilon_{yz}(x-x_s) - 2\varepsilon_{xz}(y-y_s)\right] dA \qquad 1.20$$

$$= G\theta_z'(z)\int_A \left[\left(x - x_s - \frac{\partial\omega}{\partial y}\right)(x-x_s) - \left(y_s - y - \frac{\partial\omega}{\partial x}\right)(y-y_s)\right] dA$$

$$= G\theta_z'(z)\int_A \left[(x-x_s)^2 + (y-y_s)^2 - (x-x_s)\frac{\partial\omega}{\partial y} + (y-y_s)\frac{\partial\omega}{\partial x}\right] dA$$

In which G is the shear modulus, J is the Saint Venant torsional constant which can be found as (Saade [11])

$$J = \int_A \left[(x-x_s)^2 + (y-y_s)^2 - (x-x_s)\frac{\partial\omega}{\partial y} + (y-y_s)\frac{\partial\omega}{\partial x}\right] dA \qquad 1.21$$

Consequently, by substituting equation 1.21 into equation 1.20, the Saint Venant's internal torque can be obtained as

$$T_{SV} = GJ\theta_Z' \qquad 1.22$$

1.4.6. Vlasov open thin-walled beam theory (non-uniform torsion)

In contrast to closed cross-sections, when a torque applied to a thin-walled beam with open cross-section, the member twisted non-uniformly and the distribution of the angle of twist $\theta_z(z)$ is not linear anymore like the uniform torsion which gives rise to non-uniform longitudinal displacements called warping of the plane section. If the cross-section is restrained at some locations along the member to warp out of its plane, then it will induce normal warping stress $\sigma_\omega$and shear warping stress τ_ω along the beam. These stresses due to restrained warping should be considered in addition to bending stresses in the combined torsional flexural analysis of thin-walled members. Hence, the torsional moment is consisting of two parts, one induced by Saint Venant torsion (T_{SV}) and the other by warping torsion (T_W). The effect of warping restrained due to non-uniform torsion for a doubly symmetric wide flange beam is depicted in Figure 1.7.

$$T = T_{SV} + T_W \qquad 1.23$$

$$T_W = -EI_w\theta_Z'''$$

$$T = GJ\theta_Z' - EI_w\theta_Z'''$$

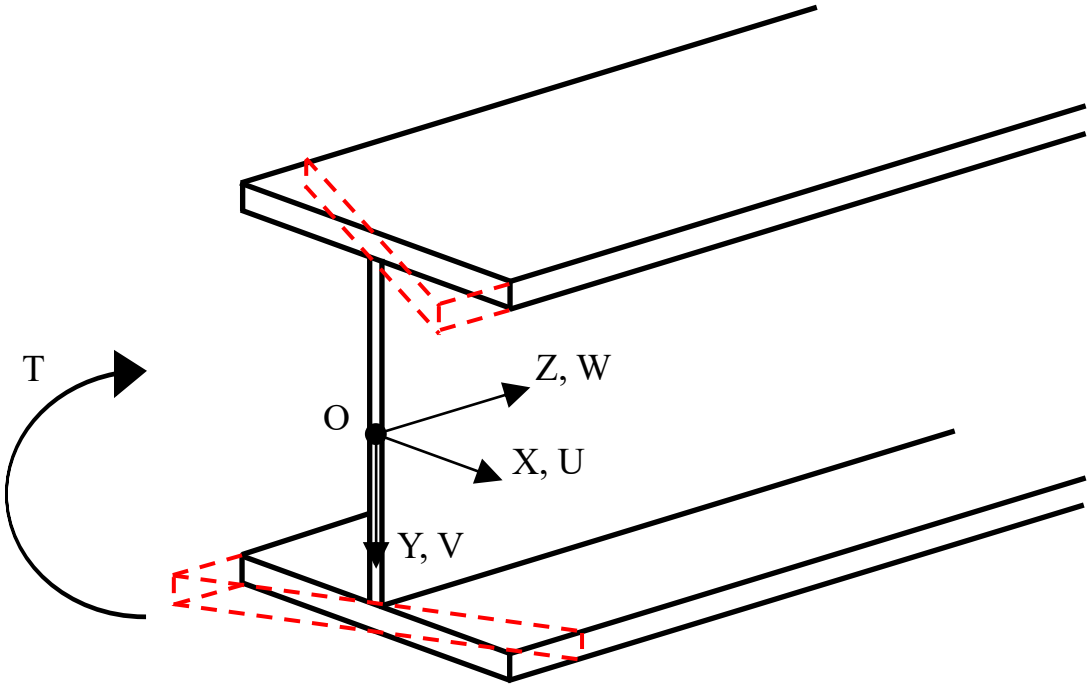

(a)

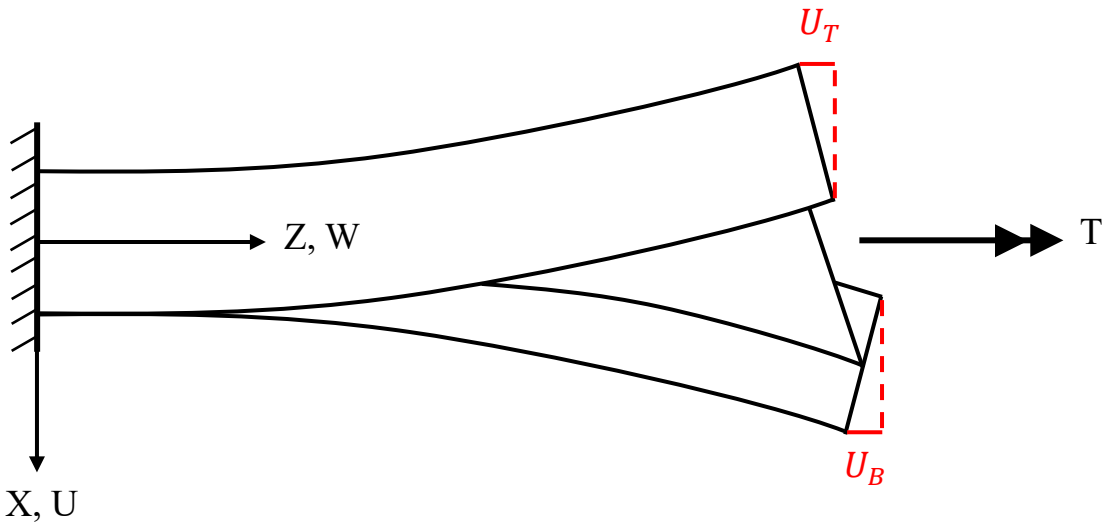

(b)

Figure 1.7 Global warping deformation of doubly symmetric I-shaped wide flange section, (a) Longitudinal displacements of the flanges, (b) Cantilever beam under torsion (restrained warping)

Where GJ is related to torsional stiffness and I_w is the warping constant and EI_w is known as the warping rigidity of the cross-section.

Vlasov [2] presented the simplest theory for prismatic thin-walled beams with open sections under the combination of flexure and torsion. His theory is based on 2 fundamental principles:

1) Every point on a given cross-section undergo the same angle of twist and the section acts as a rigid disk in its own plane.

2) The shear strains can be assumed to be equal to zero at the middle surface of the beam's cross-section.

As depicted in Figure 1.8, a doubly symmetric I-shaped beam undergoes deformation and rotates around z axis θ_z. The origin O is chosen on the centroid of the cross-section which is coincide with the shear center. According to the Vlasov assumptions, the displacement fields of any generic point on the middle surface of the thin-walled segment can be expressed in terms of the shear center displacements u_0, v_0 along x and y axis, and θ_z which is the angle of twist through

$$u(x,y,z) = u_0(z) - y\theta_z(z) \tag{1.24}$$

$$w(x,y,z) = w_0(z) - xu_0'(z) - yv_0'(z) - \bar{\omega}(x,y)\theta_z'(z)$$

$$v(x,y,z) = v_0(z) + x\theta_z(z)$$

Where $\bar{\omega}(x,y)$ is the global warping function due to twisting of the cross-section which caused by twisting of the section and can be calculated as $\bar{\omega}(x,y) = xy$. As a result of restrained warping, the twisting of the cross-section will induce each flange to bend about its local strong axis in opposite directions, one bends clockwise and the other one counterclockwise. Hence, both flanges move laterally, and in opposite signs, this pair of moments induced by warping restrained known as bimoment or moment couple (see Figure 1.7). This torsional-warping behavior of the beam give rises to warping constant which is a section property and can be defined as $I_w = \int \bar{\omega}^2 dA$.

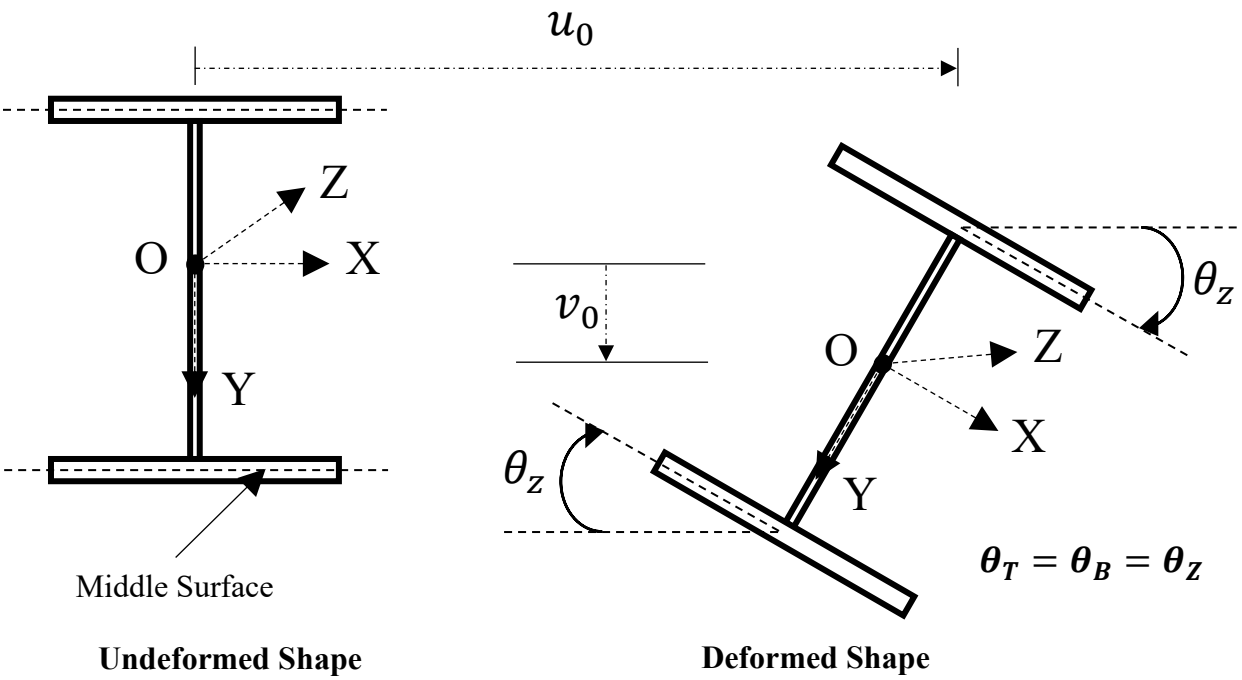

Figure 1.8 Vlasov's theory kinematics (rigid disk movement)

While Vlasov covered the out-of-plane displacements of the cross-section called warping induced by twisting of the member but neglected possible distortional effects on the cross-section which can be significant for beams with short spans, slender webs and stocky flanges. As depicted in Figure 1.8, when the cross-section undergoes deformation the top and bottom flanges have the same angle of twist θ_z, however; in reality, for many cases especially those with slender web and stocky flanges, the web has a tendency to bend in its own plane, so the angle of twist of the top flange differs from the angle of twist of the bottom flange (see distortional buckling configuration in Figure 1.9). Hence, ignoring web distortion can lead to inaccurate results in stability problems.

1.5. Gjelsvik thin-walled beam theory

Gjelsvik [12] pursued the Vlasov theory assumptions besides considering another kinematic assumption which is thickness warping function (secondary warping) when the thickness of the plates constituted the cross-section (web and flanges) increased, so local warping effects should be taken to account. Moreover, his hypothesis obeys the Kirchhoff theory of plates assumption whereby a straight line initially normal to the mid-surface remaining normal to the mid-surface after deformation. Hence, as the elements of the cross-section become thicker, each flange can

move out of its own plane. This behavior is captured in Gjelsvik theory as local warping effects of the section. As depicted in Figure 1.9, For a wide flange beam, two corners of the flange move in the longitudinal direction of the beam referring to Z axis here, and the other two corners move in the opposite direction. A right-handed local coordinate system (s, t) is introduced, and the origin of the coordinate system is at a generic point located on the middle surface of the segment where s is the coordinate along the mid-surface and t is along the thickness of the wall.

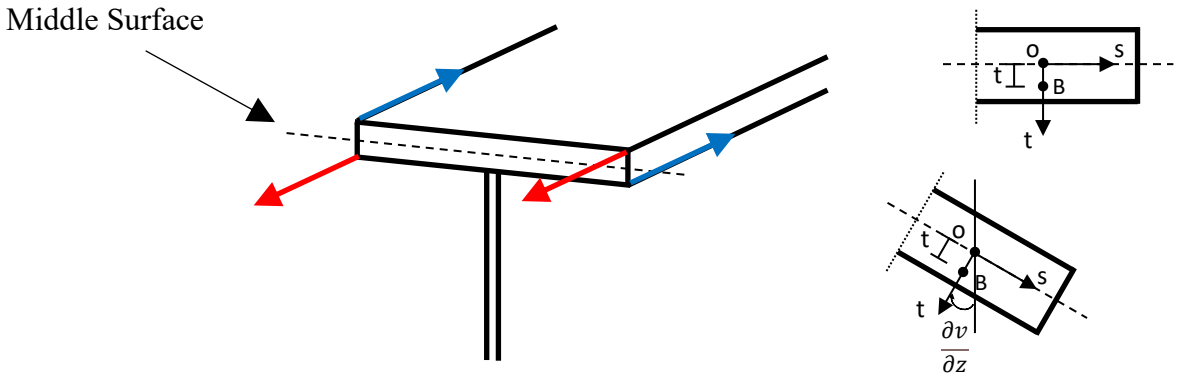

Figure 1.9 Local warping deformation of the flange (Gjelsvik theory)

For a doubly symmetric I-shaped section s coordinate is along the x global axis for the flanges and s is along the Y global axis for the web. According to the third assumption of the Gjelsvik theory (Kirchhoff plate theory) the additional axial displacement of point B offset from the middle surface by a distance t is

$$w = -t\frac{\partial v}{\partial z} \tag{1.25}$$

Therefore, the total longitudinal displacement of the flange can be obtained as

$$w(x,y,z) = w_0(z) - xu_0'(z) - (y+t)v_0'(z) - [\bar{\omega}(x,y) + \bar{\bar{\omega}}(x,t)]\theta_z'(z) \tag{1.26}$$

In which $\bar{\bar{\omega}}(x,t) = xt$ is the additional thickness warping function of the flange. Thus, the total warping function is composed of two components of global warping function $\bar{\omega}(x,y)$ and local warping function $\bar{\bar{\omega}}(x,t)$, i.e.,

$$\omega = \bar{\omega} + \bar{\bar{\omega}} \tag{1.27}$$

The existence of the local warping in addition to the global warping can cause to increase the warping constant of the related cross-section.

1.6. Lateral Torsional Buckling

Thin-walled open cross-sections such as I-shaped wide flanges steel beams and beam-columns inherently suffering from low torsional stiffness. Therefore, they are generally prone to various instability phenomena involving torsion depending on the slenderness of the beam and components of the section (e.g., flanges, web). One of the prevalent buckling modes of failure in beams is Lateral Torsional Buckling (LTB) by which an unconstrained (laterally unsupported) steel beam subjected to transverse loads tends to move laterally and twist about shear center besides its bending about the beam's major axis, and the beam is no longer considered able resist any extra load because of the failure mode sustained. Lateral Torsional Buckling (LTB) has been assessed by modern steel design standards (i.e., Canadian Code CSA-S16, American Code ANSI/AISC 360-16, Euro Code EN-1993-1-1). The current Canadian code for bridge design does not provide clear guidance for evaluating the capacity of steel-bridge girders under the combined action of bending moment and torsion, and this combination give rises to considerable reduction in the strength of the steel girder beams. In other words, it can be assumed that the Lateral Torsional Buckling (LTB) is a dominant mode of failure in steel-bridge girders.

1.6.1. Kinematics in Lateral Torsional Buckling

Deformations in lateral torsional buckling for a laterally unsupported beam with doubly symmetric cross-section include four states which are shown in Figure 1.10, and these states are:

1. Undeformed State
2. Equilibrium State
3. Onset of Buckling State
4. Buckling State

For a prismatic thin-walled beam as depicted in Figure 1.10, beam is initially in the undeformed stage where no load is applied. Under transvers load Q_y, the beam undergoes vertical displacement $v(Z)$ and moves from initial configuration 1 to equilibrium configuration 2. The applied reference load is assumed to increase gradually by a scalar λ and the associated vertical displacement $v(\lambda, z)$ is increasing linearly, and the beam reaches to neutral equilibrium state at configuration 3.

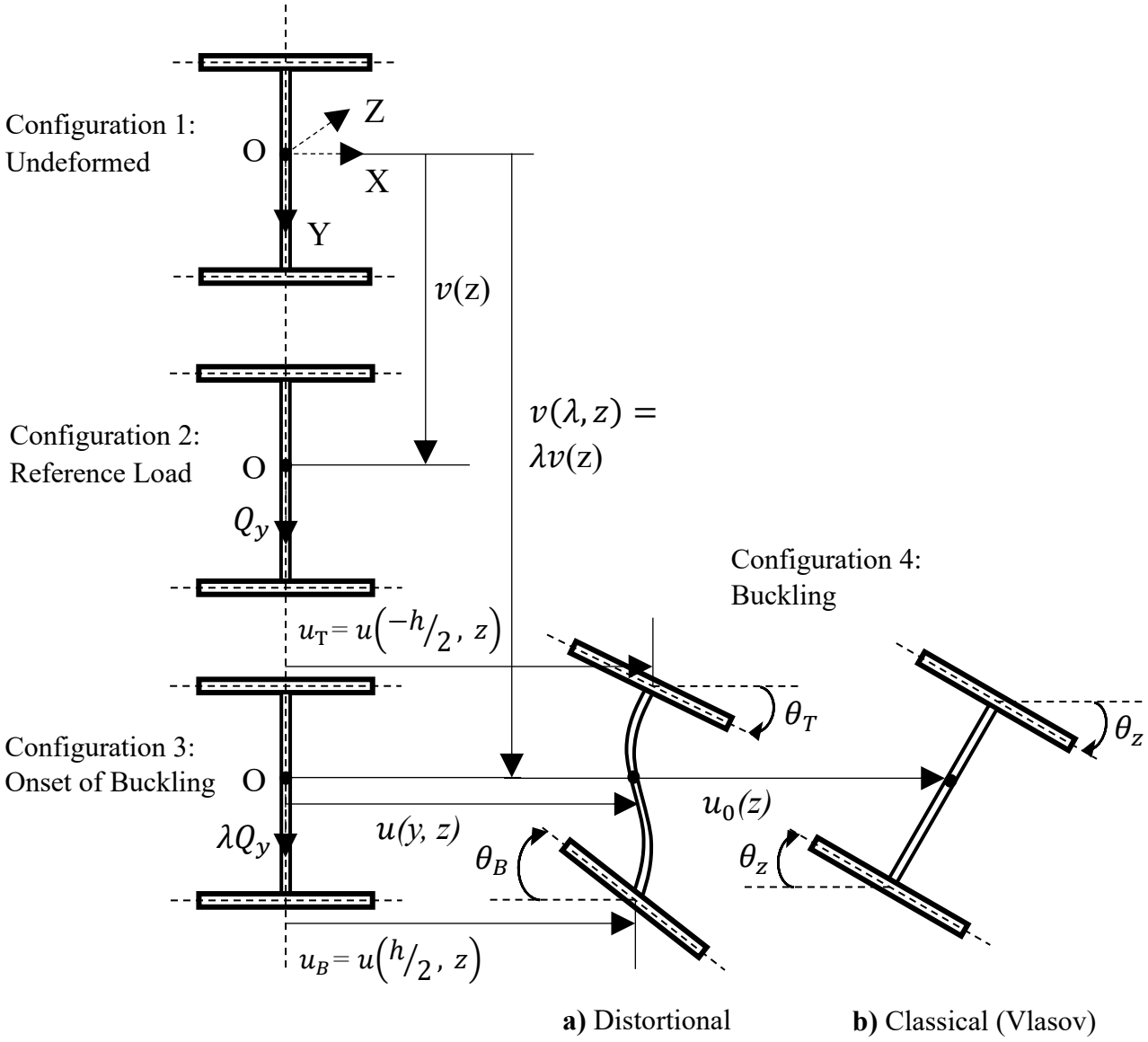

Figure 1.10 Stages of buckling deformation

At the onset of buckling, without increasing the applied load λQ_y the member buckles and suddenly undergoes lateral displacement and twist at the same time (i.e., goes from configuration 3 to configuration 4).

The classical solution for the analysis of LTB is formed on the kinematics of the well-known Vlasov thin-walled beam theory (Vlasov [2]) which is based on two fundamental assumptions (e.g., Section 1.4.6). As illustrate in Figure 1.10, classical approaches such as Vlasov neglect the distortional effects of the cross-section throughout the deformation while in reality for thin-walled

beams particularly for those with slender web and stocky flanges, distortional buckling mode can be observed where the web bending take place. Ignoring the effect of web distortion can lead to overestimating the critical buckling capacity of the beam. Several research have been conducted to consider the web distortional effects. This includes the work of Bradford [13], Hancock et al [14] and Z. Vrcelj and M.A. Bradford [15] who demonstrated that neglecting the web distortion can be detrimental particularly in short spans beams.

1.7. References:

1. Timoshenko, S. P. (1921). LXVI. On the correction for shear of the differential equation for transverse vibrations of prismatic bars. *The London, Edinburgh, and Dublin Philosophical Magazine and Journal of Science*, *41*(245), 744-746.
2. Vlasov, V. Z., (1961). *Thin-walled elastic beams*, Israel Program for Scientific Translations. *Jerusalem, Israel*.
3. Mindlin, R. D., & Deresiewicz, H. (1953). *Timoshenko's shear coefficient for flexural vibrations of beams*. COLUMBIA UNIV NEW YORK.
4. Cowper, G. R. (1966). The shear coefficient in Timoshenko's beam theory.
5. Reddy, J. (1997). On locking-free shear deformable beam finite elements. *Computer methods in applied mechanics and engineering*, *149*(1-4), 113-132.
6. Levinson, M. A. R. K. (1981). A new rectangular beam theory. *Journal of Sound and vibration*, *74*(1), 81-87.
7. Pilkey, W. D. (1994). Formulas for stress, strain, and structural matrices Wiley New York.
8. Bickford, W. B. "Consistent higher order beam theory." Proc., *Developments in Theoretical and Applied Mechanics*, 137-150.
9. Heyliger, P. R., and Reddy, J. N. (1988). "A higher order beam finite element for bending and vibration problems." *Journal of Sound and Vibration*, 126(2), 309-326.
10. Batoz, J. L., & Dhatt, G. (1990). *Modélisation des structures par éléments finis: Solides élastiques*. Presses Université Laval.
11. Saade, K. (2005), Finite Element Modeling of Shear in Thin-Walled Beams with a Single Warping Function, Ph.D Thesis, University of Bruxelles.
12. Gjelsvik, Atle, and D. H. Hodges. "The theory of thin-walled bars." *Journal of Applied Mechanics 49*, no. 2 (1982): 468.
13. Bradford, M. A. (1992). "Lateral-Distortional buckling of steel I—Section members." *Journal of Constructional Steel Research*, 23(1–3), 97-116.
14. Hancock, G. J., Bradford, M. A., and Trahair, N. S. (1980). "Web distortion and flexural-torsional buckling." *Journal of the Structural Division, ASCE*, 106(7), 1557-1571.
15. Vrcelj, Z., and Bradford, M. A. (2006a). "Elastic distortional buckling of continuously restrained I-section beam–columns." *Journal of Constructional Steel Research*, 62(3), 223-230.

1.8. Literature review

One of the prevalent buckling modes of failure in thin-walled beams is lateral-torsional buckling by which an unconstrained steel beam subjected to vertical transverse loads tends to move laterally and twists. Since the early theoretical works of Timoshenko [1] and Bleich [2] there has been a vast amount of work on the lateral-torsional buckling analysis of thin-walled beams. Early numerical studies for the lateral-torsional buckling analysis of thin-walled beams include Krajcinovic [3], Barsoum and Gallagher [4], and Bazant and Nimeri [5] who developed displacement based finite element formulations. The effect of pre-buckling deformations on lateral-torsional buckling of thin-walled beams was investigated by Roberts and Azizian [6], Attard [7], and Pi and Trahair [8]. Effect of shear deformation on buckling behaviour of thin-walled members were investigated in displacement-based formulations by Saade et al. [9], Kim et al [10], Wu and Mohareb [11] and Erkmen and Attard [12]. Erkmen et al. [13] developed a complementary energy-based finite element formulation for torsional buckling analysis of thin-walled columns and Erkmen and Mohareb [14,15] included the shear deformation effects in lateral-torsional buckling by using a complementary energy-based finite element formulation. Based on the Hellinger-Reissner principle, Erkmen [16] and Erkmen et al [17] developed hybrid finite element formulations that can capture shear deformation effects in the buckling analysis of steel and FRP pultruded thin-walled beams. The effect of shear deformation can gain significance especially in the buckling behaviour of beams with built-up or composite sections [18,19] or alternatively when materials with low shear modulus is used such as FRP [20] whose usage in engineering structures is increasing.

To capture the cross-sectional deformations such as web distortions in thin-walled beam behaviour shell element models have been frequently used e.g., [22-26]. Hancock [27] and Adani and Schafer [28] developed finite strip methods to capture the distortional behaviour of the web in the buckling analysis of thin-walled beams. Beam-type Finite Element (FE) formulations that can capture web distortion were developed by Roberts and Jhita [29], Wang et al [30], Ronagh and Bradford [31], and Pezeshky and Mohareb [32]. For the modelling of thin-walled beams, beam-type FE formulations with nodes only at the ends of their longitudinal axis are computationally the most efficient choice as model sizes and accordingly computational time, as well as modelling effort can be kept relatively small compared to shell and finite strip-type modelling approaches. Furthermore, beam behaviour is easier to interpret as the dominant modes of behaviour can be

more easily identified in reduced size models. In fact, beam formulations can be sufficiently equipped to capture any predetermined modes of deformations including web distortions as in the generalized beam theory [33]. For the buckling analysis of thin-walled beams FE formulations based on the generalized beam theory were developed by Camotim et al [34]. However, in generalized beam theory there is significant computational effort required in determining the active modes of deformation and only then the beam element DOFs can be decided for an accurate analysis [35]. A technique for the buckling analysis of thin-walled beams that introduces the modes of deformations in a hierarchical sequence have been presented in [36], which however requires mode orthogonalization adding extra cost to the numerical formulation. The additional modes that are sought in the generalized beam theory are generally the modes that include distortion and local deformations of the cross-section, and kinematically speaking, many thin-walled beam formulations including those with web-distortion can be categorized as special instances of the generalized beam theory where the deformations modes are pre-determined by ignoring the local deformations. As such, the proposed distortional beam formulation falls into a category, where local buckling is not an expected mode of deformation.

One important aspect that is often overlooked in buckling analysis is that the material description for nonlinear strains depends on the choice of strain definition even when the material is elastic. An accurate hyperelastic material description leads to complicated expressions because the material parameters depend on finite deformations. To avoid complications in material description direct adaptation of the generalized Hooke's material, where deformation independent moduli is used, is often justified by assuming that deflections are large, but strains are small. However, literature has shown that when shear deformations are involved contradictory buckling predictions can be produced by adopting the Hooke's material directly as in the case of Engesser versus Haringx column buckling formulas. The difference between two methods has been attributed to different assumptions for the internal normal force orientations at the deformed state of the column [37]. Engesser assumes that the normal force is parallel to the beam axis in the loading state whereas in Haringx theory, the normal force is assumed to be perpendicular to the cross section of the beam. This difference in the assumption of force directions can indeed be traced down to differences in the definitions of adopted strains within the Doyle-Ericksen family of strains and conjugate stresses [38-39]. Although several shear deformable finite element formulations have been proposed for the buckling analysis of thin-walled beams the differences that alternative stress-

strain definitions might cause were not identified in the finite element context. This paper develops a novel beam-type nonlinear Finite Element formulation that is applicable for the analysis of doubly symmetric I-sections that are prone to lateral-torsional buckling, distortion and shear deformation. A linearized buckling formulation has also been derived as a special case of the nonlinear beam formulation under the assumption of no pre-buckling deformations. The formulation is developed in terms of a generic member of the Doyle-Ericksen family of strains, while elastic Hooke's material is adopted for the constitutive relations. As such the developed formulation is an extension of both Engesser and Haringx buckling formulas to thin-walled beams with deformable webs. It is shown that alternative stress-strain definitions lead to changes in the geometric stiffness matrices of thin-walled beam finite element formulations. The effect of changes in the geometric stiffness matrix on the lateral-torsional-distortional buckling load predictions of thin-walled beams is illustrated in numerical tests.

The current thesis is organized as follows; Kinematic relations of the thin-walled beams including web distortion and shear deformations, and adaptation of Doyle-Ericksen family of strains according to the beam kinematics are presented in chapter 2. The weak forms of equilibrium equations and the variational formulation for nonlinear and buckling analyses are generated in chapter 3. The interpolation scheme and the associated finite element formulation, and also a special case of the beam formulation where web distortions are suppressed are given in chapter 4. Case studies for linear static analysis are introduced and verified in chapter 5, where effects of web distortion, and shear deformations are depicted. Buckling case studies are presented in chapter 6, where effects of web distortion are illustrated. Alternative strain tensor of the Doyle-Ericksen family are illustrated for thin-walled composite materials are developed and written in paper format in chapter 7. Conclusions are drawn in chapter 8.

2. Chapter 2: Distortional Thin-walled Beam Kinematics

2.1. Coordinate System

For a prismatic thin-walled beam with an open cross-section the Lagrangian approach is adopted based on which a material coordinate system (*x, y, z)* that changes with the deformation is used, and the corresponding lateral, transversal and longitudinal displacement fields are (*u, v, w*) where according to the dependence of the displacement fields on all three dimensions it leads to discretization in three coordinates, i.e., *w=w(x, y, z),* etc. The benefit of applying material (or Lagrangian) coordinates is that, not only it is simple to keep track of a point as its material coordinate never changes after initial identification, but also boundary conditions and interface conditions are easily applied due to the fact that boundary nodes remain on the boundary. Moreover, a set of right-handed local curvilinear coordinate system (s, r) is defined to each segment which moves along the mid-surfaces of the undeformed plate segments that is tangent to the contour along the middle surface of the section and through thickness direction which is normal to the tangent to the contour respectively referred as coordinates *s* and *r*. An arbitrary local coordinate pole (a_{Lx}, a_{Ly}) located at (x, y) called R is chosen for each segment. Adaptation of *s-r* coordinate system allows us to impose the kinematic assumptions on the thin-walled segments more directly and characterizes the coordinates of a point offset from the mid-surface by a distance r and s is a coordinate tangential to the mid-surface. Accordingly, following coordinates transformation rules can be determined for relating the coordinates of (x, y) to (s, r):

2.1

$$\frac{\mathrm{d}x}{\mathrm{d}s}=\cos\alpha\,,\qquad \frac{\mathrm{d}y}{\mathrm{d}s}=\sin\alpha\,,\qquad \frac{\mathrm{d}x}{\mathrm{d}r}=-\sin\alpha\,,\qquad \frac{\mathrm{d}y}{\mathrm{d}r}=\cos\alpha$$

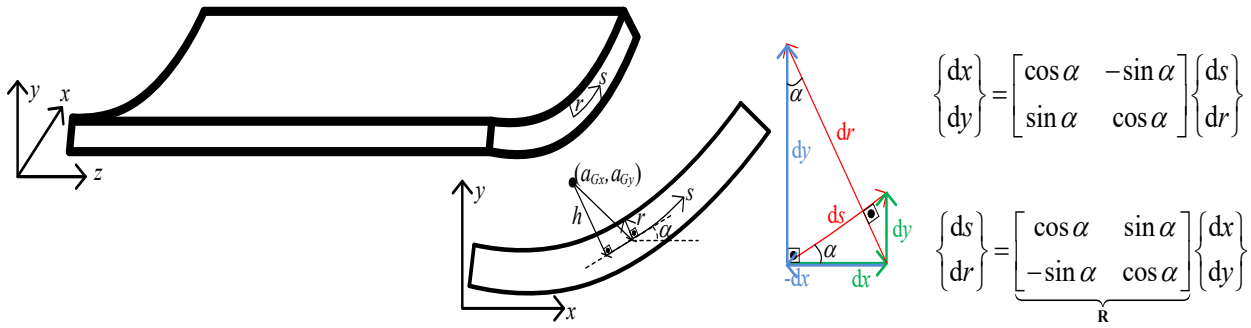

Figure 2.1 A general thin-walled beam segment and the coordinate systems – see ref [37]

2.2. Assumptions and kinematics

The material is assumed to be linearly elastic, homogeneous, and isotropic and therefore it obeys Hooke's law. Also, the formulation is restricted to prismatic members and cross-sections are open and doubly symmetric. Strains are assumed small, but rotations are assumed second-order, thus nonlinear strain components due to the rotation effects are maintained in the formulation.

2.3. Displacements in the plane of the cross-sections

For the introduced global right-handed coordinate system, the origin is located at the mid-height of the web. Considering a generic point that offset from the middle surface of the related segment (e.g., flanges, web), the lateral and transverse displacements, each divided into two components: a) the horizontal or vertical displacement component at the origin lying on the middle surface pertaining to rigid body movement which is denoted by single bars, $\bar{u}(z)$ and $\bar{v}(z)$ respectively, and b) a component because of the rotation of the offset distance from the mid-surface of the segment.

At a given cross-section, based on the right hand rule the rotation of the cross-section around the longitudinal axis (z) can cause a generic point in the plane of x-y to move to the left side. Therefore, the horizontal component of the displacement vector is a function of y and z only, i.e.

$$u(y,z) = \bar{u} + \int_{a_{Gy}}^{y} \dot{u}\mathrm{d}y \tag{2.2}$$

where $\bar{u}(z)=u(a_{Gy},z)$ is generally defined at a selected reference point a_G, which is called herein as the global pole and are conveniently selected at the shear center on the web. In 2.2, $\dot{(\,)}$ indicates derivative along the web direction, i.e., with respect to y. The angle of twist around the z-axis $\phi_z(y,z)$ is also a function of both y and z, and it is related to the horizontal displacement as $\phi_z(y,z)=-\dot{u}(y,z)$. The web is allowed to bend about the longitudinal axis z due to change in the twist angle along the web; however, the flanges stay rigid within the plane of the cross-section, therefore the twist angle is constant on the flanges. In a similar manner, the $\phi_z(y,z)$ gives rises to an arbitrary point in the plane of the cross-section to move upward. As a result, the vertical component of the displacement vector can be written as

$$v(x,y,z) = \bar{v}(z) + \int_{a_{Lx}}^{x} \phi_z \, dx \qquad 2.3$$

in which $\bar{v}(z) = v(a_{Gx}, a_{Gy}, z)$. In equations 2.2 and 2.3 a_{Lx} and a_{Ly} are respectively the x and y coordinates at the middle of each segment.

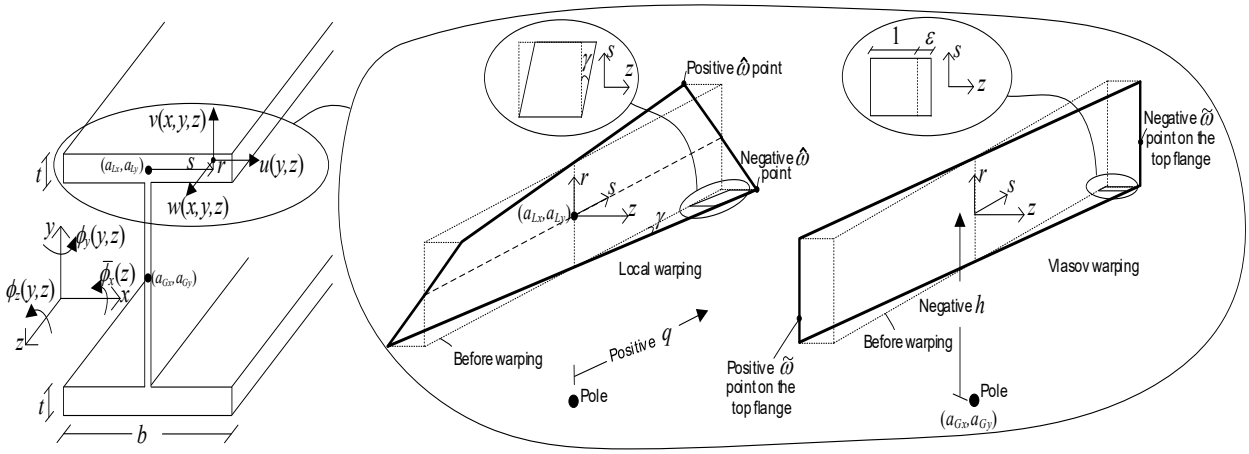

Figure 2.2 Displacement field of a doubly symmetric I-section, a) Displacement functions b) Warping of the cross-section - See ref [37]

2.4. Longitudinal displacement

The axial displacement field *w* of a point *x, y, z* on the cross-section can be expressed as

$$w(x,y,z) = \bar{w} - x\varphi_y + y\varphi_x - \hat{\omega}\phi_z' \qquad 2.4$$

In which $\bar{w}(z) = w(a_{Gx}, a_{Gy}, z)$ characterizes the longitudinal displacement because of elongation of the centroidal axis of the beam, also second and third terms are due to the bending about weak axis and strong axis respectively while the last item which is $\hat{\omega}$ specifies local warping function due to Saint Venant's uniform torsion. From the Saint Venant's elasticity solution under uniform torsion assumption, in the limit case of thin segments, i.e., $t/b \to 0$, the local warping function simplifies to (Oden [24])

$$\underset{t/b\to 0}{\hat{\omega}} = q_L r \qquad 2.5$$

in which $r=-(x-a_{Lx})\sin\alpha+(y-a_{Ly})\cos\alpha$ and $q_L=(x-a_{Lx})\cos\alpha+(y-a_{Ly})\sin\alpha$. For a segment where coordinates (a_{Lx},a_{Ly}) and (a_{Gx},a_{Gy}) are identical, q and h can be shown as in Figure 2.3 and r is again the coordinate through thickness direction as previously shown in Figure 2.1 and Figure 2.2.

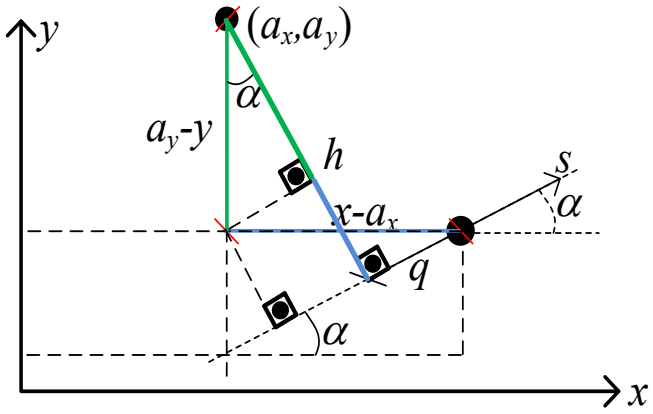

Figure 2.3 Thin-walled beam segment and the coordinate system – see ref [37]

For the rotation angles φ_x and φ_y, by including the second order terms of the Euler-Rodriguez rotation tensor [25], from equation 2.4, one obtains:

$$w(x,y,z)=\bar{w}-x\phi_y+y\bar{\phi}_x-\hat{\omega}\phi_z'-\frac{1}{2}x\bar{v}'\phi_z+\frac{1}{2}yu'\phi_z \tag{2.6}$$

in which $\varphi_x=\phi_x+0.5u'\phi_z$ and $\varphi_y=\phi_y+0.5\bar{v}'\phi_z$ are due to Euler-Rodriguez rotation tensor. In equation 2.6, the last two terms include the second order twist effect on the bending related rotations around both x and y axes, which might have significant influence on lateral-torsional buckling predictions [26]. The bending related rotation function around x axis, stays constant at any point on the cross-section and therefore it is only a function of the z coordinate, i.e., $\phi_x(z)=\bar{\phi}_x(z)$. Our aim is to develop a distortional thin-walled beam formulation in a hierarchical manner so that classical rigid-cross-section thin-walled beam formulation can be easily identified as a special case. For that purpose, we introduce the global warping function of Vlasov [28], i.e. $\tilde{\omega}=\int h\mathrm{d}s=\int h\cos\alpha\mathrm{d}x+\int h\sin\alpha\mathrm{d}y$ (see Figure 2.2). The coordinate h for a general cross-section can be calculated as $h=(x-a_{Gx})\sin\alpha-(y-a_{Gy})\cos\alpha$ in which (a_{Gx},a_{Gy}) are the coordinates of the global pole (see Figure 2.1). We define a global warping related general displacement as

$\psi(y,z)=-\dot{\phi}_y(y,z)$, which takes the value $\bar{\psi}(z)=\psi(a_{Gy},z)$ at the global pole, i.e. $\psi(y,z)=\bar{\psi}(z)+\int_{a_{Gy}}^{y}\dot{\psi}\,\mathrm{d}y$ and $\phi_y(y,z)=\bar{\phi}_y-\int_{a_{Gy}}^{y}\psi\,\mathrm{d}y$ in which $\bar{\phi}_y(z)=\phi_y(a_{Gy},z)$. Similarly, the rotation field around z axis can be written as $\phi_z(y,z)=\bar{\phi}_z(z)+\int_{a_{Gy}}^{y}\dot{\phi}_z\mathrm{d}y$ where $\bar{\phi}_z(z)=\phi_z(a_{Gy},z)$ is the angle of twist around the z-axis at the global pole a_G. Accordingly, equation 2.6 can be re-written as

$$w(x,y,z)=\bar{w}-x\bar{\phi}_y+y\bar{\phi}_x-\tilde{\omega}\bar{\psi}+x\int_{a_{Gy}}^{y}\left(\int_{a_{Gs}}^{s}\dot{\psi}\mathrm{d}s\right)\mathrm{d}y-\hat{\omega}\phi_z'-\frac{1}{2}x\bar{v}'\phi_z+\frac{1}{2}yu'\phi_z \tag{2.7}$$

in which $\tilde{\omega}=-x\left(y-a_{Gy}\right)$ was used.

2.5. Expressions for Strains

For the Doyle-Ericksen finite strain tensor definition in continuum, we refer to Bazant and Cedolin [28], i.e. $\boldsymbol{\varepsilon}_m=\left(\mathbf{U}^2-\mathbf{I}\right)/2$, where $\mathbf{I}$ is the unit tensor, and $\mathbf{U}$ is the right-stretch tensor of polar decomposition of the deformation gradient. Majority of the strain tensors used in stability theories are produced in terms of the Green-Lagrange strain tensor. For calculating the critical loads in buckling, only the second-order approximations to the strain tensor matters. Therefore, we limit ourselves to second order accuracy and the pre-buckling deformation effects are not considered. They can be considered in a nonlinear analysis. We can express the second order approximation to the Green-Lagrange strain tensors as

$$\boldsymbol{\varepsilon}_m=\boldsymbol{\varepsilon}+\mathbf{e}=\begin{bmatrix}\varepsilon_{mxx} & \varepsilon_{mxy} & \varepsilon_{mxz}\\ \varepsilon_{myx} & \varepsilon_{myy} & \varepsilon_{myz}\\ \varepsilon_{mzx} & \varepsilon_{mzy} & \varepsilon_{mzz}\end{bmatrix} \tag{2.8}$$

which consists of a first order strain tensor $\boldsymbol{\varepsilon}$, and a second order strain tensor $\mathbf{e}$. The first and second order components of the strain tensor can be written respectively as

$$\boldsymbol{\varepsilon} = \begin{bmatrix} \varepsilon_{xx} & \varepsilon_{xy} & \varepsilon_{xz} \\ \varepsilon_{yx} & \varepsilon_{yy} & \varepsilon_{yz} \\ \varepsilon_{zx} & \varepsilon_{zy} & \varepsilon_{zz} \end{bmatrix} = \frac{1}{2}\begin{bmatrix} 2\dfrac{\partial u}{\partial x} & \dfrac{\partial u}{\partial y}+\dfrac{\partial v}{\partial x} & \dfrac{\partial u}{\partial z}+\dfrac{\partial w}{\partial x} \\ \dfrac{\partial v}{\partial x}+\dfrac{\partial u}{\partial y} & 2\dfrac{\partial v}{\partial y} & \dfrac{\partial v}{\partial z}+\dfrac{\partial w}{\partial y} \\ \dfrac{\partial w}{\partial x}+\dfrac{\partial u}{\partial z} & \dfrac{\partial w}{\partial y}+\dfrac{\partial v}{\partial z} & 2\dfrac{\partial w}{\partial z} \end{bmatrix} \tag{2.9}$$

$$\mathbf{e} = \begin{bmatrix} e_{xx} & e_{xy} & e_{xz} \\ e_{yx} & e_{yy} & e_{yz} \\ e_{zx} & e_{zy} & e_{zz} \end{bmatrix} = \frac{1}{2}\begin{bmatrix} \left(\dfrac{\partial u}{\partial x}\right)^2+\left(\dfrac{\partial v}{\partial x}\right)^2+\left(\dfrac{\partial w}{\partial x}\right)^2 & \dfrac{\partial u}{\partial x}\dfrac{\partial u}{\partial y}+\dfrac{\partial v}{\partial x}\dfrac{\partial v}{\partial y}+\dfrac{\partial w}{\partial x}\dfrac{\partial w}{\partial y} & \dfrac{\partial u}{\partial x}\dfrac{\partial u}{\partial z}+\dfrac{\partial v}{\partial x}\dfrac{\partial v}{\partial z}+\dfrac{\partial w}{\partial x}\dfrac{\partial w}{\partial z} \\ \dfrac{\partial u}{\partial y}\dfrac{\partial u}{\partial x}+\dfrac{\partial v}{\partial y}\dfrac{\partial v}{\partial x}+\dfrac{\partial w}{\partial y}\dfrac{\partial w}{\partial x} & \left(\dfrac{\partial u}{\partial y}\right)^2+\left(\dfrac{\partial v}{\partial y}\right)^2+\left(\dfrac{\partial w}{\partial y}\right)^2 & \dfrac{\partial u}{\partial y}\dfrac{\partial u}{\partial z}+\dfrac{\partial v}{\partial y}\dfrac{\partial v}{\partial z}+\dfrac{\partial w}{\partial y}\dfrac{\partial w}{\partial z} \\ \dfrac{\partial u}{\partial z}\dfrac{\partial u}{\partial x}+\dfrac{\partial v}{\partial z}\dfrac{\partial v}{\partial x}+\dfrac{\partial w}{\partial z}\dfrac{\partial w}{\partial x} & \dfrac{\partial u}{\partial z}\dfrac{\partial u}{\partial y}+\dfrac{\partial v}{\partial z}\dfrac{\partial v}{\partial y}+\dfrac{\partial w}{\partial z}\dfrac{\partial w}{\partial y} & \left(\dfrac{\partial u}{\partial z}\right)^2+\left(\dfrac{\partial v}{\partial z}\right)^2+\left(\dfrac{\partial w}{\partial z}\right)^2 \end{bmatrix} \tag{2.10}$$

Although some accuracy is compromised due to omission of third and higher order terms in the strain tensor, this is a convenient form as the strain components are in terms of derivatives of displacements with respect to fixed directions. It should be noted that one of the simplifying assumptions of beam kinematics is adopted, that is the shear deformations within the cross-sectional plane are omitted i.e., $\varepsilon_{xy} = e_{xy} = 0$. As the flange mid-surfaces are placed within the z-x plane and that the flanges are assumed rigid in their own plane, we also impose that $\varepsilon_{xx} = e_{xx} = 0$. As a result, out of six linear strain components in equation 2.9 only four components are non-zero, which can be written in terms of displacement derivatives as

$$\varepsilon_{zz} = \bar{w}' - x\bar{\phi}_y' + y\bar{\phi}_x' - \tilde{\omega}\bar{\psi}' + x\int_{a_{Gy}}^{y}\left(\int_{a_{Gs}}^{s}\dot{\psi}'\mathrm{d}s\right)\mathrm{d}y \tag{2.11}$$

$$\varepsilon_{yy} = -r\dot{\phi}_z \tag{2.12}$$

2.13

$$\varepsilon_{xz}=\frac{1}{2}\left(\overline{u}'-\int_{a_{Gy}}^{y}\phi_z'\mathrm{d}y-\overline{\phi}_y-\grave{\tilde{\omega}}\overline{\psi}+\int_{a_{Gy}}^{y}\left(\int_{a_{Gs}}^{y}\dot{\psi}\mathrm{d}y\right)\mathrm{d}y-\grave{\hat{\omega}}\phi_z'\right)$$

$$\varepsilon_{yz}=\frac{1}{2}\left(\overline{v}'+\int_{a_{Gx}}^{x}\phi_z'\mathrm{d}x+\overline{\phi}_x-\dot{\tilde{\omega}}\overline{\psi}+x\int_{a_{Gy}}^{y}\dot{\psi}\mathrm{d}y-\dot{\hat{\omega}}\phi_z'-\hat{\omega}\dot{\phi}_z'\right) \qquad 2.14$$

in which $\grave{}(),\dot{}(),()'$ indicate derivatives with respect to *x*, *y*, *z* respectively, and $\tilde{\omega}=-x\left(y-a_{Gy}\right)$ was used. We assume that $\ddot{\psi}(y,z)=-\chi(z)$ is constant in the *y* direction, i.e., $\dot{\psi}=\int\ddot{\psi}\mathrm{d}y+c=-\chi(z)y+c(z)$ in which $c(z)$ is the integration constant. We will employ an interpolation scheme in Section 4 consistent with this assumption. Accordingly, from the relations $\int_{a_{Gy}}^{y}\dot{\psi}\mathrm{d}y=-0.5\chi\left(y^2-a_{Gy}{}^2\right)+c\left(y-a_{Gy}\right)$ and $\int_{y_B}^{y_T}\dot{\psi}\mathrm{d}y=\psi_T-\psi_B$, the integration constant can be identified as $c=\frac{(\psi_T-\psi_B)}{(y_T-y_B)}+\frac{\chi}{2}(y_T+y_B)$, where ψ_T and ψ_B are the values of the function $\psi(y,z)$ at the top and bottom flanges, respectively. By using $\int_{a_{Gy}}^{y}\left(\int_{a_{Gs}}^{y}\dot{\psi}\mathrm{d}y\right)\mathrm{d}y=-\frac{\chi}{6}\left(y^3-a_{Gy}{}^3\right)+\frac{\chi a_{Gy}{}^2}{2}\left(y-a_{Gy}\right)+\frac{c}{2}\left(y-a_{Gy}\right)^2$ in equation 2.13, one obtains: *2.13*

2.15

$$\varepsilon_{zz}=\overline{w}'-x\overline{\phi}_y'+y\overline{\phi}_x'-\tilde{\omega}\overline{\psi}'+\tilde{\omega}\frac{\chi'}{6}\left(y^2+a_{Gy}y-2a_{Gy}{}^2\right)-\tilde{\omega}\frac{c'}{2}\left(y-a_{Gy}\right)$$

in which the last two terms are due to the effect of web bending. It is also important to note that in obtaining equation 2.10 and consequently equation 2.15, the derivative of the sixth term in equation 2.7with respect to z was assumed zero, i.e., $\partial\left(\hat{\omega}\phi_z'\right)/\partial z=0$ under the assumption of uniform torsion. This is because contribution of local warping to the axial displacement field is based on the Saint Venant elasticity solution under uniform torsion assumption, in which case ϕ_z'=constant as discussed in section 2.3. Thus, local warping should not cause normal strains along the z or y directions. Therefore, an ad-hoc adjustment is needed within the thin-walled beam theory so that the thin-walled beam behaviour can be captured as a special case of unification of plate segments. To contrast the beam and plate kinematics; in plate kinematics twist action results with

angle change in both z and q directions shown in Figure 2.4. In (Kirchhoff or Mindlin-Reissner) plate kinematics, it is assumed that under twist action in the limit case of an infinitesimal element, i.e., $\Delta z \to dz$, twist curvature is $\rho = 4\phi_z'$, mid-surface is rigid and surfaces above or below deform due to shear within their own plane without bending (see Figure 2.4). This kinematics is imposed as a result of the selected displacement field, i.e., $u = r\phi$, $v \equiv v(z,q,0)$ and $w = -r\beta$. As a result, under pure twist plate theory avoids any contribution to axial strains, i.e. $\varepsilon_z = \partial w/\partial z = 0$ and $\varepsilon_q = \partial u/\partial q = 0$ since the mid-surface is rigid, i.e. $\partial\phi/\partial q = \partial\beta/\partial z = 0$ and the fiber lengths stay the same before and after deformation. It should be noted that both (Kirchhoff or Mindlin-Reissner) linear plate theories and Saint Venant thin-walled plate solution predict the shear strains, i.e., $\gamma = \partial u/\partial z + \partial w/\partial q = 0.5r\rho$ and as a result the twisting moment-angle of twist relations i.e., $M_t = GJ\phi_z'$ identically, where M_t is the twisting moment acting around the z axis, G is the shear modulus and $J = bt^3/3$ is the torsional constant of the section perpendicular to z axis in which b is the width and t is the thickness of the plate (see Figure 2.2 for b and t of the flanges).

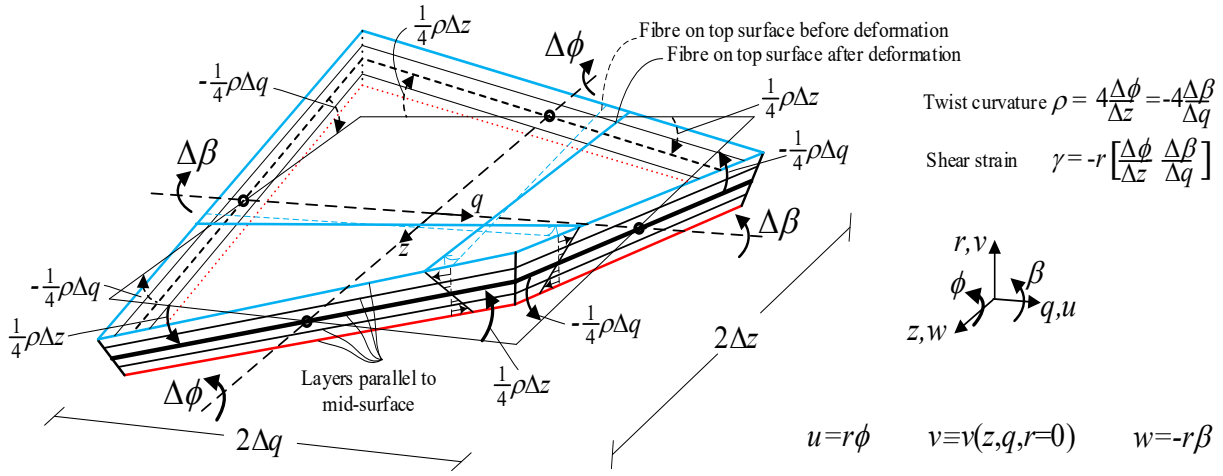

Figure 2.4 Uniform twist action of a plate segment – see ref [37]

On the other hand, in beam kinematics there is no assumption imposed along the axial direction of the beam. However, it is not meaningful to generate normal strains under uniform torsion that cannot be obtained either from the plate theories or Saint Venant elasticity solution. Accordingly, the first order shear strain, i.e., $\gamma = 2\varepsilon_{xz}\cos\alpha + 2\varepsilon_{yz}\sin\alpha$ can be obtained from equations 2.13 and 2.14 considering the orientation of the thin-walled segment, i.e.,

$$\gamma=\left(\bar{u}'-\bar{\phi}_y\right)\cos\alpha+\left(\bar{v}'+\bar{\phi}_x\right)\sin\alpha-h\left(\bar{\psi}-\bar{\phi}_z'\right)-2r\phi_z' \qquad 2.16$$

In obtaining equation 2.16, the coordinate transformation rules, i.e., $r=\tilde{\omega}\sin\alpha+\dot{\tilde{\omega}}\cos\alpha$ and $h=\tilde{\omega}\cos\alpha+\dot{\tilde{\omega}}\sin\alpha$ were used. Note that the term $\tilde{\omega}\psi\sin\alpha$ vanishes since $\tilde{\omega}=0$ on the web and $\sin\alpha=0$ on the flange. We have also used $\phi_z'(y,z)=\bar{\phi}_z'(z)+\int_{a_{Gy}}^{y}\dot{\phi}_z'\mathrm{d}y$. To eliminate the shear strains along the contour directions, we assume that $\bar{u}'=\bar{\phi}_y$, $\bar{v}'=-\bar{\phi}_x$ and $\bar{\psi}=\bar{\phi}_z'$, and we will adopt an interpolation scheme for the numerical solution accordingly. Thus, only the shear strains produced by the St. Venant torsion are considered, i.e., $\gamma=-2r\phi_z'$, which is a widely used approximation in thin-walled beam formulations considering their slenderness, e.g. [18-20].

The non-zero second order strain components can be written in terms of displacement derivatives by substituting the relation $v'=\bar{v}'+\int_{a_{Gx}}^{x}\phi_z'\mathrm{d}x=\bar{v}'+\left(x-a_{Gx}\right)\phi_z'$ into $e_{zz}=\frac{1}{2}\left(u'^2+v'^2\right)$ as

$$e_{zz}=\frac{1}{2}\left(u'^2+\bar{v}'^2\right)-a_{Gx}\bar{v}'\phi_z'-\frac{1}{2}x\left(\bar{v}''\phi_z-\bar{v}'\phi_z'\right)+\frac{1}{2}y\left(u'\phi_z'+u''\phi_z\right)+\frac{1}{2}\left(x-a_{Gx}\right)^2\phi_z'^2 \qquad 2.17$$

and

$$e_{yy}=\left(\frac{1}{2}\phi_z^{\,2}+\frac{1}{2}\bar{\phi}_x^{\,2}\right)\mu \qquad 2.18$$

Note that in obtaining equation 2.17, the relation $(y-a_{Gy})\phi_z=(y-a_{Ly})\phi_z-h\bar{\phi}_z$ and the fact that a_{Lx} coincides with a_{Gx} were used. The strains due to second order effects of the extensions of the beam axis and the web, i.e., $\bar{w}'\bar{w}'=\dot{v}\dot{v}=\dot{v}v'=0$ and the second order shear strains are omitted. One would come across equation 2.17 in thin-walled buckling formulations with rigid web e.g. [29]. On the other hand, equation 2.18 contributes to web buckling, which however should be used with caution considering the pressures applied in the web direction. There will be more discussions within the numerical studies in chapter 6 regarding the necessity or possible consequences of equation 2.18. Therefore, we put an on/off switch to equation 2.18 by introducing the parameter μ which is either zero or one. Unless stated otherwise μ is taken as 0.

2.6. Variations of Strains

From the linear strain components in equations 2.15, 2.12 and 2.16, the first variations of the non-zero linear strain tensor components can be written as

$$\delta\varepsilon_{zz} = \delta\bar{w}' - x\delta\bar{\phi}_y' + y\delta\bar{\phi}_x' - \tilde{\omega}\delta\bar{\psi}' - \tilde{\omega}\frac{\delta\chi'}{6}\left(y^2 + a_{Gy}y - 2a_{Gy}^{\,2}\right) - \tilde{\omega}\frac{\delta c'}{2}\left(y - a_{Gy}\right) \tag{2.19}$$

$$\delta\varepsilon_{yy} = -r\delta\dot{\phi}_z \tag{2.20}$$

$$\delta\gamma = -2r\delta\phi_z' \tag{2.21}$$

Similarly, from the second order strain components in equations 2.17 and 2.18, the first variations of the non-zero second order strain tensor components can be written as

$$\begin{aligned}\delta e_{zz} = {} & u'\delta u' + \left(\bar{v}' - a_{Gx}\phi_z'\right)\delta\bar{v}' - a_{Gx}\bar{v}'\delta\phi_z' + \frac{1}{2}y\bar{u}'\delta\phi_z' + \frac{1}{2}y\phi_z'\delta\bar{u}' + \frac{1}{2}y\bar{u}''\delta\phi_z + \frac{1}{2}y\phi_z\delta\bar{u}'' + \left(x - a_{Gx}\right)^2\phi_z'\delta\phi_z' \\ & - \frac{1}{2}x\bar{v}''\delta\phi_z - \frac{1}{2}x\phi_z\delta\bar{v}'' + \frac{1}{2}x\bar{v}'\delta\phi_z' + \frac{1}{2}x\phi_z'\delta\bar{v}'\end{aligned} \tag{2.22}$$

$$\delta e_{yy} = \left(\phi_z\delta\phi_z + \bar{\phi}_x\delta\bar{\phi}_x\right)\mu \tag{2.23}$$

The second variations of the second order strain can be written as

$$\delta^2 e_{zz} = \delta u'^2 + \delta\bar{v}'^2 - 2a_{Gx}\delta\bar{v}'\delta\phi_z' - x\left(\delta\bar{v}''\delta\phi_z - \delta\bar{v}'\delta\phi_z'\right) + y\left(\delta u'\delta\phi_z' + \delta u''\delta\phi_z\right) + \left(x - a_{Gx}\right)^2\delta\phi_z'^2 \tag{2.24}$$

$$\delta^2 e_{yy} = \left(\delta\phi_z^{\,2} + \delta\bar{\phi}_x^{\,2}\right)\mu \tag{2.25}$$

Voigt notation is used as the strain tensor have symmetry properties. Accordingly, the strain tensor can be expressed in vector form as

$$\boldsymbol{\varepsilon}_m \equiv \left[\begin{array}{c:c:c} 0 & 0 & \varepsilon_{mxz} \\ \hdashline 0 & \varepsilon_{myy} & \varepsilon_{myz} \\ \hdashline \varepsilon_{mzx} & \varepsilon_{mzy} & \varepsilon_{mzz} \end{array}\right] \rightarrow \left\{\begin{array}{c} \varepsilon_{mzz} \\ \varepsilon_{myy} \\ 2\varepsilon_{mxz}\cos\alpha + 2\varepsilon_{myz}\sin\alpha \end{array}\right\} = \left\{\begin{array}{c} \varepsilon_{mzz} \\ \varepsilon_{myy} \\ \gamma_m \end{array}\right\} \tag{2.26}$$

Similar to equation 2.8, we decompose the strains as $\boldsymbol{\varepsilon}_m = \boldsymbol{\varepsilon} + \mathbf{e}$ where

$$\boldsymbol{\varepsilon} = \left\langle \varepsilon_{zz} \quad \varepsilon_{yy} \quad \gamma \right\rangle^{\mathrm{T}} \tag{2.27}$$

$$\mathbf{e} = \left\langle e_{zz} \quad e_{yy} \quad 0 \right\rangle^{\mathrm{T}} \tag{2.28}$$

Strain components in equations 2.27 and 2.28 can be identified from equations 2.12, 2.15-18.

2.7. Strain decomposition using matrix-vector multiplications

For numerical implementation purposes, in the following the variations of the strain expressions are organized in the form of matrix-vector multiplications. In Voigt notation one can express the first variation of the linear strain as $\delta\boldsymbol{\varepsilon} = \bar{\mathbf{s}}\delta\boldsymbol{\chi}_L$, in which

$$\bar{\mathbf{s}} = \left[\begin{array}{ccccccc:cc:c} 1 & -x & -y & -\tilde{\omega} & \frac{\tilde{\omega}}{6}\left(y^2 + a_{Gy}y - 2a_{Gy}{}^2\right) & -\frac{\tilde{\omega}}{2}\left(y - a_{Gy}\right) & x^2+y^2 & 0 & 0 & 0 \\ 0 & 0 & 0 & 0 & 0 & 0 & 0 & 1 & -r & 0 \\ 0 & 0 & 0 & 0 & 0 & 0 & 0 & 0 & 0 & -2r \end{array}\right] \tag{2.29}$$

and

$$\boldsymbol{\chi}_L = \left\langle \bar{w}' \quad \bar{\phi}_y' \quad -\bar{\phi}_x' \quad \bar{\psi}' \quad \chi' \quad c' \quad 0 \;\vdots\; 0 \quad \dot{\phi}_z \;\vdots\; \phi_z' \right\rangle^{\mathrm{T}} \tag{2.30}$$

Similarly, in Voigt notation, the first variation of the second order strains can be written as $\delta\mathbf{e} = \bar{\mathbf{s}}\mathbf{A}\delta\boldsymbol{\chi}_A$, in which

$$\boldsymbol{\chi}_A = \left\langle u' \quad \bar{v}' \quad \bar{\phi}_x \quad \phi_z \quad \phi_z' \quad u'' \quad \bar{v}'' \right\rangle^{\mathrm{T}} \tag{2.31}$$

and

$$\mathbf{A}=\left[\begin{array}{ccccccc}
u'+a_{Gy}\phi_z' & \bar{v}'-a_{Gx}\phi_z' & 0 & 0 & a_{Gy}u'-a_{Gx}\bar{v}'+\left(a_{Gx}{}^2+a_{Gy}{}^2\right)\phi_z' & 0 & 0 \\
0 & 0 & 0 & \bar{v}'' & 2a_{Gx}\phi_z' & 0 & \phi_z \\
0 & 0 & 0 & -u'' & 2a_{Gy}\phi_z' & -\phi_z & 0 \\
0 & 0 & 0 & 0 & 0 & 0 & 0 \\
0 & 0 & 0 & 0 & 0 & 0 & 0 \\
0 & 0 & 0 & 0 & 0 & 0 & 0 \\
0 & 0 & 0 & 0 & \phi_z' & 0 & 0 \\
\hline
0 & 0 & \bar{\phi}_x\mu & \phi_z\mu & 0 & 0 & 0 \\
0 & 0 & 0 & 0 & 0 & 0 & 0 \\
\hline
0 & 0 & 0 & 0 & 0 & 0 & 0
\end{array}\right] \qquad 2.32$$

The second variation of equation 2.28 can be re-written as

$$\delta^2\mathbf{e}=\bar{\mathbf{s}}\left(\mathbf{t}_1\delta\boldsymbol{\chi}_A{}^{\mathrm{T}}\mathbf{G}_1+\mathbf{t}_2\delta\boldsymbol{\chi}_A{}^{\mathrm{T}}\mathbf{t}_{G2}{}^{\mathrm{T}}\mathbf{G}_2\mathbf{t}_{G2}\right)\delta\boldsymbol{\chi}_A \qquad 2.33$$

in which $\mathbf{t}_1=\langle 1 \,\vdots\, \mathbf{0}_{1\times 9}\rangle^{\mathrm{T}}$, $\mathbf{t}_2=\langle \mathbf{0}_{1\times 7} \,\vdots\, 1 \,\vdots\, \mathbf{0}_{1\times 2}\rangle^{\mathrm{T}}$,

$$\mathbf{G}_1=\left[\begin{array}{ccccccc}
1 & 0 & 0 & 0 & \frac{y}{2} & 0 & 0 \\
0 & 1 & 0 & 0 & \frac{x}{2}-a_{Gx} & 0 & 0 \\
0 & 0 & 0 & 0 & 0 & 0 & 0 \\
0 & 0 & 0 & 0 & 0 & \frac{y}{2} & -\frac{x}{2} \\
\frac{y}{2} & \frac{x}{2}-a_{Gx} & 0 & 0 & \left(x-a_{Gx}\right)^2 & 0 & 0 \\
0 & 0 & 0 & \frac{y}{2} & 0 & 0 & 0 \\
0 & 0 & 0 & -\frac{x}{2} & 0 & 0 & 0
\end{array}\right] \qquad 2.34$$

$\mathbf{G}_2=\begin{bmatrix}1 & 0\\ 0 & 1\end{bmatrix}$ and $\mathbf{t}_{G2}{}^{\mathrm{T}}=\begin{bmatrix}0 & 0 & 1 & 0 & 0 & 0 & 0\\ 0 & 0 & 0 & 1 & 0 & 0 & 0\end{bmatrix}$.

3. Chapter 3: Weak Form of Equilibrium Equations

3.1. Constitutive relation

We develop the constitutive relations under plane stress assumption as:

$$\boldsymbol{\sigma}_m = \mathbf{E}_a \boldsymbol{\varepsilon}_m = \frac{E}{\left(1-\upsilon^2\right)} \begin{bmatrix} 1 & \upsilon & 0 \\ \upsilon & 1 & 0 \\ 0 & 0 & \dfrac{(1-\upsilon)}{2} \end{bmatrix} \begin{Bmatrix} \varepsilon_{mzz} \\ \varepsilon_{myy} \\ \gamma_m \end{Bmatrix} \tag{3.1}$$

in which $\boldsymbol{\sigma}_m = \langle \sigma_{mzz} \quad \sigma_{myy} \quad \tau_m \rangle^{\mathrm{T}}$ and $\mathbf{E}_a$ is the matrix of elastic constitutive properties Note that equation 3.1 is written for the web because of the plane stress assumption in *y*-*z* plane. However, the same constitutive relations can be applied to flanges by simply rotating the local coordinate system 90 degrees around the *z* axis, i.e., replacing subscripts 4 with 5 in *x*-*z* plane. To avoid repetition in the derivations of the constitutive equations the flange equations are not explicitly shown.

It should be noted that due to the assumption of non-extensible web or flange segments, the constitutive relations in equation 3.1 would cause unrealistic overly stiff behaviour and significant stresses would build up within the plane of the web due to Poisson ratio effect. In fact, the flanges are generally not restraint against extension and web are partially restraint depending on the boundary conditions. In fact, in-extensible cross-section assumption is a simplification of the beam theory. To continue with our formulation under the in-extensible cross-section assumption and yet avoid overly stiff behaviour, the stresses due to Poisson ratio effect can be eliminated by using the constitutive matrix below, i.e.,

$$\mathbf{E}_b = \begin{bmatrix} E & 0 & 0 \\ 0 & E & 0 \\ 0 & 0 & G \end{bmatrix} \tag{3.2}$$

Generally, for the web $\mathbf{E} = \mathbf{E}_a$ and for the flanges $\mathbf{E} = \mathbf{E}_b$ is used (e.g., see Pezeshky and Mohareb [19]). chapter 6 will introduce parametric studies and discussions on the consequences of the adopted constitutive relations.

3.2. Non-linear Equilibrium Equations Based on the principle of virtual work

The principle of virtual work can be written as

$$\delta\Pi = \delta W^{\text{int}} - \delta W^{\text{ext}} = 0 \tag{3.3}$$

where δW^{int} is the variation of the internal work, i.e.,

$$\delta W^{\text{int}} = \int_L \int_A \delta \boldsymbol{\varepsilon}_m^{\mathrm{T}} \boldsymbol{\sigma}_m \mathrm{d}A\mathrm{d}z \tag{3.4}$$

The virtual work done by the external loads can be written as

$$\delta W^{\text{ext}} = \delta \mathbf{d}^{\mathrm{T}} \mathbf{P}^{\text{ext}} \tag{3.5}$$

where $\mathbf{P}^{\text{ext}}$ is the vector of the external nodal forces and $\mathbf{d}$ is the vector of corresponding displacements. In the finite element form, we refer to vector $\mathbf{d}$ as the nodal displacement vector. A relation can be directly built between the variations of strains and the variations of nodal displacements in the form of

$$\delta \boldsymbol{\varepsilon}_m = \overline{\mathbf{s}} \mathbf{B}_n \delta \mathbf{d} \tag{3.6}$$

Details of the matrix $\mathbf{B}_n$ depends on the selected interpolation scheme which will be provided in Chapter 4. By the virtue of virtual work, we can write the nonlinear equilibrium equation as

$$\delta\Pi = \delta \mathbf{d}^{\mathrm{T}} \int_L \int_A \mathbf{B}_n^{\mathrm{T}} \overline{\mathbf{s}}^{\mathrm{T}} \boldsymbol{\sigma}_m \mathrm{d}A\mathrm{d}z - \delta \mathbf{d}^{\mathrm{T}} \mathbf{P}^{\text{ext}} = 0 \tag{3.7}$$

3.3. Consistent Linearization and Tangent Stiffness

The linearized equilibrium equations can be obtained from the Gateaux derivative of the functional in equation 3.7 as

$$\delta \mathbf{d} \cdot \nabla_{\mathbf{d}} \delta\Pi = \delta \mathbf{d} \cdot \nabla_{\mathbf{d}} \delta W^{\text{int}} = \delta \mathbf{d}^{\mathrm{T}} \int_L \int_A \mathbf{B}_n^{\mathrm{T}} \overline{\mathbf{s}}^{\mathrm{T}} \delta \boldsymbol{\sigma}_m \mathrm{d}A\mathrm{d}z + \delta \mathbf{d}^{\mathrm{T}} \int_L \int_A \delta \mathbf{B}_n^{\mathrm{T}} \overline{\mathbf{s}}^{\mathrm{T}} \boldsymbol{\sigma}_m \mathrm{d}A\mathrm{d}z = \delta \mathbf{d}^{\mathrm{T}} \mathbf{K}_t \delta \mathbf{d} \tag{3.8}$$

where $\mathbf{K}_t$ is the tangent stiffness matrix, i.e.

$$\delta\mathbf{d}^{\mathrm{T}}\mathbf{K}_t\delta\mathbf{d}=\delta\mathbf{d}^{\mathrm{T}}\int_L\int_A\mathbf{B}_n^{\mathrm{T}}\bar{\mathbf{s}}^{\mathrm{T}}\mathbf{E}\bar{\mathbf{s}}\mathbf{B}_n\mathrm{d}A\mathrm{d}z\delta\mathbf{d}+\delta\mathbf{d}^{\mathrm{T}}\int_L\int_A\delta\mathbf{B}_n^{\mathrm{T}}\bar{\mathbf{s}}^{\mathrm{T}}\boldsymbol{\sigma}_m\mathrm{d}A\mathrm{d}z \tag{3.9}$$

in which $\delta\boldsymbol{\sigma}_m=\mathbf{E}\delta\boldsymbol{\varepsilon}_m=\mathbf{E}\bar{\mathbf{s}}\mathbf{B}_n\delta\mathbf{d}$ was used. In equation 3.9, the variation of matrix $\mathbf{B}_n$ appear due to the second variation of the strain, i.e., $\delta^2\boldsymbol{\varepsilon}_m=\bar{\mathbf{s}}\delta\mathbf{B}_n\delta\mathbf{d}$. To obtain the stiffness matrix and the stress resultants, the integrations over the cross-sectional area A are performed at every integration point along the span L. This is because the displacement functions in equations 2.2 to 2.4 and accordingly, the strains $\boldsymbol{\varepsilon}_m$, the matrix $\mathbf{B}_n$ and the stresses $\boldsymbol{\sigma}_m$ are general functions of the cross-sectional coordinates as well as the axial coordinates. Thus, in equation 3.8 both $\mathbf{B}_n$ or $\boldsymbol{\sigma}_m$ are shown inside the first integral over the cross-section A as they cannot be analytically carried out of the integral. The $\mathbf{B}_n$ matrix generally depends on the displacement vector $\mathbf{d}$ which can be decomposed into two components as $\mathbf{B}_n=\mathbf{B}_l+\mathbf{B}_G$, where $\mathbf{B}_l$ is the component that is independent of $\mathbf{d}$, i.e., $\delta\boldsymbol{\chi}_L=\mathbf{B}_l\delta\mathbf{d}$ and $\delta\mathbf{B}_l=0$. The component $\mathbf{B}_G$ can be obtained from the relation $\mathbf{A}\delta\boldsymbol{\chi}_A=\mathbf{B}_G\delta\mathbf{d}$, i.e. $\mathbf{B}_G=\mathbf{A}\mathbf{N}_B$ and thus, $\mathbf{N}_B$ is such that $\delta\boldsymbol{\chi}_A=\mathbf{N}_B\delta\mathbf{d}$. The second term in equation 3.9 can be re-written such that

$$\delta\mathbf{B}_G{}^{\mathrm{T}}\bar{\mathbf{s}}^{\mathrm{T}}\boldsymbol{\sigma}_m=\mathbf{N}_B{}^{\mathrm{T}}\mathbf{M}_G\mathbf{N}_B\delta\mathbf{d} \tag{3.10}$$

in which $\mathbf{M}_G$ is a symmetrical matrix which can be written as

$$\mathbf{M}_G=\mathbf{G}^{\mathrm{T}}\mathbf{t}^{\mathrm{T}}\bar{\mathbf{s}}^{\mathrm{T}}\boldsymbol{\sigma}_m \tag{3.11}$$

As a result, the tangent stiffness matrix is $\mathbf{K}_t=\int_L\int_A\left(\mathbf{B}_l^{\mathrm{T}}+\mathbf{B}_G^{\mathrm{T}}\right)\bar{\mathbf{s}}^{\mathrm{T}}\mathbf{E}\bar{\mathbf{s}}\left(\mathbf{B}_l+\mathbf{B}_G\right)+\mathbf{N}_B{}^{\mathrm{T}}\mathbf{M}_G\mathbf{N}_B\mathrm{d}A\mathrm{d}z$.

3.4. Linearization Buckling Analysis

The equations of the linearized buckling analysis can be obtained from equation 3.9 by neglecting the pre-buckling deformations as

$$\mathbf{K}_e\delta\mathbf{d}_b-\lambda\mathbf{K}_g\delta\mathbf{d}_b=0 \tag{3.12}$$

in which

$$\mathbf{K}_e = \int_L \int_A \mathbf{B}_l^{\mathrm{T}} \bar{\mathbf{s}}^{\mathrm{T}} \mathbf{E} \bar{\mathbf{s}} \mathbf{B}_l \mathrm{d}A\mathrm{d}z \qquad 3.13$$

is the elastic stiffness matrix without the pre-buckling deformation effects, i.e. $\mathbf{B}_G = 0$ and

$$\mathbf{K}_g = \int_L \int_A \mathbf{N}_B{}^{\mathrm{T}} \mathbf{M}_G \mathbf{N}_B \mathrm{d}A\mathrm{d}z \qquad 3.14$$

is the geometric stiffness matrix. In equation 3.12, λ is the buckling load factor and $\delta\mathbf{d}_b$ is the corresponding eigenvector. The explicit expressions of the stiffness matrices depend on the interpolation scheme which is explained in Chapter 4. It should also be noted that the discretized equilibrium equations have been presented only in the context of a single element model. However, standard finite element assemblage procedures can be easily employed for structural models of multiple elements. Also note that proper boundary conditions need to be imposed. Details of the assemblage and the boundary condition imposition procedures are not presented herein.

4. Chapter 4: Finite Element Formulation

4.1. Interpolation Function

A beam type finite element with nodes only at both ends of the element is developed. The components of an element's nodal displacement vector shown in Figure 4.1 can be written as

$$\mathbf{d}=\left\langle w_1 \quad v_1 \quad \phi_{x1} \quad u_{B1} \quad \phi_{yB1} \quad \phi_{zB1} \quad \psi_{B1} \quad u_{T1} \quad \phi_{yT1} \quad \phi_{zT1} \quad \psi_{T1} \quad w_2 \quad v_2 \quad \phi_{x2} \quad u_{B2} \quad \phi_{yB2} \quad \phi_{zB2} \quad \psi_{B2} \quad u_{T2} \quad \phi_{yT2} \quad \phi_{zT2} \quad \psi_{T2} \right\rangle^{\mathrm{T}} \tag{4.1}$$

in which, the first eleven components are defined at the front end as shown in Figure 4.1 and the last eleven components are at the back end.

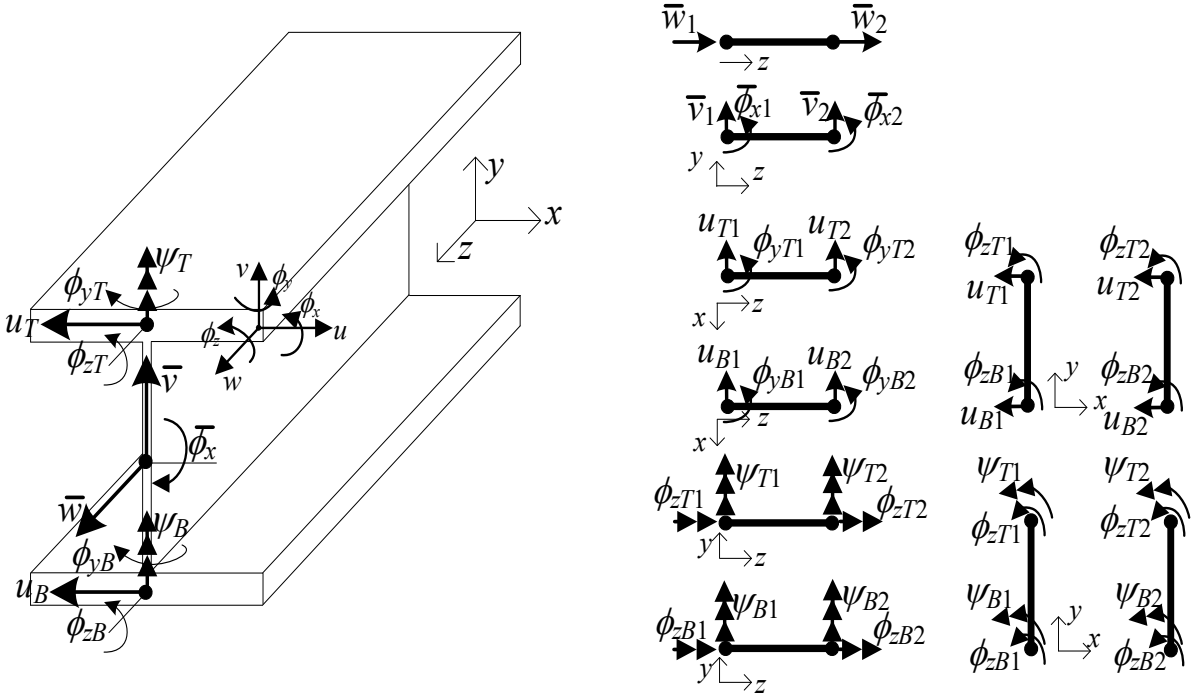

Figure 4.1 Nodal displacements according to interpolation scheme – see ref [37]

Accordingly, element displacement field vector becomes

$$\mathbf{u}=\left\langle \bar{w}(z) \quad \bar{v}(z) \quad \bar{\phi}_x(z) \quad u(y,z) \quad \phi_y(y,z) \quad \phi_z(y,z) \quad \psi(y,z) \right\rangle^{\mathrm{T}} = \tilde{\mathbf{N}}(y,z)\tilde{\mathbf{d}} = \mathbf{N}(y,z)\mathbf{d} \tag{4.2}$$

in which the matrix of shape functions was introduced as

$$\tilde{\mathbf{N}}(y,z)=\begin{bmatrix} \mathbf{N} & \mathbf{0} & \mathbf{0} & \mathbf{0} & \mathbf{0} & \mathbf{0} \\ \mathbf{0} & \mathbf{L}_f & \mathbf{0} & \mathbf{0} & \mathbf{0} & \mathbf{0} \\ \mathbf{0} & \mathbf{M}_f & \mathbf{0} & \mathbf{0} & \mathbf{0} & \mathbf{0} \\ \mathbf{0} & \mathbf{0} & \hat{H}_1\mathbf{L}_u & \hat{H}_2\mathbf{L}_u & \hat{H}_3\mathbf{L}_u & \hat{H}_4\mathbf{L}_u \\ \mathbf{0} & \mathbf{0} & \hat{H}_1\mathbf{M}_u & \hat{H}_2\mathbf{M}_u & \hat{H}_3\mathbf{M}_u & \hat{H}_4\mathbf{M}_u \\ \mathbf{0} & \mathbf{0} & \dot{H}_1\mathbf{L}_t & \dot{H}_2\mathbf{L}_t & \dot{H}_3\mathbf{L}_t & \dot{H}_4\mathbf{L}_t \\ \mathbf{0} & \mathbf{0} & \dot{H}_1\mathbf{M}_t & \dot{H}_2\mathbf{M}_t & \dot{H}_3\mathbf{M}_t & \dot{H}_4\mathbf{M}_t \end{bmatrix} \qquad 4.3$$

Note that in equation 4.2, vector $\tilde{\mathbf{d}}$ is used instead of $\mathbf{d}$ to change the order of displacement vector components so that the matrix of shape functions can be expressed in an organized compact form as in equation 4.3. In the nodal displacement vector $\tilde{\mathbf{d}}$, the components are collected in the order of axial, vertical, bottom flange lateral, bottom flange twist, top flange lateral and top flange twist related terms, respectively i.e.,

$$\tilde{\mathbf{d}}=\langle \mathbf{w} \;\vdots\; \mathbf{\Omega} \;\vdots\; \mathbf{\Lambda}_B \;\vdots\; \mathbf{\Gamma}_B \;\vdots\; \mathbf{\Lambda}_T \;\vdots\; \mathbf{\Gamma}_T \rangle^{\mathrm{T}} \qquad 4.4$$

in which $\mathbf{w}=\langle w_1 \quad w_2 \rangle^{\mathrm{T}}$, $\mathbf{\Omega}=\langle v_1 \quad \phi_{x1} \quad v_2 \quad \phi_{x2} \rangle^{\mathrm{T}}$, $\mathbf{\Lambda}_B=\langle u_{B1} \quad \phi_{yB1} \quad u_{B2} \quad \phi_{yB2} \rangle^{\mathrm{T}}$, $\mathbf{\Gamma}_B=\langle \phi_{zB1} \quad \psi_{B1} \quad \phi_{zB2} \quad \psi_{B2} \rangle^{\mathrm{T}}$, $\mathbf{\Lambda}_T=\langle u_{T1} \quad \phi_{yT1} \quad u_{T2} \quad \phi_{yT2} \rangle^{\mathrm{T}}$ and $\mathbf{\Gamma}_T=\langle \phi_{zT1} \quad \psi_{T1} \quad \phi_{zT2} \quad \psi_{T2} \rangle^{\mathrm{T}}$.

In equation 4.3, the axial displacement field in z direction is interpolated by using usual linear functions. Thus, the components of the vector $\mathbf{N}$ in equation 4.3 can be explicitly written as

$$N_1=\frac{L-z}{L} \qquad N_2=\frac{z}{L} \qquad 4.5$$

For the transverse displacement and rotational fields around the x axis, the components of the vectors $\mathbf{L}_f$ and $\mathbf{M}_f$ used in equation4.3 can be written as

$$L_{f1}=1-\frac{z\alpha_f}{L(1+\alpha_f)}-\frac{3z^2}{L^2(1+\alpha_f)}+\frac{2z^3}{L^3(1+\alpha_f)} \qquad L_{f2}=\frac{z(1+0.5\alpha_f)}{(1+\alpha_f)}-\frac{2z^2(1+0.25\alpha_f)}{L(1+\alpha_f)}+\frac{z^3}{L^2(1+\alpha_f)} \qquad 4.6$$

$$L_{f3}=\frac{z\alpha_f}{L(1+\alpha_f)}+\frac{3z^2}{L^2(1+\alpha_f)}-\frac{2z^3}{L^3(1+\alpha_f)} \qquad L_{f4}=-\frac{0.5z\alpha_f}{(1+\alpha_f)}+\frac{z^2(0.5\alpha_f-1)}{L(1+\alpha_f)}+\frac{z^3}{L^2(1+\alpha_f)}$$

and

$$M_{f1}=-\frac{6z}{L^2\left(1+\alpha_f\right)}+\frac{6z^2}{L^3\left(1+\alpha_f\right)} \qquad M_{f2}=1-\frac{z\left(4+\alpha_f\right)}{L\left(1+\alpha_f\right)}+\frac{3z^2}{L^2\left(1+\alpha_f\right)} \qquad 4.7$$

$$M_{f3}=\frac{6z}{L^2\left(1+\alpha_f\right)}-\frac{6z^2}{L^3\left(1+\alpha_f\right)} \qquad M_{f4}=\frac{z\left(\alpha_f-2\right)}{L\left(1+\alpha_f\right)}+\frac{3z^2}{L^2\left(1+\alpha_f\right)}$$

where α_f is a shear parameter. Components of the vectors $\mathbf{L}_u$, $\mathbf{M}_u$, $\mathbf{L}_t$ and $\mathbf{M}_t$ in in equation 4.3 are identical to those given for $\mathbf{L}_f$ and $\mathbf{M}_f$ in equations 4.6 and 4.7, except the fact that α_f is replaced with α_u and α_t for the interpolation of lateral and torsional displacements, respectively. By default shear parameters are selected as selected as $\alpha_f=12EI_{xx}/GA_yL^2$ and $\alpha_u=\alpha_t=12EI_{yy}/GA_xL^2$ in which $GA_x=\int_{A_x}\bar{Q}_{44}^{(k)*}\mathrm{d}A$, $GA_y=\int_{A_y}\bar{Q}_{44}^{(k)*}\mathrm{d}A$ A_x and A_y are shear areas in x and y directions, respectively, $EI_{xx}=\int_{A}\bar{Q}_{33}^{(k)*}y^2\mathrm{d}A$, $EI_{yy}=\int_{A}\bar{Q}_{33}^{(k)*}x^2\mathrm{d}A$ and L is the span of the element. The selected interpolation functions allow first order shear deformation effects to be captured based on the fact that in general $\bar{u}'-\bar{\phi}_y\neq 0$, $\bar{v}'+\bar{\phi}_x\neq 0$ and $\bar{\psi}-\bar{\phi}_z'\neq 0$ which generates linear shear strains in equation 2.14 unless $\alpha_f=\alpha_u=\alpha_t=0$. It is interesting to note, however, that in finite element formulations where multiple fields are coupled numerical locking is a potential problem which may cause degradation in optimal convergence rate. So-called kinematic interpolation scheme has been previously suggested to alleviate shear-locking in Timoshenko beam elements by Tessler and Dong (1981). They have used interdependent polynomial orders for the deflection and rotations fields which were related to each other using Euler-Bernoulli-type kinematic constraints so that a locking-free analysis can be performed with two-node Timoshenko beam elements when $\alpha_f\to 0$. A similar idea re-appeared in Reddy (1997), where the interdependent polynomial functions were directly obtained from the homogenous solution of the equilibrium equations of the Timoshenko beam formulation, which led to interpolation functions for the transverse deflection and rotation fields as given in equations 4.6 and 4.7, respectively.

In equation 4.3, the interpolation along the web is based on Hermitian functions, i.e.

$$H_1=1-\frac{3(y-y_B)^2}{h_w^2}+\frac{2(y-y_B)^3}{h_w^3} \qquad H_2=(y-y_B)-\frac{2(y-y_B)^2}{h_w}+\frac{(y-y_B)^3}{h_w^2} \qquad 4.8$$

$$H_3=\frac{3(y-y_B)^2}{h_w^2}-\frac{2(y-y_B)^3}{h_w^3} \qquad H_4=-\frac{(y-y_B)^2}{h_w}+\frac{(y-y_B)^3}{h_w^2}$$

where $h_w=y_T-y_B$. The components of the vector $\hat{H}_i$ in equation 4.3 can be written as

$$\hat{H}_i=H_i-\kappa(y-0.5h_w)\dot{H}_i(y_0) \qquad 4.9$$

where $i=1,\cdots,4$ and $y_0=(y_T+y_B)/2$. Indeed, the additions to Hermitian functions in equation 4.9 are not activated in the Distortional Beam Formulation (DBF) developed herein and thus, $\kappa=0$ is used. However, when rigid web assumption is imposed as a special case of the distortional beam formulation, interpolation can be modified by using $\kappa=1$ so that $0.5h_w\left(\hat{H}_3-\hat{H}_1\right)+\hat{H}_2+\hat{H}_4=0$ which results with a standard interpolation scheme for the rigid-web Thin-walled beam formulation as explained in the next section.

It is important to note that when shear deformations are included the shape functions along the beam axis depend on the cross-sectional properties due to the involvement of the parameters α_f, α_u and β. However, cross-sectional properties are not meaningful for the lateral and torsional behaviour unless the cross-section is rigid, which is generally not the case in the distortional beam formulation presented herein. The flexibility of the web influences the lateral-torsional behaviour. Therefore, we modify the shape functions for lateral and torsional behaviour by proposing a formula for μ considering the flexibility of the web, i.e.,

$$\mu=\frac{GJ_dL^2}{EI_{\omega\omega}+GJ_dL^2} \qquad 4.10$$

in which L is the span of the element. Equation 4.10 is developed based on the fact that contribution of the St. Venant's uniform torsion component $T_{sv}=-GJ_d\bar{\phi}_z'$ within the total torsion carried, i.e., $T=T_{sv}+T_w$ is an indication of web rigidity. The warping torsion $T_w=EI_{\omega\omega}\bar{\phi}_z'''$ is due to shear force couple V_{Tf} and V_{Bf} acting on the top and bottom flanges, respectively. The St. Venant's uniform

torsion component T_{sv} (Figure 4.2a) increases as the web becomes thicker and the beam becomes longer, in which case distortion of the web diminishes. In the limit case of zero-web rigidity St. Venant torsion also vanishes both on the flanges and the web. The twist rates of flanges vanish because of the loss of interaction between the flanges and as a result the total torsion is carried only by the warping torsion T_w. This is consistent with the fact that in the limit case of $\mu \to 0$, the St. Venant component is negligible comparison to the warping torsion and the corresponding the differential equation becomes $EI_{\omega\omega}\bar{\phi}_z^{iv} = \bar{t}(z)$. It can be verified that for $\mu \to 0$, one obtains $kL \to 0$, in which case the interpolation functions become Hermitian polynomials (see [38]), which is the solution for $\bar{\phi}_z^{iv} = 0$. On the other hand, in the case of $\mu \to 1$ the warping torsion is negligible comparison to the St. Venant component and the corresponding differential equation becomes $-GJ_d\bar{\phi}_z'' = \bar{t}(z)$. It can be verified that for $\mu \to 1$, one obtains $kL \to \infty$, in which case the interpolation functions become linear (see [38]), which is the solution for $\bar{\phi}_z'' = 0$. Therefore, we interpolate μ between the two limit cases shown in Figure 4.2 according to how the total torsion is shared between the St. Venant torsion and warping torsion components.

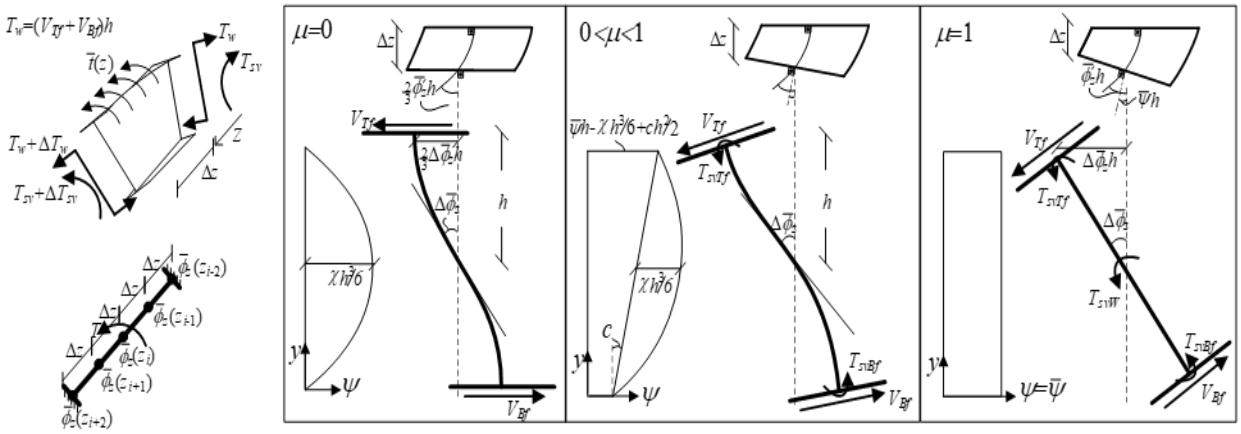

Figure 4.2 Components of torsional moment and their dependence on web rigidity

By using the expression for warping and St.Venant's torsion of the Vlasov [28] in finite difference form and considering symmetry conditions at z_i (Figure 4.2) i.e., $\bar{\phi}_z'(z_i) \approx -\bar{\phi}_z'''(z_i)\Delta z^2$, one obtains

$$T_w \approx \frac{EI_{\omega\omega}}{EI_{\omega\omega} + GJ_d \Delta z^2} T \qquad T_{sv} \approx \frac{GJ_d \Delta z^2}{EI_{\omega\omega} + GJ_d \Delta z^2} T \tag{4.11}$$

From the definition of μ as the contribution of the St. Venant component comparison to the total torsion carried, i.e., $T_{sv} \approx \mu T$ equation 4.11 produces equation 4.10. It is our observation that the upper bounds that is provided by equation 4.11 generally suppresses the shear deformation effect for the torsional behaviour. Therefore, when distortional deformations are activated the shear effects are not significant in the tortional behaviour.

4.2. Thin-walled Beam Formulation as a special case

Bending of the web within the plane of the cross-section can be suppressed by using Multiple-Point Constraints (MPCs). As the web is assumed rigid in the plane of the cross-section, the number of angle of twist $\bar{\phi}_z$ and warping $\bar{\psi}$ Degrees-Of-Freedoms (DOFs) should be reduced from two to one at both ends of the beam element. As a result, the DOFs related to lateral displacement $\bar{u}$ and rotation angle $\bar{\phi}_y$ are reduced from two to one at both ends as top and bottom DOFS can be related as

$$\bar{\phi}_{z1} = \phi_{zB1} = \phi_{zT1} \qquad \frac{u_{T1} - u_{B1}}{h_w} = \phi_{zT1} \qquad \bar{\psi}_1 = \psi_{B1} = \psi_{T1} \qquad \frac{\bar{\phi}_{y1} - \phi_{yB1}}{h_w} = \bar{\psi}_1 \tag{4.12}$$

$$\bar{\phi}_{z2} = \phi_{zB2} = \phi_{zT2} \qquad \frac{u_{T2} - u_{B2}}{h_w} = \phi_{zT2} \qquad \bar{\psi}_2 = \psi_{B2} = \psi_{T2} \qquad \frac{\bar{\phi}_{y2} - \phi_{yB2}}{h_w} = \bar{\psi}_2$$

From equation 4.12, one obtains the following eight conditions which reduces the 22DOF element to a 14DOF element, i.e.,

$$u_{T1} = \bar{u}_1 + \frac{h_w \bar{\phi}_{z1}}{2} \qquad u_{B1} = \bar{u}_1 - \frac{h_w \bar{\phi}_{z1}}{2} \qquad \phi_{yT1} = \bar{u}_1 + \frac{h_w \bar{\psi}_1}{2} \qquad \phi_{yB1} = \bar{u}_1 - \frac{h_w \bar{\psi}_1}{2} \tag{4.13}$$

$$u_{T2} = \bar{u}_2 + \frac{h_w \bar{\phi}_{z2}}{2} \qquad u_{B2} = \bar{u}_2 - \frac{h_w \bar{\phi}_{z2}}{2} \qquad \phi_{yT2} = \bar{u}_2 + \frac{h_w \bar{\psi}_2}{2} \qquad \phi_{yB2} = \bar{u}_2 - \frac{h_w \bar{\psi}_2}{2}$$

For implementation purposes equation 4.13 can be introduced using a constraint matrix $\tilde{\mathbf{T}}$ such that

$$\tilde{\mathbf{d}} = \tilde{\mathbf{T}}\hat{\mathbf{d}} \tag{4.14}$$

in which

$$\hat{\mathbf{d}}=\langle \mathbf{w} \mid \mathbf{\Omega} \mid \mathbf{\Lambda} \mid \mathbf{\Gamma} \rangle^{\mathrm{T}} \tag{4.15}$$

and $\mathbf{w}=\langle w_1 \quad w_2 \rangle^{\mathrm{T}}$, $\mathbf{\Omega}=\langle v_1 \quad \phi_{x1} \quad v_2 \quad \phi_{x2} \rangle^{\mathrm{T}}$, $\mathbf{\Lambda}=\langle u_1 \quad \phi_{y1} \quad u_2 \quad \phi_{y2} \rangle^{\mathrm{T}}$, $\mathbf{\Gamma}=\langle \phi_{z1} \quad \psi_1 \quad \phi_{z2} \quad \psi_2 \rangle^{\mathrm{T}}$.

The matrix $\tilde{\mathbf{T}}$ in equation 4.14 can be obtained by using equations 4.4, 4.13 and 4.15 as

$$\tilde{\mathbf{T}}=\left[\begin{array}{c|c|c|c} \mathbf{I}_{2\times2} & \mathbf{0}_{2\times4} & \mathbf{0}_{2\times4} & \mathbf{0}_{2\times4} \\ \hline \mathbf{0}_{4\times2} & \mathbf{I}_{4\times4} & \mathbf{0}_{4\times4} & \mathbf{0}_{4\times4} \\ \hline \mathbf{0}_{4\times2} & \mathbf{0}_{4\times4} & \mathbf{I}_{4\times4} & -0.5h_w\mathbf{I}_{4\times4} \\ \hline \mathbf{0}_{4\times2} & \mathbf{0}_{4\times4} & \mathbf{0}_{4\times4} & \mathbf{I}_{4\times4} \\ \hline \mathbf{0}_{4\times2} & \mathbf{0}_{4\times4} & \mathbf{I}_{4\times4} & 0.5h_w\mathbf{I}_{4\times4} \\ \hline \mathbf{0}_{4\times2} & \mathbf{0}_{4\times4} & \mathbf{0}_{4\times4} & \mathbf{I}_{4\times4} \end{array}\right] \tag{4.16}$$

It can be verified that under the assumption of rigid cross-section by using matrix $\tilde{\mathbf{T}}$ given in equation 4.16,the independent displacement field components can be reduced to seven as

$$\tilde{\mathbf{N}}\tilde{\mathbf{T}}\hat{\mathbf{d}}=\left[\begin{array}{c|c|c|c} \mathbf{N} & \mathbf{0} & \mathbf{0} & \mathbf{0} \\ \hline \mathbf{0} & \mathbf{L} & \mathbf{0} & \mathbf{0} \\ \hline \mathbf{0} & \mathbf{M} & \mathbf{0} & \mathbf{0} \\ \hline \mathbf{0} & \mathbf{0} & \mathbf{L} & \mathbf{0} \\ \hline \mathbf{0} & \mathbf{0} & \mathbf{M} & \mathbf{0} \\ \hline \mathbf{0} & \mathbf{0} & \mathbf{0} & \mathbf{L} \\ \hline \mathbf{0} & \mathbf{0} & \mathbf{0} & \mathbf{M} \end{array}\right]\left\{\begin{array}{c} \mathbf{w} \\ \hline \mathbf{\Omega} \\ \hline \mathbf{\Lambda} \\ \hline \mathbf{\Gamma} \end{array}\right\}=\left\{\begin{array}{c} \bar{w}(z) \\ \hline \bar{v}(z) \\ \hline \bar{\phi}_x(z) \\ \hline -\bar{u}(z) \\ \hline -\bar{\phi}_y(z) \\ \hline \bar{\phi}_z(z) \\ \hline \psi(z) \end{array}\right\} \tag{4.17}$$

in which $\tilde{\mathbf{N}}$ is as given in equation 4.3 and obtained by using $\kappa=1$ in equation 4.9. In obtaining equation 4.17, the following properties of the shape functions have been used for when $\kappa=1$, i.e.

$$\left(H_1+H_3\right)=1 \qquad \left(\dot{H}_1+\dot{H}_3\right)=0 \qquad 0.5h_w\left(\hat{H}_3-\hat{H}_1\right)+\hat{H}_2+\hat{H}_4=0 \tag{4.18}$$

$$0.5h_w\left(\dot{H}_3-\dot{H}_1\right)+\dot{H}_2+\dot{H}_4=1 \qquad 0.5h_w\left(\ddot{H}_3-\ddot{H}_1\right)+\ddot{H}_2+\ddot{H}_4=0$$

Indeed, equation 4.17 is a standard interpolation scheme for a 2-node, 14DOF Thin-walled beam finite element formulations, e.g. [3-8]. The nodal DOF-generalized displacement field relations obtained in equation 4.17 assume non-bendable rigid web kinematics. The strain expressions for the thin-walled beam with rigid web can be obtained simply by replacing ϕ_y with $\bar{\phi}_y$ and ϕ_z with $\bar{\phi}_z$ in equations 2.15-2.17. However, it is important to note that in equation 2.17, the lateral displacement expression considering rigid web, i.e., $u = \bar{u} - \left(y - a_{Gy}\right)\bar{\phi}_z$ should be used to obtain the second order strains of the Thin-walled beam with rigid web correctly. Thus, under rigid web assumption the second order strain expression in equation 2.17 becomes

$$\bar{e}_{zz} = \frac{1}{2}\left(\bar{u}'^2 + \bar{v}'^2\right) - a_{Gx}\bar{v}'\bar{\phi}_z' - \frac{1}{2}x\left(\bar{v}''\bar{\phi}_z - \bar{v}'\bar{\phi}_z'\right) + \frac{1}{2}y\left(\bar{u}''\bar{\phi}_z - \bar{u}'\bar{\phi}_z'\right) + \frac{1}{2}\left[\left(x - a_{Gx}\right)^2 + \left(y - a_{Gy}\right)^2\right]\bar{\phi}_z'^2 \quad 4.19$$

5. Chapter 5: Case Studies

For the case studies various types of analysis options are employed including the developed Distortional Beam Formulation (DBF), the rigid web thin-walled beam formulation as a special case (TBF); and a Shell Element Formulation (SEF) formed by combining plate and membrane elements whose details are explained further. For accurate numerical integration 4-point Gauss integration along the beam span, 8-point Gauss integration along the contour direction and 20-point trapezoidal rule across the thickness were used. The material is assumed steel in all cases, therefore the modulus of elasticity and Poisson ratio were taken as E=200GPa and n=0.3, respectively.

5.1. The employed Shell Formulation (SEF)

The employed Shell Element Formulation has four-nodes and six-degree-of-freedom-per-node which is a combination of Discrete Kirchhoff Plate developed in [31] and the membrane with drilling degrees of freedom developed in [32]. For numerical integration 2x2 Gauss integration scheme is used as suggested for both membrane and plate components in [31] and [32]. The interpolation functions and implementation details of the SEF can be found for the buckling and nonlinear analyses in [33]. Similar shell formulations were formed for buckling analysis of thin-walled beams by combining plate and membrane elements in [34,35]. In SEF adopted herein the strains $\boldsymbol{\varepsilon}_s$ are due to linear plate bending deformations $\boldsymbol{\varepsilon}_b$, linear membrane in-plane deformations $\boldsymbol{\varepsilon}_i$ and second order membrane and plate bending action $\boldsymbol{\varepsilon}_N$, i.e.

$$\boldsymbol{\varepsilon}_s = \boldsymbol{\varepsilon}_b + \boldsymbol{\varepsilon}_i + \boldsymbol{\varepsilon}_N \tag{5.1}$$

where

$$\boldsymbol{\varepsilon}_b = -r\left\langle \frac{\partial \phi}{\partial z} \quad \frac{\partial \beta}{\partial q} \quad \frac{\partial \phi}{\partial q} + \frac{\partial \beta}{\partial z} \right\rangle^{\mathrm{T}} \tag{5.2}$$

$$\boldsymbol{\varepsilon}_i = \left\langle \frac{\partial w}{\partial z} \quad \frac{\partial u}{\partial q} \quad \frac{\partial w}{\partial q} + \frac{\partial u}{\partial z} \right\rangle^{\mathrm{T}} \tag{5.3}$$

And

$$\boldsymbol{\varepsilon}_N = \frac{1}{2}\left\langle \left(\frac{\partial v}{\partial z}\right)^2 + \left(\frac{\partial u}{\partial z}\right)^2 \quad \left(\frac{\partial v}{\partial q}\right)^2 + \left(\frac{\partial w}{\partial q}\right)^2 \quad 2\frac{\partial v}{\partial z}\frac{\partial v}{\partial q} \right\rangle^{\mathrm{T}} \tag{5.4}$$

in which the strain components in equations 5.2 to 5.4 are given in terms of local coordinates z, q, r, deflections w, u, v and rotations b, f previously introduced in Figure 2.4.

We first compare the SEF results with the Euler-Buckling formula so that reliability of the SEF used for comparison purposes can be confirmed. For that purpose, a thin strip is subjected to axial compressive load. To prevent local buckling rigid links are imposed using MPCs to tie the neighbouring nodes to load application points and support locations in the middle node as shown in Figure 5.1. Support conditions in the case of Figure 5.1a are kept minimal to impose simply supported boundary conditions and allow buckling about the weak axis Y. In the second case as shown in Figure 5.1c extra supports are imposed to prevent weak axis buckling so that the buckling occurs about the strong axis Z. While in the first case only plate component of the shell element is active, in the second case only membrane component is active. In both cases, 2 elements were used across the width and alternatively 8 or 16 elements were used along the span. The thickness of the strip is t=1mm, the width is a=40mm and the is span L=400mm. The Euler formula, i.e. $P_{cr} = \pi^2 EI/L^2$ predicts the weak and strong axes buckling loads as $41.12N$ and $65.79\times10^3 N$, respectively. The corresponding buckling load predictions by the SEF model are $41.65N$ and $66.74\times10^3 N$ when 8 elements are used along the span, respectively. Thus, the error is around 1.3% and 1.4% respectively. When the number of elements along the span are increased to 16 the weak and strong axis buckling loads predicted by the SEF model are $41.29N$ and $66.256\times10^3 N$, respectively. The error reduces to less than 0.8% in both cases.

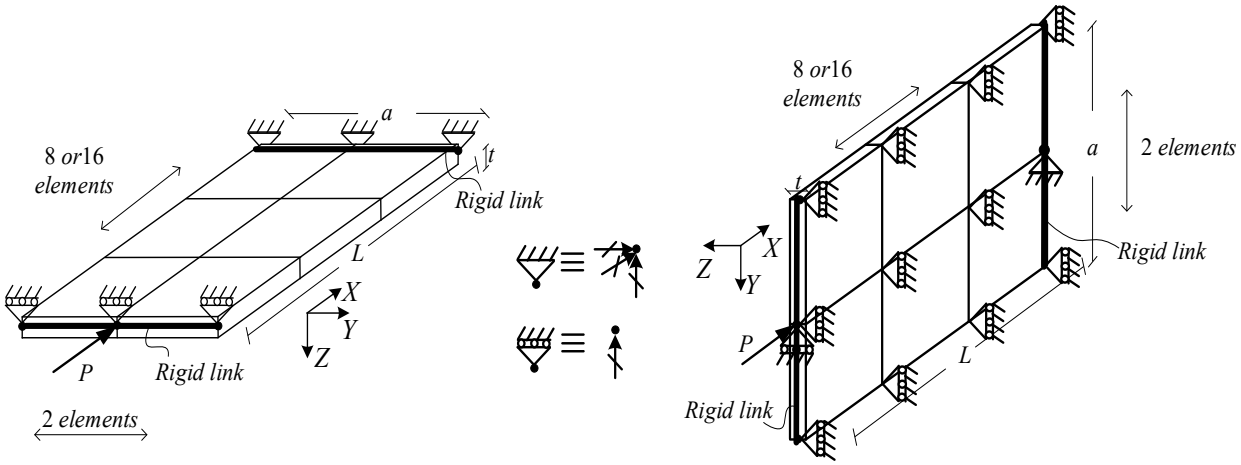

(a) Plate under compression **(b) Support definitions** **(c) Membrane under compression**

Figure 5.1 Support and loading conditions for buckling analysis of plate and membrane models

5.2. Numerical Examples

Several numerical examples are solved based on the present theory to assess the validity and illustrate the capability of the present formulations. Obtained results compared against various solutions including Shell FEA, Thin-walled beam, and conventional beam theories such as Euler-Bernoulli which neglects shear deformation effect and Timoshenko capturing shear deformability to show the validity and correctness of the implementation of the distortional beam solution. In all examples, a mono symmetric WRF1000×340 cross-section is considered (Figure 5.3a) with steel material properties of $E = 200{,}000\ MPa, \nu = 0.3$.

5.2.1 Example 1: Cantilever beam under tip load

For verification of the results according to the present solution, a 6.00 m span cantilever beam is subjected to a transverse tip load *P=1,000 KN* at the mid-surface of the beam, Figure 5.2. A mono-symmetric WRF1000×340 steel cross-section is selected which the cross-sectional dimensions are shown in Figure 5.3a, and the transverse displacements and strong axis rotations are predicted through present theory in the existence of both distortional and shear effect and compared them against various solutions (see Figure 5.5). The predicted response for transverse displacement through Euler-Bernoulli beam theory can obtain from $V_{EB} = -\frac{PZ^2}{6EI_x}(3L - Z)$ which ignores shear deformation effects, and under the Timoshenko beam theory the displacement by considering shear correction factor K_{xx} can be calculated as $V_T = -\frac{PZ^2}{6EI_x}(3L - Z) - \frac{PZ}{GAK_{xx}}$. In the Shell FE modelling, the cross-section is divided into six elements buy assuming two elements for the web and two elements for each top and bottom flange (see Figure 5.3b), and 20 elements are taken along the cantilever beam span.

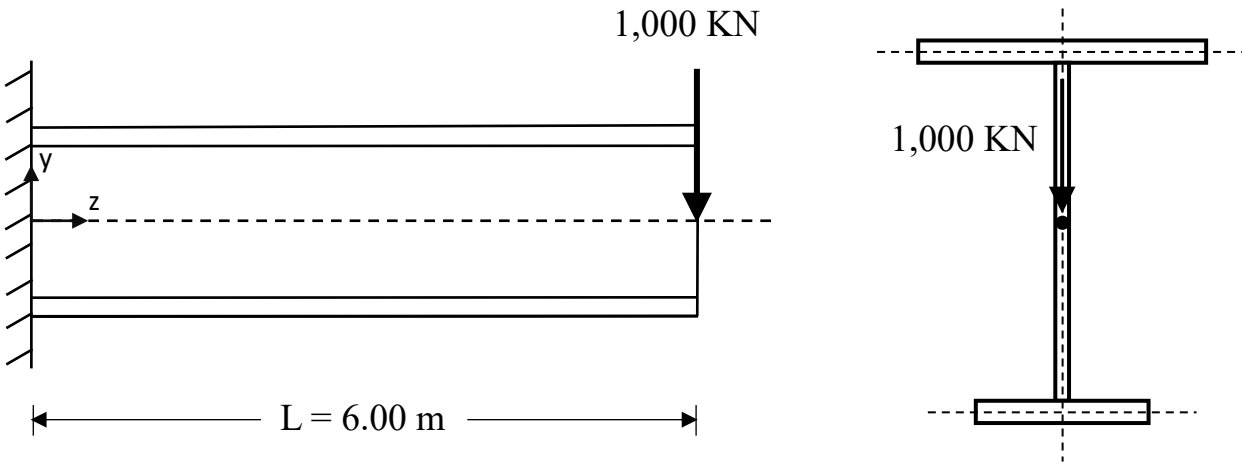

Figure 5.2 Tip load at the mid-surface of the cantilever

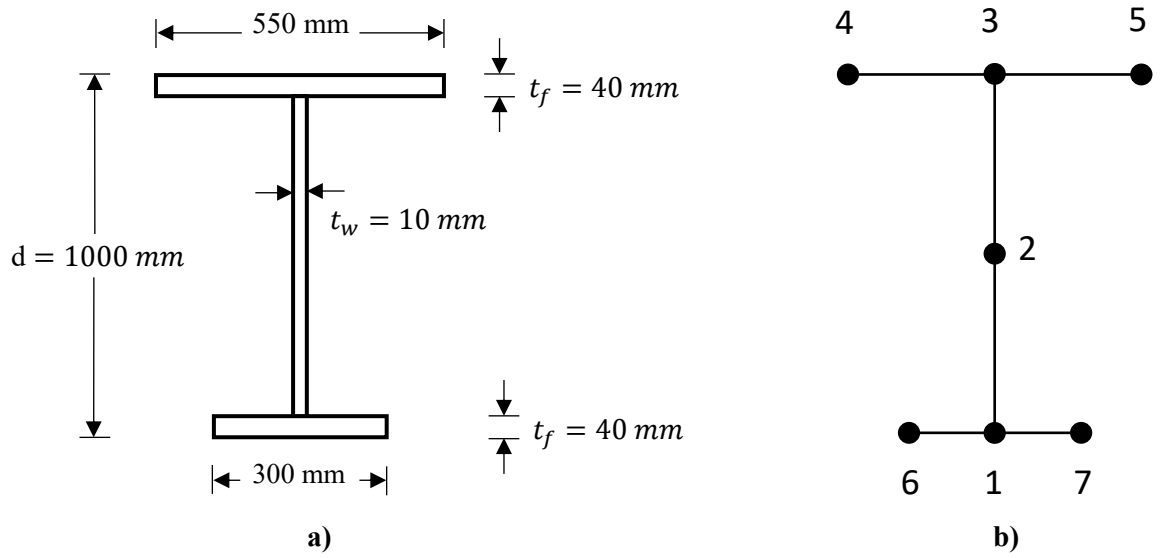

Figure 5.3 a) WRF1000×340 Cross-sectional Geometry, b) Cross-section finite element mesh

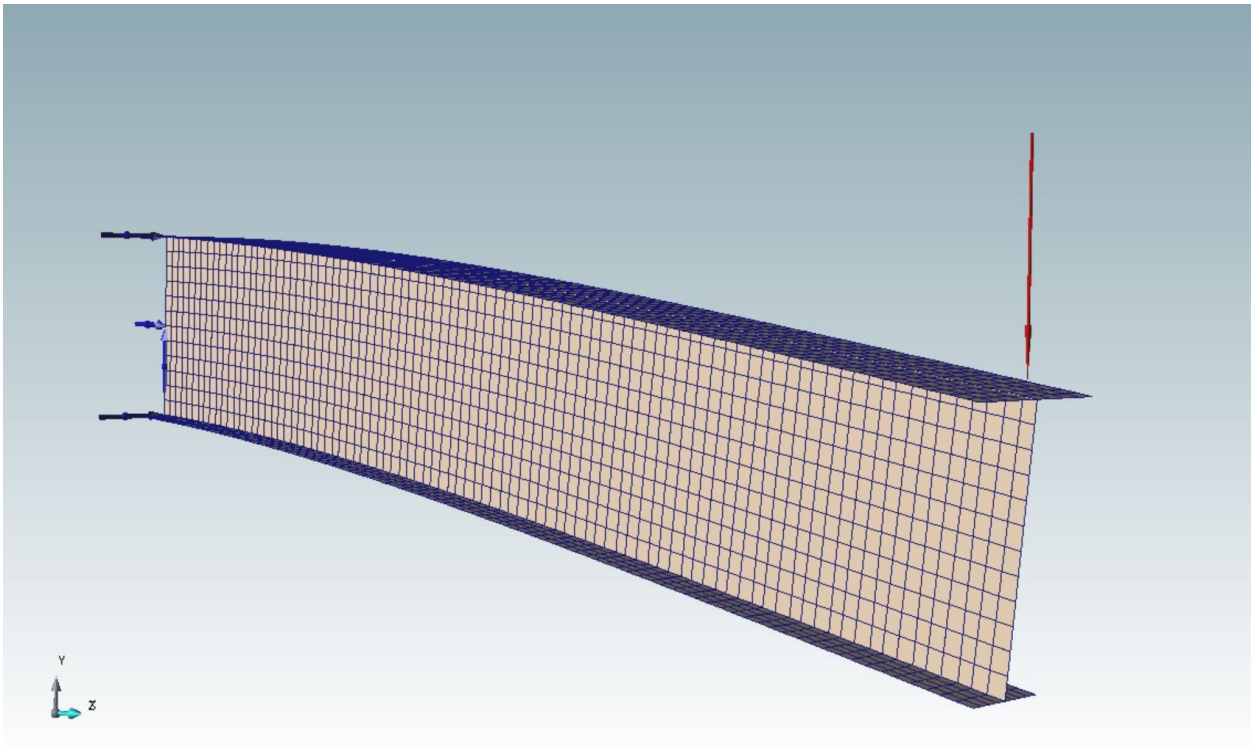

Figure 5.4 Finite element modelling of the cantilever beam under a tip load

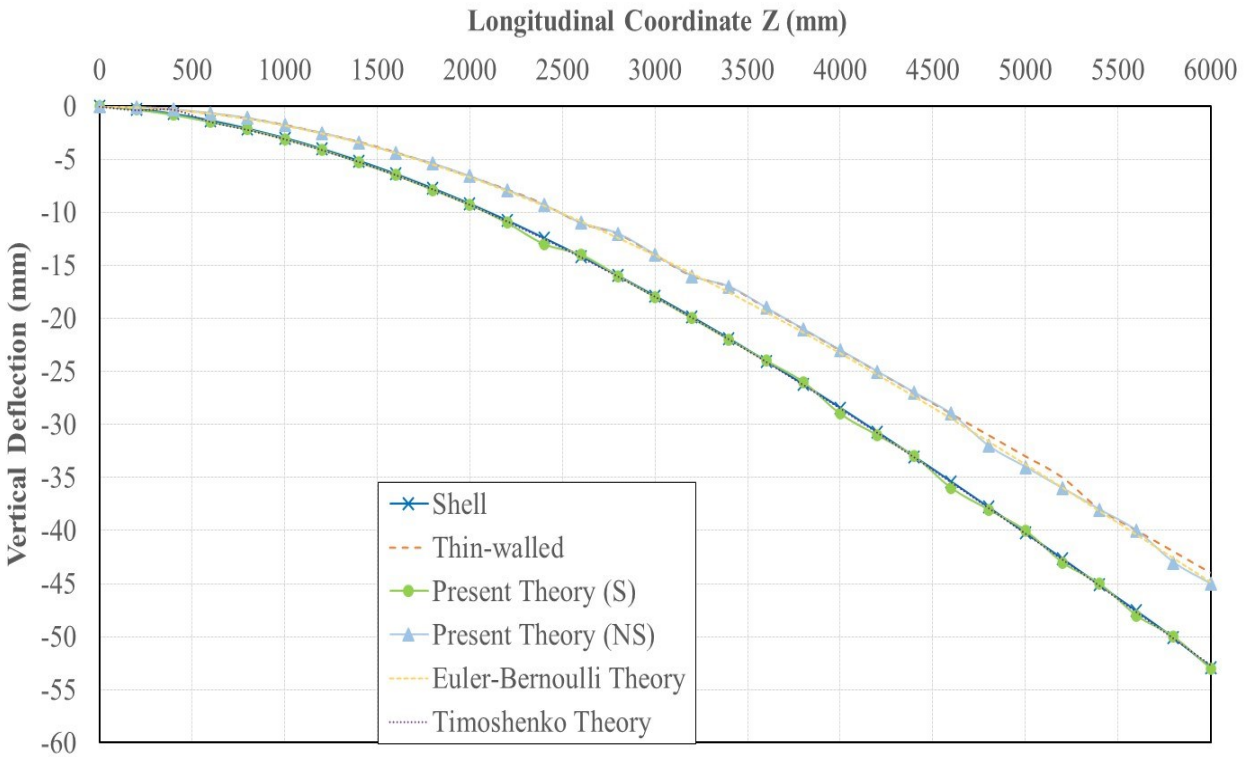

Figure 5.5 Vertical deflection for transversely loaded cantilever

Under Timoshenko theory, the mentioned shear correction factor can be obtained as below:

$$K_{xx} = \left[\left(\frac{A}{I^2}\right)\int\left(\frac{{Q_x}^2(s)}{t(s)}\right)ds\right]^{-1} = 0.23 \ \left(e.g., Iyer\ (2005)\right).$$

Where $A =$ Cross-sectional area

$I =$ Second area moment of inertia about bending axis

$Q_x =$ First area moment of inertia above or below the centroidal axis about x axis

$t(s) =$ Thickness of the section

The employed shell-type element formulation has four nodes with six-degrees of freedom per node which is composed of Discrete Kirchhoff Plate and membrane element with drilling degrees of freedom which can be result in 24 degrees of freedom for each shell element.

In all above-mentioned solutions, the vertical displacement along the cantilever beam is measured at the middle of the web, and the vertical displacement at the tip of the cantilever beam is compared against all solutions in Table 5-1, where the present theory is perfectly agreed with the shell FE

solution within 0.21% and shows a good agreement with the Timoshenko beam theory. Additionally, the Thin-walled beam solution and the Euler-Bernoulli beam theory demonstrates lower response predictions since they neglect shear deformation effects which can be significant for beams with long web. The applied load at the tip of the cantilever beam causes rotation around the strong axis due to bending which is provided Figure 5.6 as a comparison among all other solution in the literature. It can be seen a well agreement between the present theory and other solutions in terms of angle of rotation due to strong axis bending of the cantilever beam.

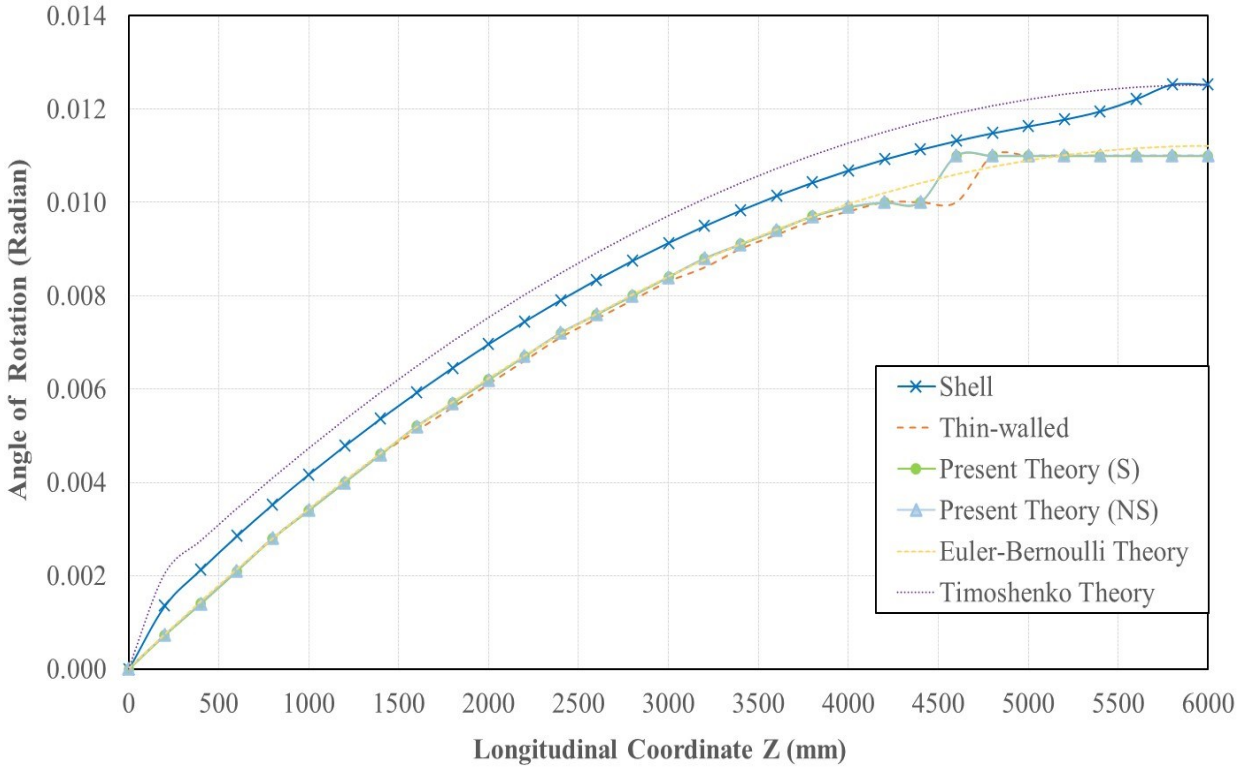

Figure 5.6 Angle of rotation due to strong axis bending of the cantilever beam

Table 5-1. Tip deflection at the mid-surface of the 6.00m span cantilever

Type of Solution	Vertical Displacement (mm)	Percentage difference relative to Shell FE solution
Shell FE	52.889	0%
Thin-walled Beam	44	16.81%
Euler-Bernoulli Beam	44.888	15.13%
Timoshenko Beam	52.676	0.403%
Present Theory (D+S)	53	-0.21%

5.2.2 Example 2: Cantilever beam under weak axis bending

A 6.00 m span cantilever with mono symmetric WRF1000×340 steel cross-section is subjected to two horizontal parallel 50 KN forces at the free end (see Figure 5.7) with the same directions, one at the top flange and the other one at the bottom flange inducing lateral deflection and weak axis rotation along the beam.

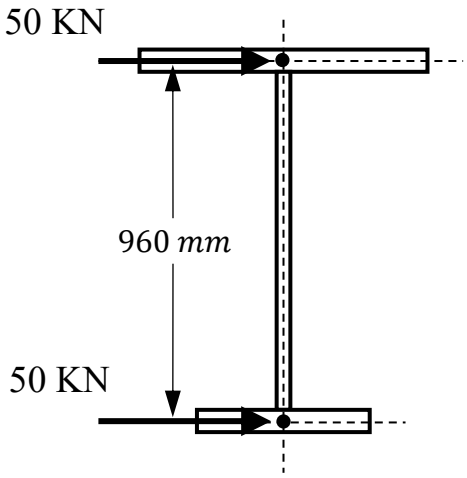

Figure 5.7 Horizontal parallel forces on top and bottom flanges

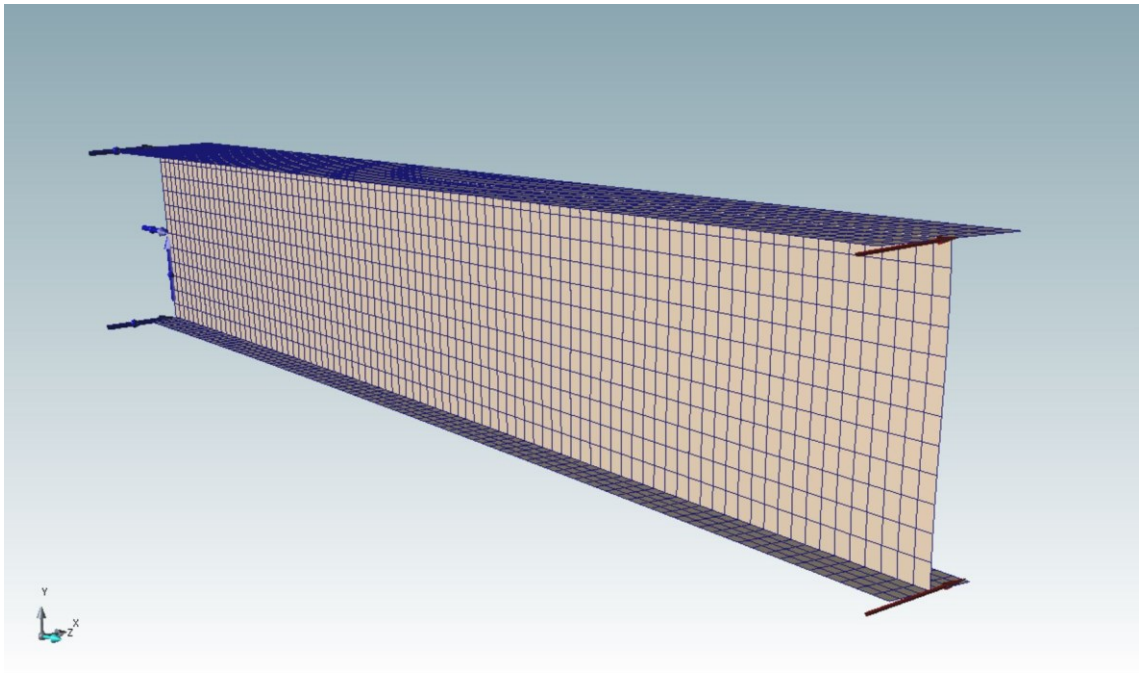

Figure 5.8 Finite element modelling of the cantilever beam subjected to horizontal parallel forces

For bending about the weak axis, the lateral displacements which measured at the middle of the web based on the present theory whether consider distortion and shear or not are in a good agreement with those predicted by the Shell model. The predicted response at the tip is based on the present theory and it is capturing distortional effects. The lateral deflection at the top flange 95.5 mm and while the shell response is 89.84 mm corresponding to 6.3% difference. Also, the predicted respond under the present theory without considering distortion and shear effects is 81 mm while thin-walled response is 81 mm showing greatly matched.

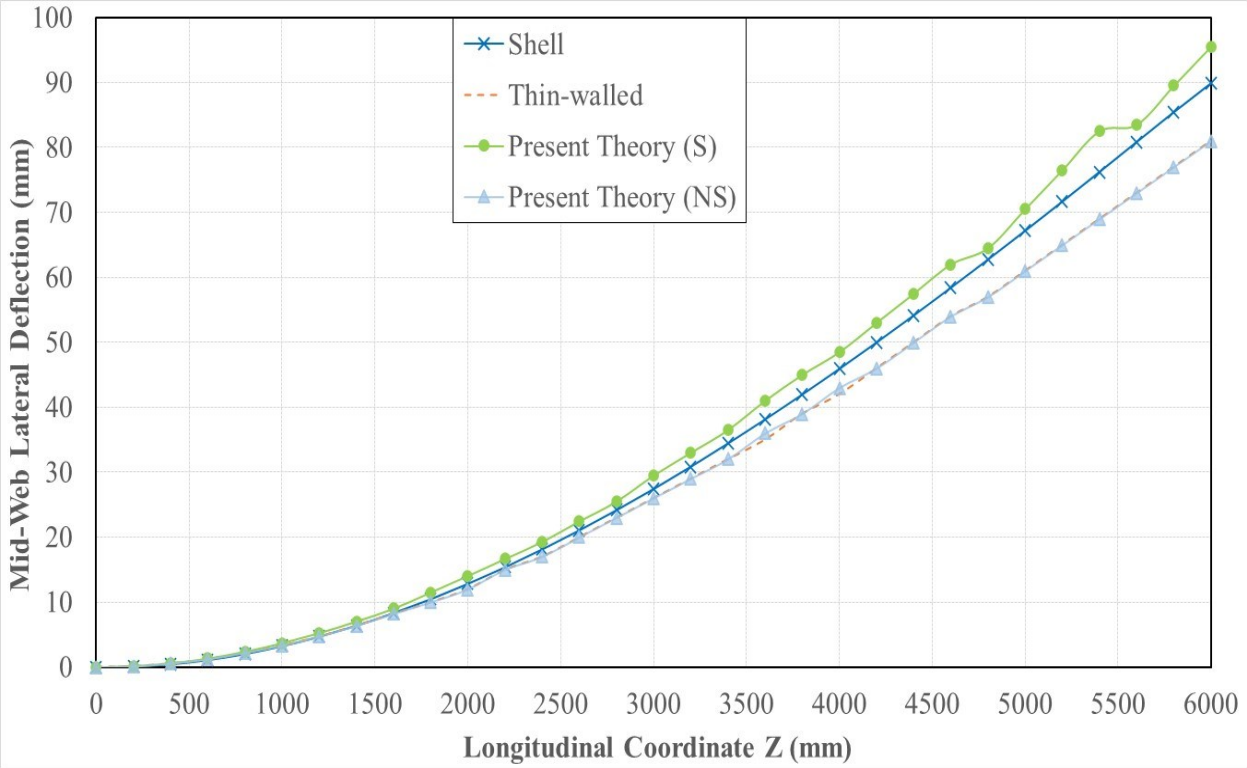

Figure 5.9 Lateral deflection for horizontally loaded cantilever

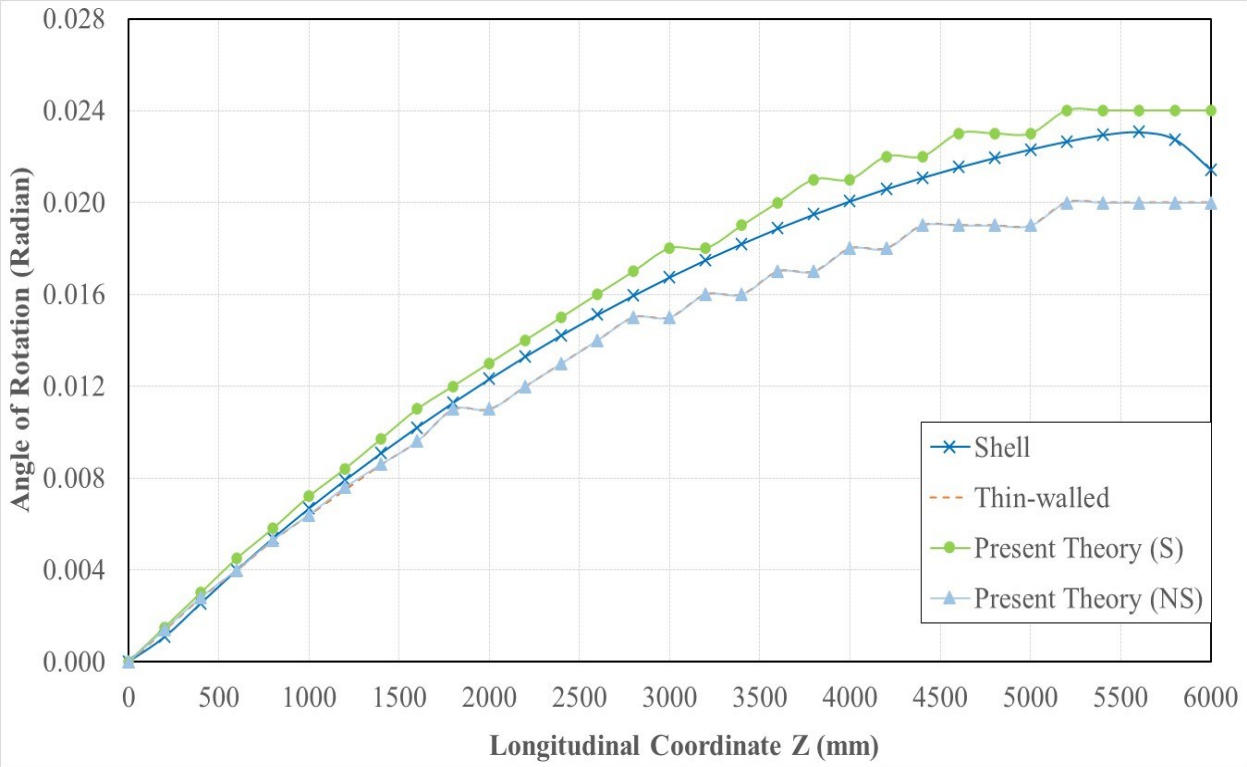

Figure 5.10 Angle of rotation due to weak axis bending of the cantilever beam

Moreover, for another assessment of the present solution the angle of rotation due to weak axis bending of the beam verified against other solution. The angle of rotation at the tip according to the present theory with distortion and shear effect is 2.4×10^{-2} radian while the corresponding response predicted by Shell is 2.1428×10^{-2} comparable to 12% difference. Also, the weak axis angle of rotation based on the present theory without distortion is perfectly match with the thin-walled response as illustrated in Figure 5.10.

5.2.3 Example 3: Cantilever beam under torsion

A 4.00 m span cantilever with mono-symmetric WRF1000×340 steel cross-section is subjected to two horizontal parallel 20 KN forces at the tip (see Figure 5.11) in the opposite directions, one at the top flange and the other one at the bottom flange inducing a 19.2 KN-m twisting moment at tip of the cantilever beam. It is required to check the angle of twist and lateral displacement of each flange under present theory with shell finite element and thin-walled beam solutions.

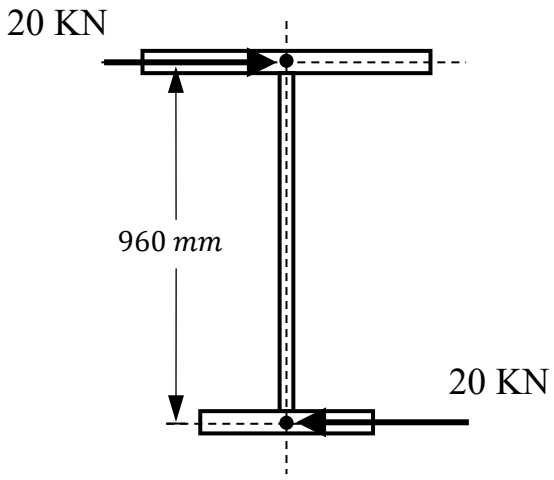

Figure 5.11 Applied twisting moment 19.2 KN-m

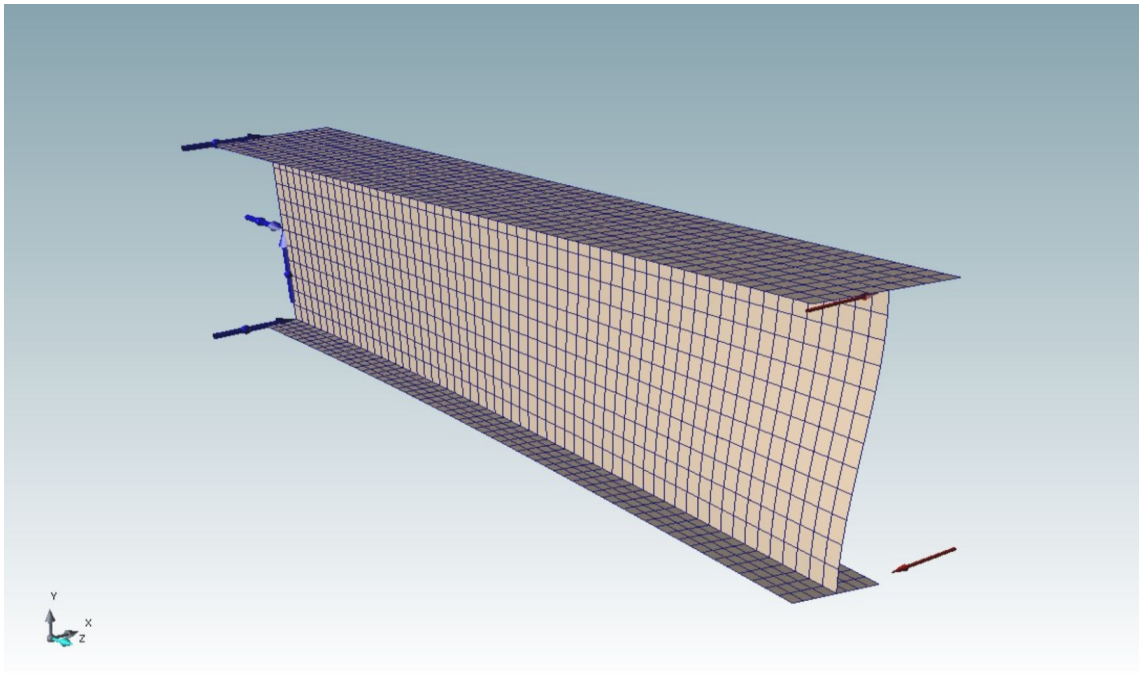

Figure 5.12 Finite element modelling of the cantilever beam under twisting moment

For the shell FEA and present theory solution which capture distortion, the angle of twist is not the same for the entire section. Hence, it is more appropriate to define web average angle of twist as $\theta_w = \frac{U_T - U_B}{h}$ where U_T and U_B are lateral displacements of top and bottom flanges respectively and h is distance between the flanges centerlines. The predicted angles of twist base on the present theory are very close to those predicted by the Shell FEA model. For a span of 4.00 m, for the web average angle of twist at the tip of the cantilever beam there is only 1.59% difference between the present theory and Shell model. Furthermore, by considering distortional effect, very good agreements between the angle of twist of top flanges of present theory and Shell model also the bottom flanges of the present theory and the Shell model can be observed in Figure 5.13.

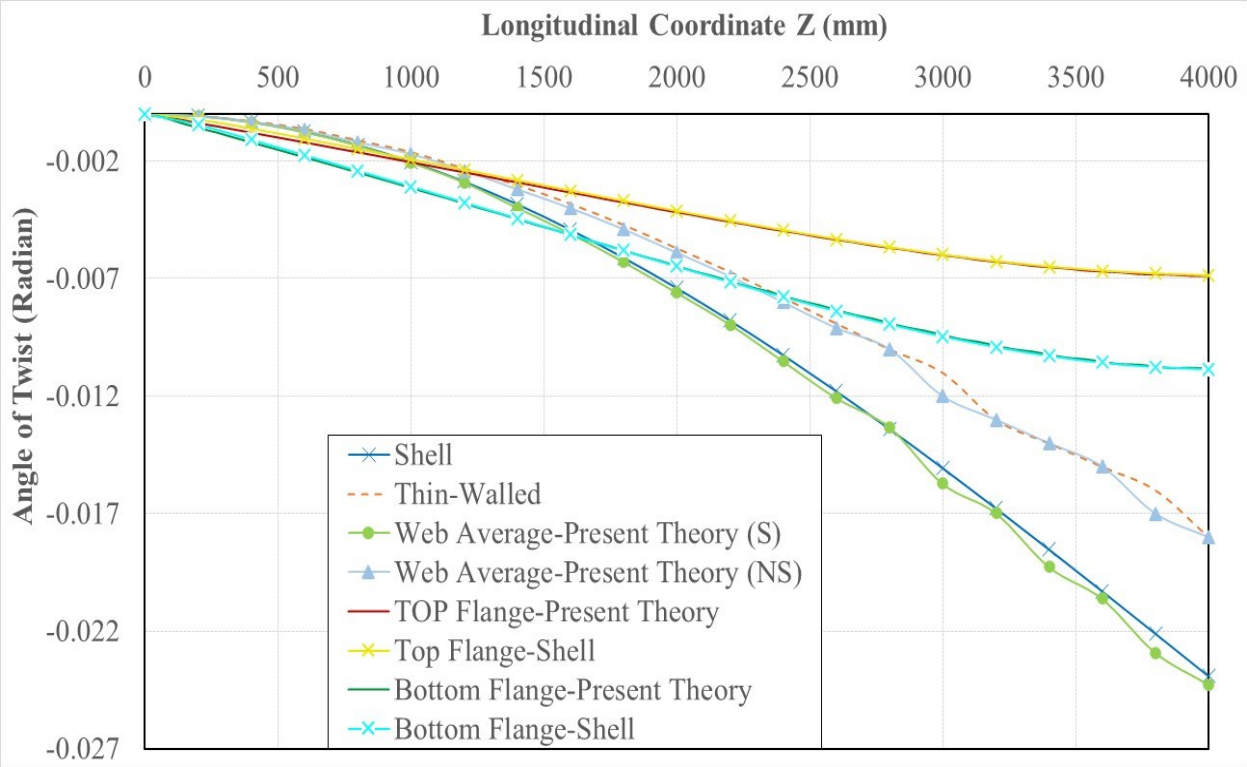

Figure 5.13 Angle of twist along the cantilever beam due to applied twisting moment

Table 5-2. Angle of twist of the free end at the mid-surface of the 4.00m span cantilever

Type of Solution	Angle of Twist (Radian)	Percentage difference relative to Shell FE solution
Shell FE	-0.02392	0%
Thin-walled Beam	-0.018	-24.75%
Present Theory (D+S)	-0.0243	1.59%

5.2.4 Example 4: Cantilever beam with restrained top flange

A 3.00 m span steel composite cantilever beam with the similar cross-section as previous examples is fully restrained by a lateral-torsional support at top flange. The continues restrained beam is subjected to a concentrated lateral force 40 KN at the bottom flange of cantilever tip Figure 5.14. The lateral deflection and longitudinal rotation are totally fixed for the top flange along the whole span ($U_T(z) = 0,\ \theta_T(z) = 0$).

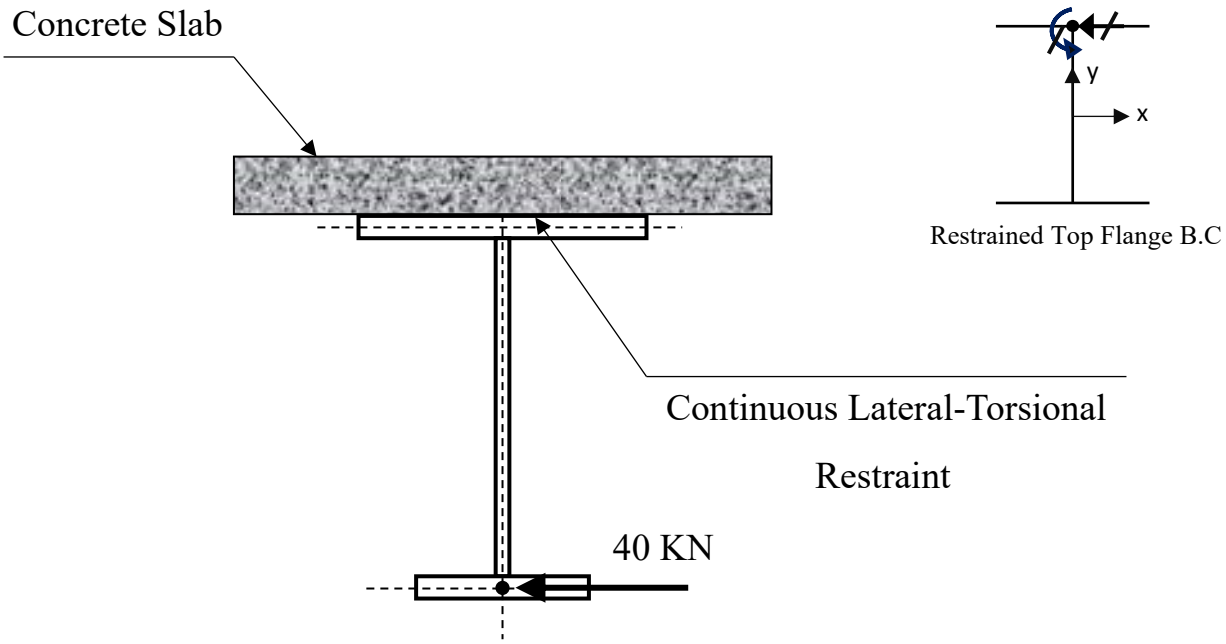

Figure 5.14 cantilever beam with restrained top flange under laterally applied load and related B.C

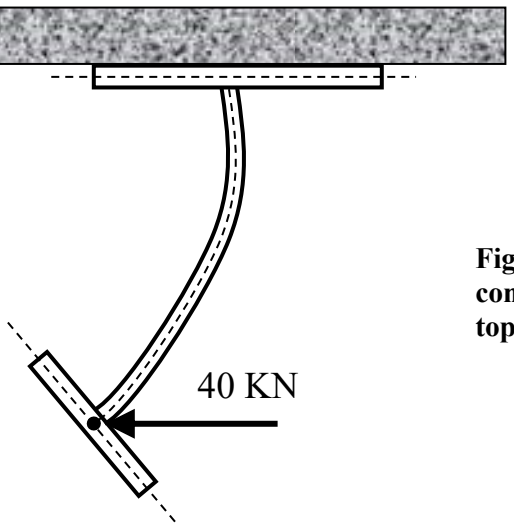

Figure 5.15 Cross-section deformed configuration at the tip with restrained top flange

Figure 5.15 represents the shape of the cross-section at the tip of the cantilever after deformation due to lateral applied load base on the present theory and the Shell model which captures the distortion of the web while it is worthwhile to note that under the thin-walled beam theory and Vlasov theory which do not capture distortional effect and the angle of twist for the entire section is the same, in this example which the top flange is totally fixed for the whole span the lateral displacement for the bottom flange and the angle of twist will be yield to zero.

The lateral displacements of the bottom flange are shown in Figure 5.16 where an excellent agreement can be observed between the present theory solution and the Shell model. The lateral displacement of the bottom flange at the tip base on the present theory is 19 mm while for the Shell is 18.295 mm corresponding to a 3.85% difference.

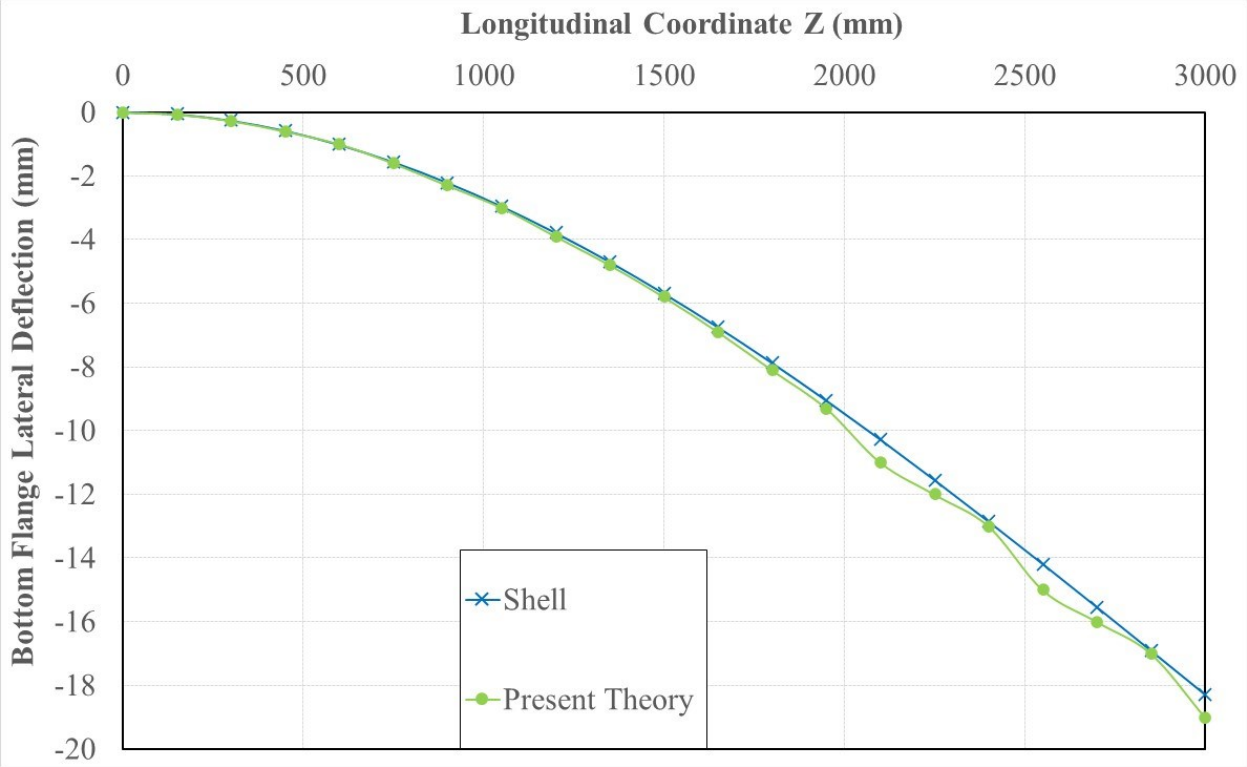

Figure 5.16 Bottom flange lateral deflection along the cantilever beam

6. Chapter 6: Validation of the Developed Distortional Beam Formulation (DBF), Buckling Response Predictions

The material is assumed steel and therefore the modulus of elasticity and Poisson ratio are taken as E=200GPa and v=0.3, respectively. A general description of thin-walled cross-sections, and boundary and loading conditions is given in Figure 6.1. For each section along the span, the SEF requires meshing of the cross-section. On the other hand, the DBF requires meshing only along the beam span. Degrees-of-freedoms of DBE and their locations on the cross-section were previously described in Figure 4.1. For numerical integration of DBF 4-point Gauss integration along the element span, 8-point Gauss integration along the contour direction and 20-point trapezoidal rule across the thickness were used. For numerical integration of SEF, 2x2 Gauss integration scheme is used as suggested in [30,31]. Shell formulations similar to SEF that were formed by combining plate and membrane elements and used for buckling analysis of thin-walled beam structures can be found in [32-34].

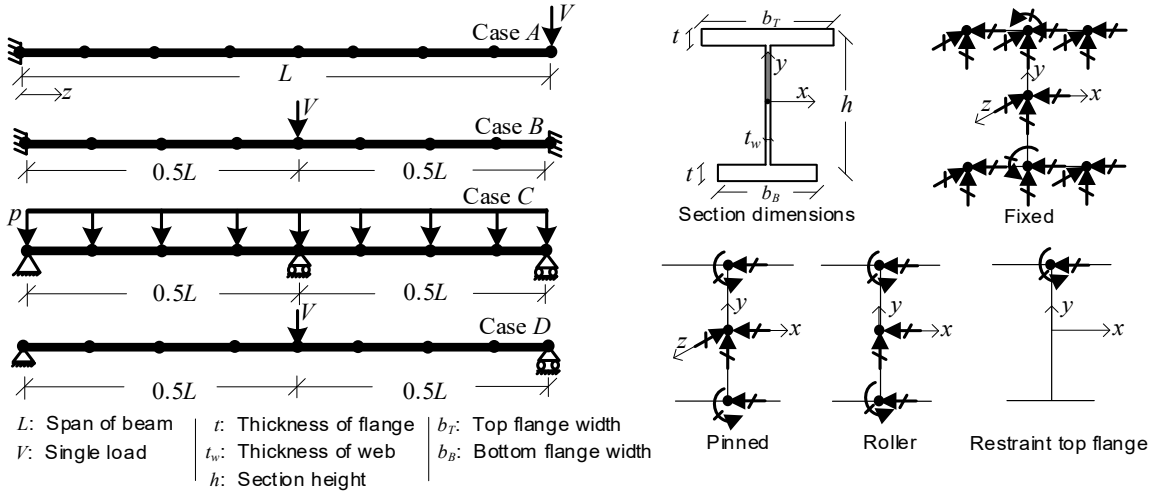

Figure 6.1 Description of loading and boundary conditions of the analysed four cases – see ref [37]

For the case studies various types of analysis options are employed including the developed Distortional Beam Formulation (DBF), the rigid web thin-walled beam formulation as a special case (TBF); and a Shell Element Formulation (SEF) formed by combining plate and membrane elements whose details are already explained in section 5.1. Various analysis options that can be

adopted using DBF have also been tested which includes the selection of the second order e_{yy} strains effects by exclusion $\mu=0$ or inclusion $\mu=1$.

For each case, we present the critical first mode buckling load predictions and the corresponding mode shapes against the number of elements as well as the first mode lateral deflections and twist angles in the middle of top and bottom flanges. 3D deformed shapes for the first buckling load are also presented in each case.

6.1. Case A: Cantilever beam

We first analyse a series of cantilever beams whose span are ranging between 2m to 8m. The reason of selection short beam is to amplify distortion effect, on the other hand even though the 8m cantilever may not be very practical by selecting such a long beam we would like to avoid the error in distortional behaviour and show the agreement with the shell model. A vertical load is applied at the tip of the cantilever and a W310x39 section (class 2) is used for which the cross-sectional dimensions are b_T=b_B=165mm, h=300.3mm, t=9.7mm and t_w=5.8mm (see Figure 6.1). We use 150 and 600 element SEF models. In 150 element model, the cross-section is divided into 6 elements by using two elements for the web and two elements for each flange, and the span is divided into 25 elements. In 600 element SEF model, the cross-section is divided into 12 elements by using four elements for the web and four elements for each flange, and the span is divided into 50 elements. It should be noted that in the SEF-based analysis, in order to prevent local buckling due to local stress concentration at the tip where the load is applied, MPCs were imposed to keep the web rigid in vertical direction only at the free end.

In Pezeshky and Mohareb [19] a similar beam formulation that also captures distortional buckling has been developed in which the effects of pre-buckling deformations on the buckling predictions were optionally considered. Our 2m cantilever beam case is identical to one of the cases presented in Pezeshky and Mohareb [19] and we compare our results with that based on no-pre-buckling deformation effect which was designated as MD in their paper. They have used Euler-Rodrigues rotation angles in their formulation. It is interesting to note that their formulation uses second order e_{yy} strains along the web direction which will be shown to be overly conservative in some cases especially due to the fact that the pre-buckling stress analysis does not include web extensibility related degrees-of-freedoms, and therefore can only determine σ_{yy} stress due to Poisson ratio

effect on a constraint web. Comparison to the developed formulation herein, Pezeshky and Mohareb [19] have also included axial strains induced by local (Gjelsvik) warping in their analysis, which we intentionally eliminated as discussed in Section 2.5. Their interpolation scheme for the lateral displacement field is based on cubic shape functions along the web in *y* direction and up to quintic interpolation along the span in *z* direction resulting with nodal curvatures included within the active degrees-of-freedom. For comparison purposed, by using a matrix notation similar to Chapter 4, their interpolation of the lateral displacement field can be described as $u(y,z)=H_1\mathbf{Q}\tilde{\mathbf{\Lambda}}_B+H_2\mathbf{L}\mathbf{\Gamma}_B+H_3\mathbf{Q}\tilde{\mathbf{\Lambda}}_T+H_4\mathbf{L}\mathbf{\Gamma}_T$, in which $\tilde{\mathbf{\Lambda}}_B=\left\langle u_{B1} \quad \phi_{yB1} \quad u''_{B1} \quad u_{B2} \quad \phi_{yB2} \quad u''_{B2}\right\rangle^{\mathrm{T}}$ and $\tilde{\mathbf{\Lambda}}_T=\left\langle u_{T1} \quad \phi_{yT1} \quad u''_{T1} \quad u_{T2} \quad \phi_{yT2} \quad u''_{T2}\right\rangle^{\mathrm{T}}$ differs from our vectors $\mathbf{\Lambda}_B=\left\langle u_{B1} \quad \phi_{yB1} \quad u_{B2} \quad \phi_{yB2}\right\rangle^{\mathrm{T}}$, $\mathbf{\Lambda}_T=\left\langle u_{T1} \quad \phi_{yT1} \quad u_{T2} \quad \phi_{yT2}\right\rangle^{\mathrm{T}}$ used in equation 4.1 due to their addition of nodal curvatures, and $\mathbf{Q}$ is a vector of Quintic functions, i.e.

$$Q_1=1-\frac{10z^3}{L^3}+\frac{15z^4}{L^4}-\frac{6z^5}{L^5} \qquad Q_2=z-\frac{6z^3}{L^2}+\frac{8z^4}{L^3}-\frac{3z^5}{L^4} \qquad Q_3=\frac{z^2}{2}-\frac{3z^3}{2L}+\frac{3z^4}{2L^2}-\frac{z^5}{2L^3} \qquad 6.1$$

$$Q_4=\frac{10z^3}{L^3}-\frac{15z^4}{L^4}+\frac{6z^5}{L^5} \qquad Q_5=-\frac{4z^3}{L^2}+\frac{7z^4}{L^3}-\frac{3z^5}{L^4} \qquad Q_3=\frac{3z^3}{2L}-\frac{z^4}{L^2}+\frac{z^5}{2L^3}$$

All possible analysis options developed herein were considered and results were obtained for 2, 4, 8, 16, 32 and 64 element models when beam formulations are used. Alternatively, 150 and 600 element SEF solutions are also presented in the same graph. In addition, Figure 6.2 contains the results from Pezeshky and Mohareb [19] for which the authors used 2,3,4,5, 15, 25 and 35 element solutions.

Figure 6.2 shows that compared to the DBF solutions TBF formulation always overestimates the buckling load due to rigid web assumption. However, considering that the cantilever is short and therefore, it is prone to distortional buckling TBF formulation is not reliable for this case. Indeed, the first mode shapes of SEF as shown in Figure 6.11 and Figure 6.12 confirms that web is bending involved in the buckling behavior. The effect of rotation angle on Lateral buckling predictions of cantilevers has been an issue of debates as discussed in detail in [27]. Distortional beam formulation of Pezeshky and Mohareb [19], agrees well with the SEF results.

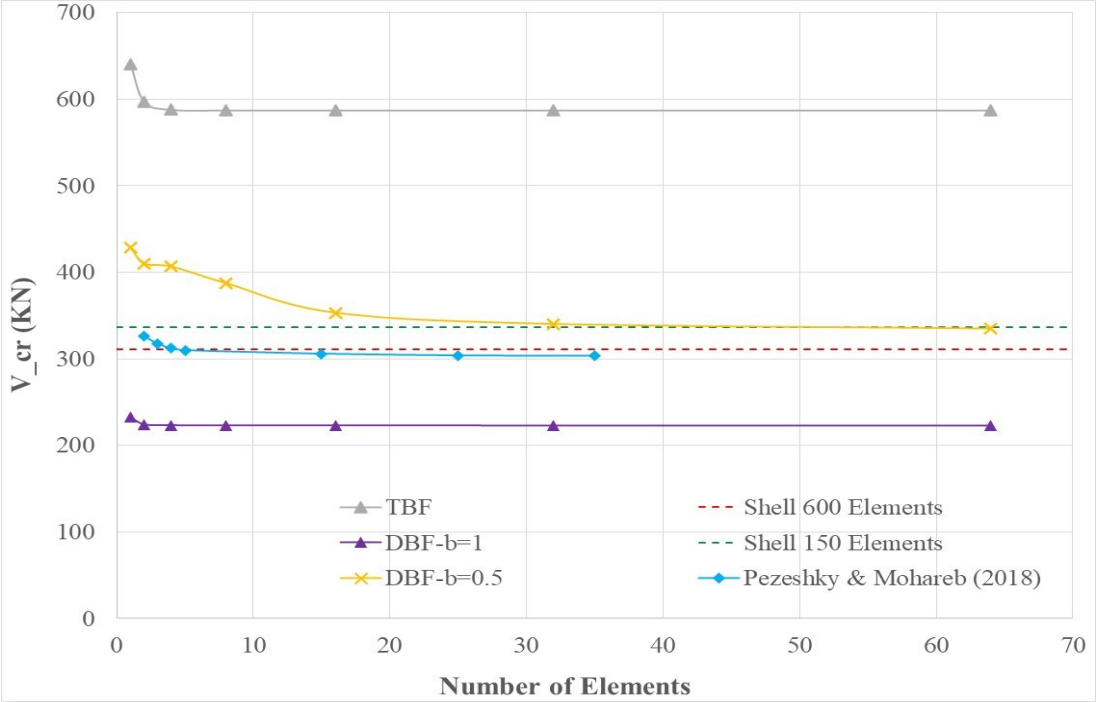

Figure 6.2 Critical tip load for the L=2m cantilever beam

It is interesting to note that when the second order strains e_{yy} in equation 2.18 of DBF is included, the buckling load decreases significantly as shown in Figure 6.3. That is because interaction of compressive stresses along the web contour σ_{yy} with e_{yy} cause early buckling. In DBF, there is no degrees-of-freedom capturing web expansion or contraction, and therefore the only reason for σ_{yy} to occur in pre-buckling analysis is the Poisson ratio effects, i.e. $\sigma_{yy}= E\upsilon\varepsilon_{zz}/\left(1-\upsilon^2\right)$ (see equation 3.1) under non-extensible web assumption). As Figure 6.3 shows, this approach may lead to overly conservative results. There is around 43% drop in the predicted buckling load when e_{yy} is included in the DBF-based solution. Unless sufficient degrees of freedoms are defined to capture web extension or contraction, it is not possible to generate accurate pre-buckling stresses in y direction σ_{yy} . This requires separate DOFS in vertical directions at the top and bottom flanges which is not included in the current formulation. Therefore, for consistency in the analysis, it is suggested that DBF should be used after removing e_{yy} from the equations, i.e. $\mu = 0$ to avoid overly conservative predictions. However, it should be noted that the current formulation may not be accurate when there is significant pressure along the vertical direction within the web.

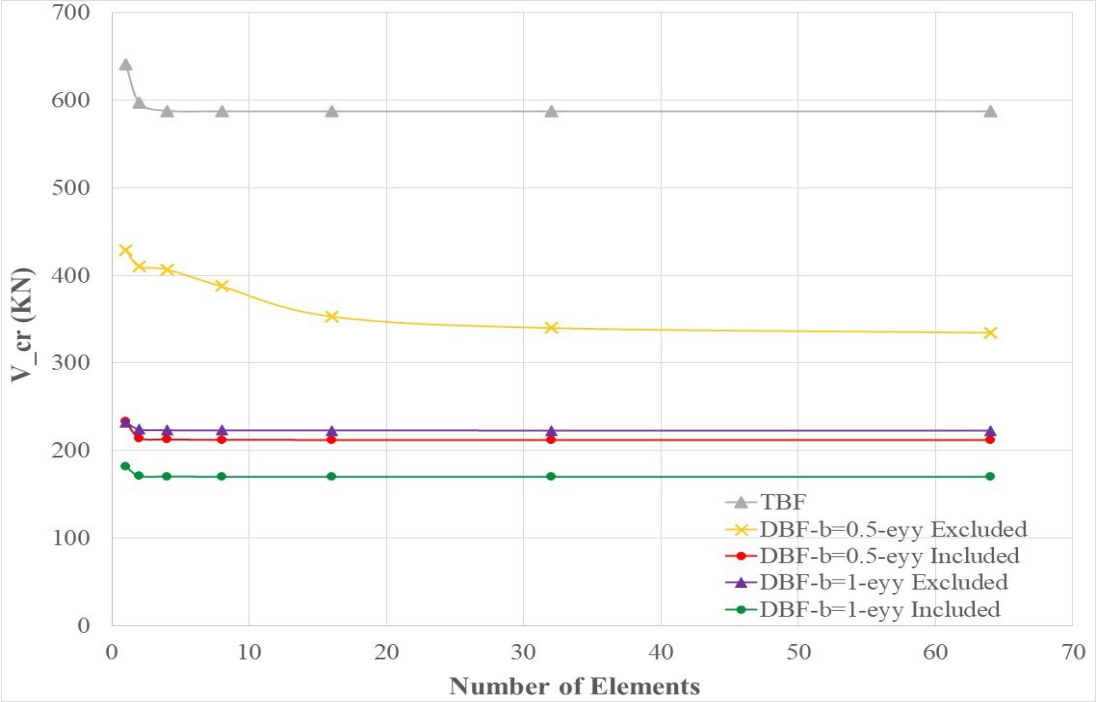

Figure 6.3 Effect of second order vertical strain on buckling load predictions for the L=2m cantilever Beam

A similar observation can be made when the beam span is increased twice to L=4m. The problem is otherwise identical, i.e., a vertical load is applied at the tip of the beam and a W310x39 section was used for which the cross-sectional dimensions are b=165mm, h=300.3mm, t=9.7mm and t_w=5.8mm (see Figure 6.1). The linearized buckling analysis results for this case are shown in Figure 6.4. Comparison to the L=2m cantilever case, when the span is increased the distortional effects are reduced which can be verified by the fact that TBF and DBF results becomes much closer. However, as shown in, the drop in the predicted buckling load due to inclusion of e_{yy} has increased to 46%. Thus, even though the distortional effects are reduced, the drop in the buckling load due to e_{yy} term is quite significant.

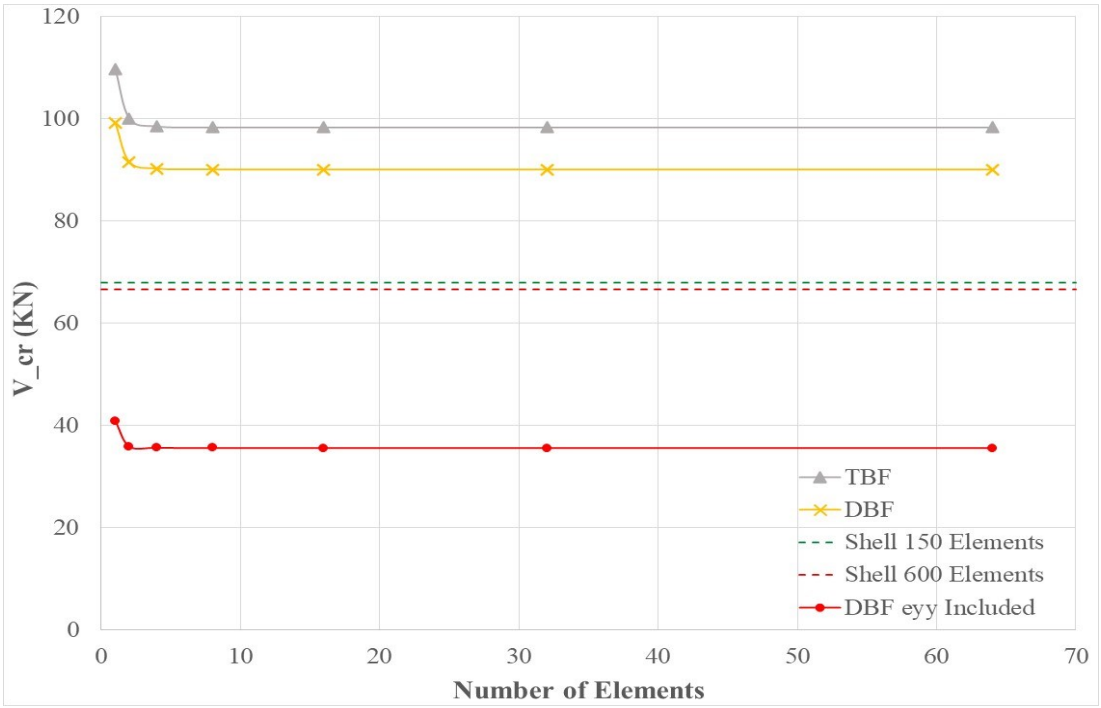

Figure 6.4 Critical tip load for the L=4m cantilever beam

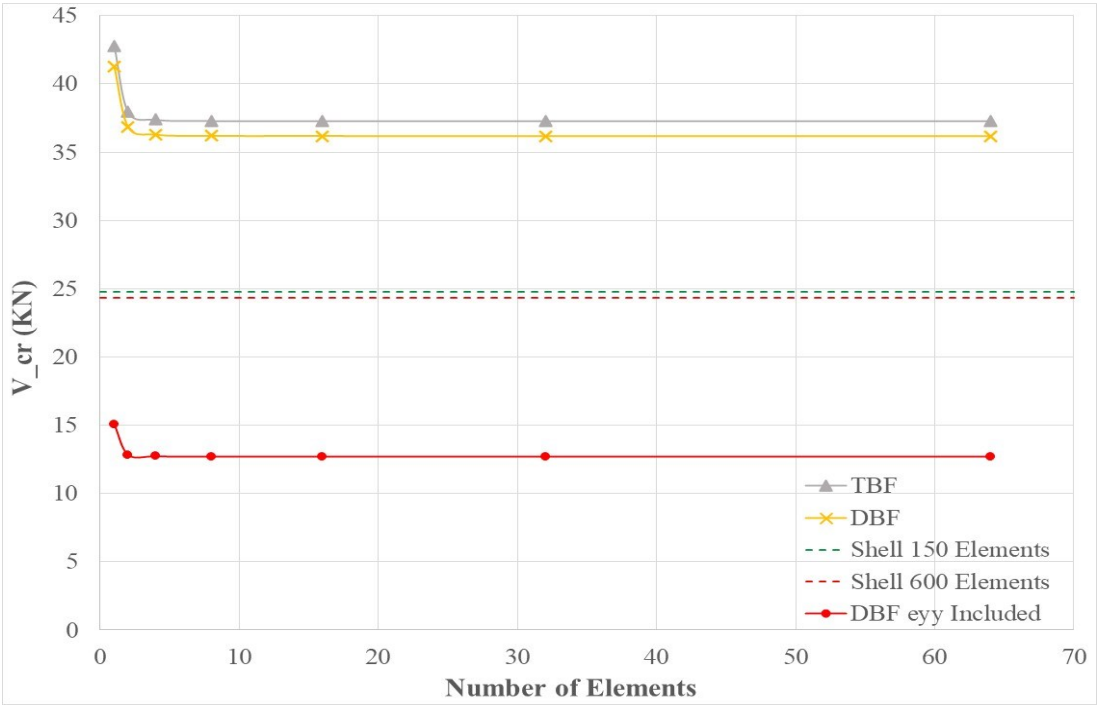

Figure 6.5 Critical tip load for the L=6m cantilever beam

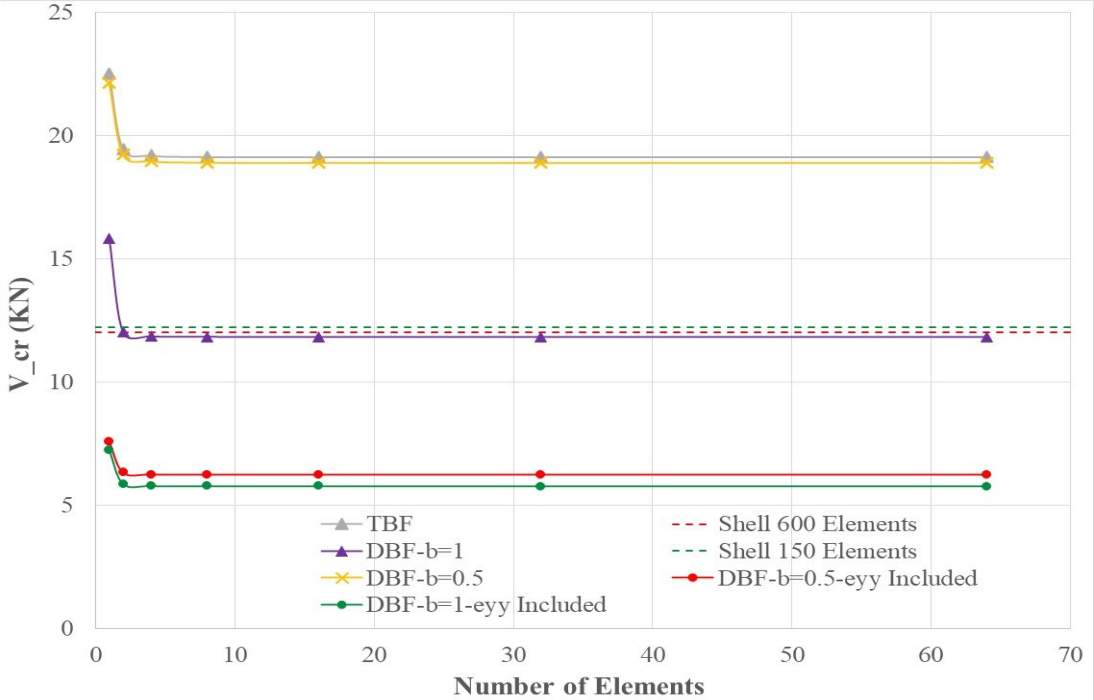

Figure 6.6 Critical tip load for the L=8m cantilever beam

It can be verified from Figure 6.2, Figure 6.3, Figure 6.4, Figure 6.5, and Figure 6.6 that the difference between the DBF and TBF formulations tend to decrease as the beam span increases. However, when m=1, DBF results significantly drop and underestimates buckling load comparison to SEF. Therefore, it is the authors opinion to DBF is not reliable as the span increases due to the fact that σ_{yy} effect on the first mode buckling load should diminish.

Figure 6.7 shows the lateral deflections of the top and bottom flanges based on the first mode shape. For comparison purposes the amplitudes of the top flange in DBF formulation was forced to match with that of the SEF formulation. For that purpose, a proportionality factor was identified and all other deflections including the angle of twist was multiplied with the same factor. However, in drawing 3D shapes in Figure 6.15, the intention is to qualitatively inspect the modes, i.e., whether there is web bending, lateral buckling or the DBF shapes agree with SEF etc., and therefore amplitudes were not adjusted. Only 2m and 8m results are shown for the buckling mode shapes. Results of the 16 element and 600 element analyses were used for DBF and SEF mode shapes respectively. Also note that the graphical tool used for the 3D Figs is such that, the grids in

Figure 6.15e-f indicate the number of elements for the SEF results, while grids are only related to the number of integration points in Figure 6.15a-b-c-d for the DBF results.

For the 2m beam, it can be verified from Figure 6.7 that DBF lateral deflections agree well with those of SEF. On the other hand, discrepancies can be observed in Figure 6.8 for the angle of twist results between DBF and SEF formulations which is due to the applied Euler-Rodriguez rotation tensor (beta=0.5). However, those discrepancies tend to decrease as the beam span gets longer as can be seen in Figure 6.9 and Figure 6.10, in which case the results of DBF and SEF almost match. It is also interesting to note that the angle of twist results of the top and bottom flange differs significantly when the beam span is short which is due to the fact that the buckling mode is distortional for short beams. As the beam span increases to 8m, the angle of twist for both top and bottom flanges come closer to each other in both DBF and SEF results.

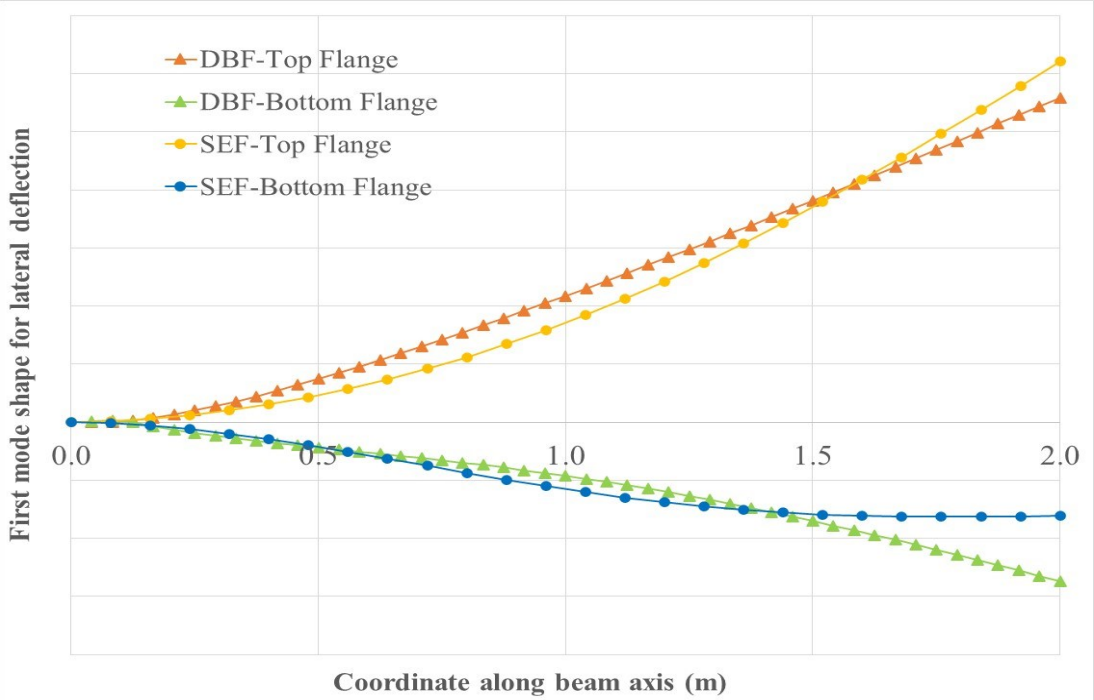

Figure 6.7 First mode shape for L=2m - Top and Bottom flange Lateral Displacement (beta=0.5)

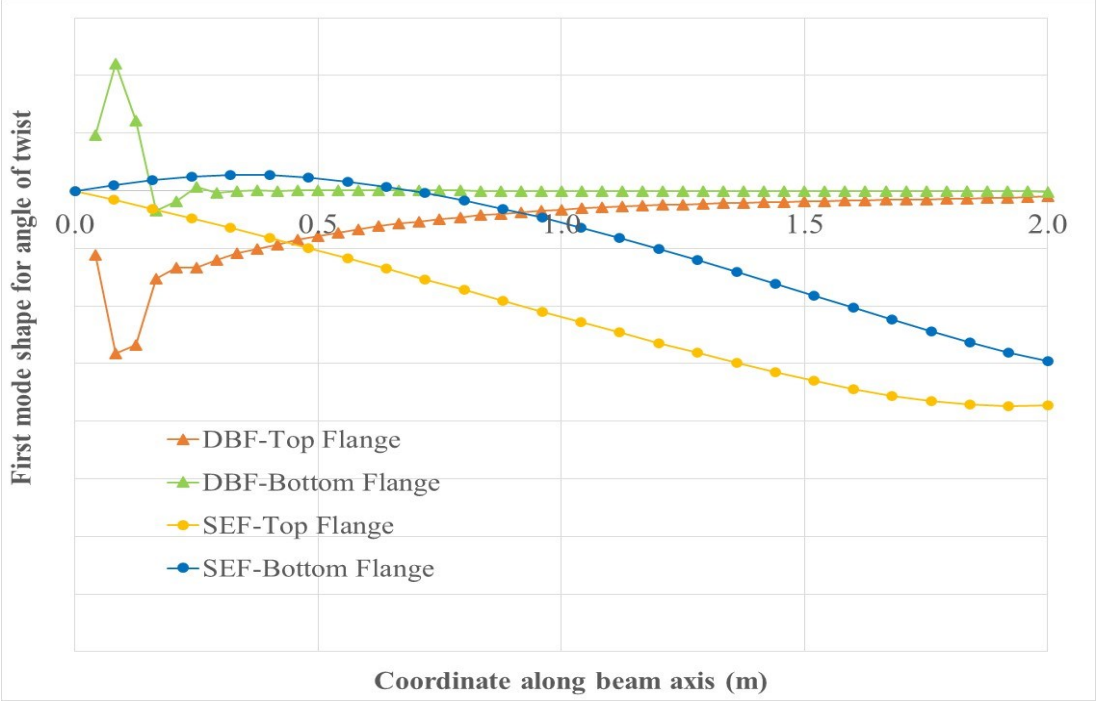

Figure 6.8 First mode shape for L=2m - Top and Bottom flange Angle of Twist (beta=0.5)

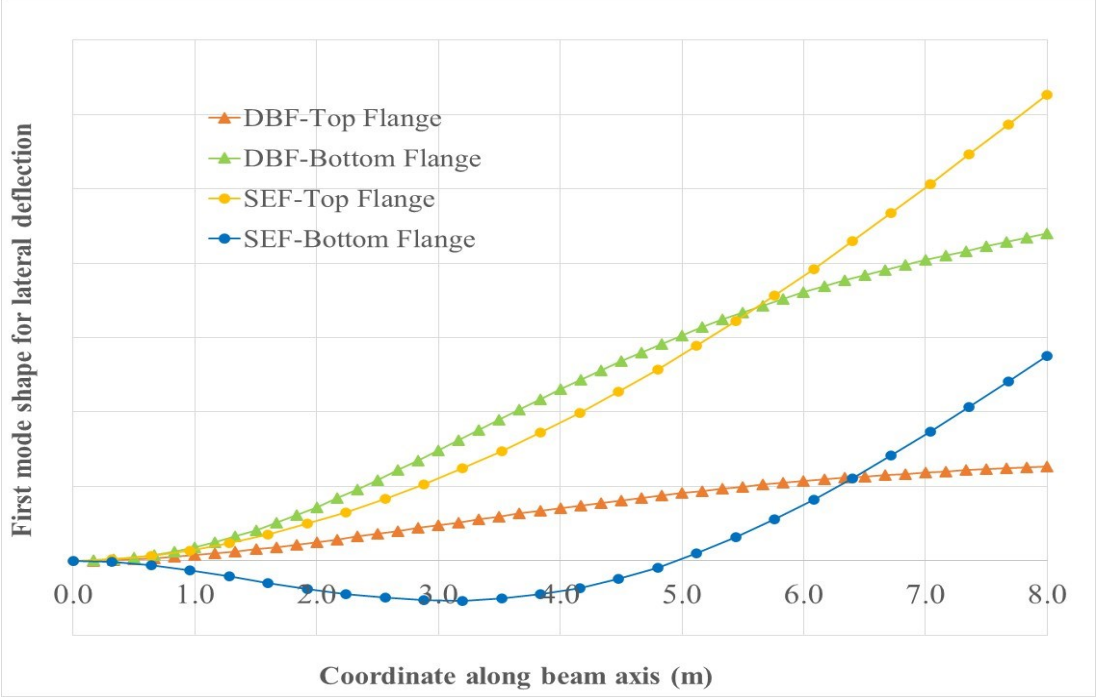

Figure 6.9 First mode shape for L=8m - Top and Bottom flange Lateral Displacement (beta=0.5)

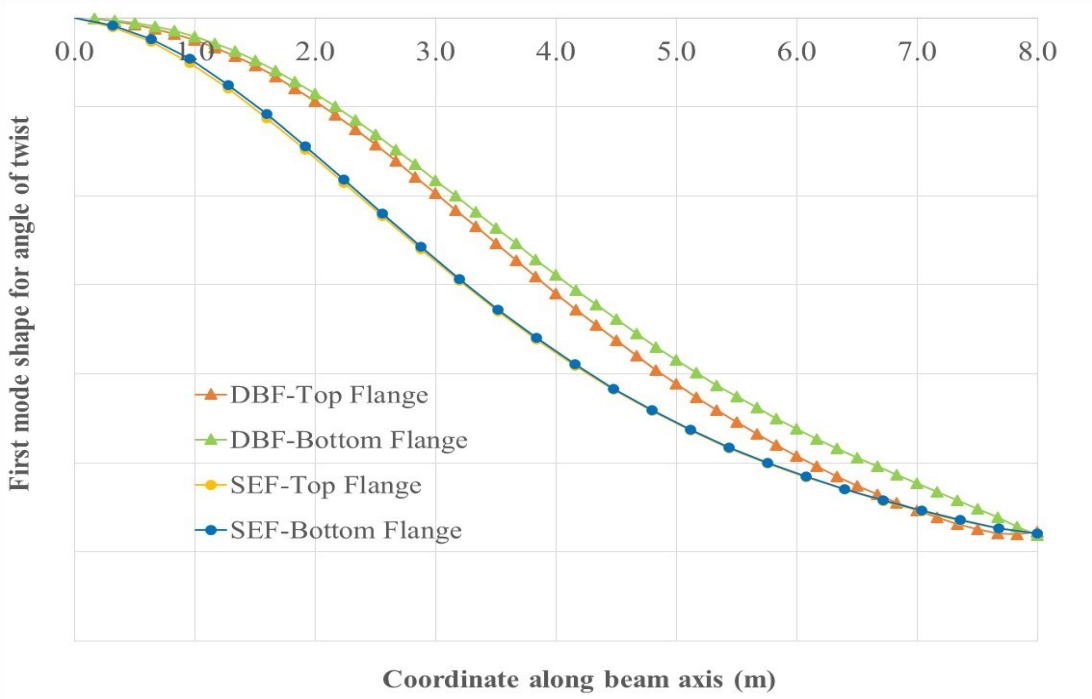

Figure 6.10 First mode shape for L=8m - Top and Bottom flange Angle of Twist (beta=0.5)

It is interesting to note that the mentioned discrepancies for the lateral deflection results between DBF and SEF formulations in 2-meter and 8-meter cantilever beams are due to the selection of rotation angles i.e., we used 0.5 for our results which is based on Euler-Rodrigues rotation tensor, however as long as the rotation angle is changed to 1 which is adopted by Pi et al [27, 37] a good agreement can be observed between DBF and SEF results (see Figure 6.11 to Figure 6.14).

The load application points in Figure 6.15, are shown with red, which is at the middle of the web at the tip of the cantilever. On the other hand, blue arrows show where the restrains are applied at the root of the beam. It can be verified from Figure 6.15b that when the beam span is 2m the buckling mode involves web bending. However, the web is almost straight when the span is increased to 8m as can be seen from Figure 6.15c-d.

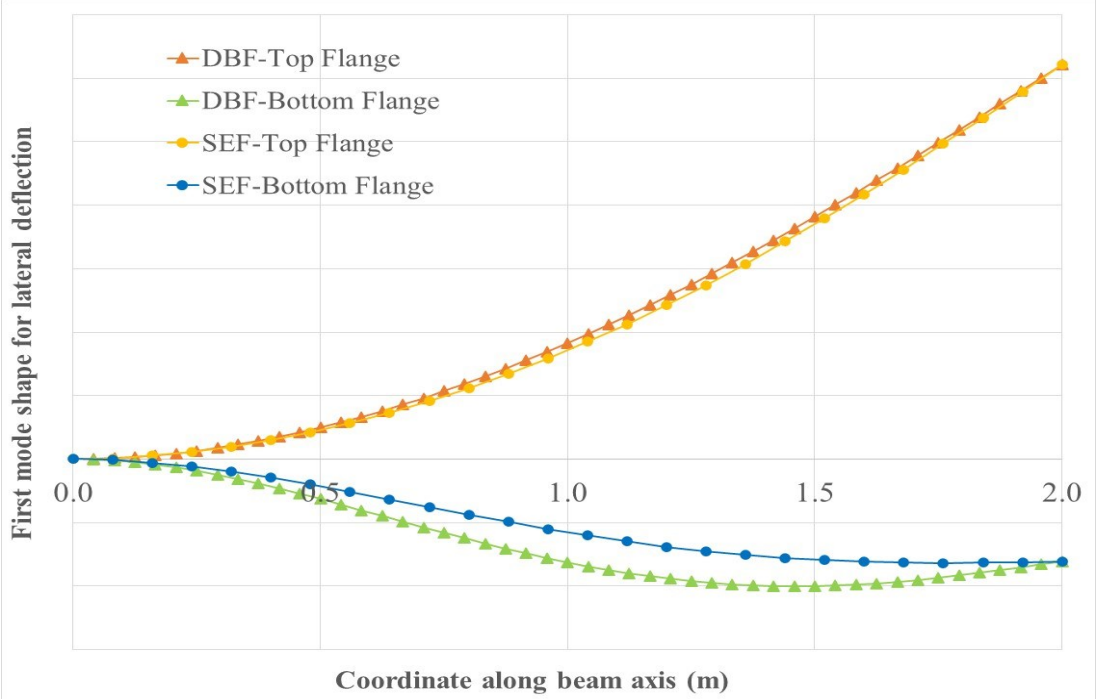

Figure 6.11 First mode shape for L=2m - Top and Bottom flange Lateral Displacement (beta=1)

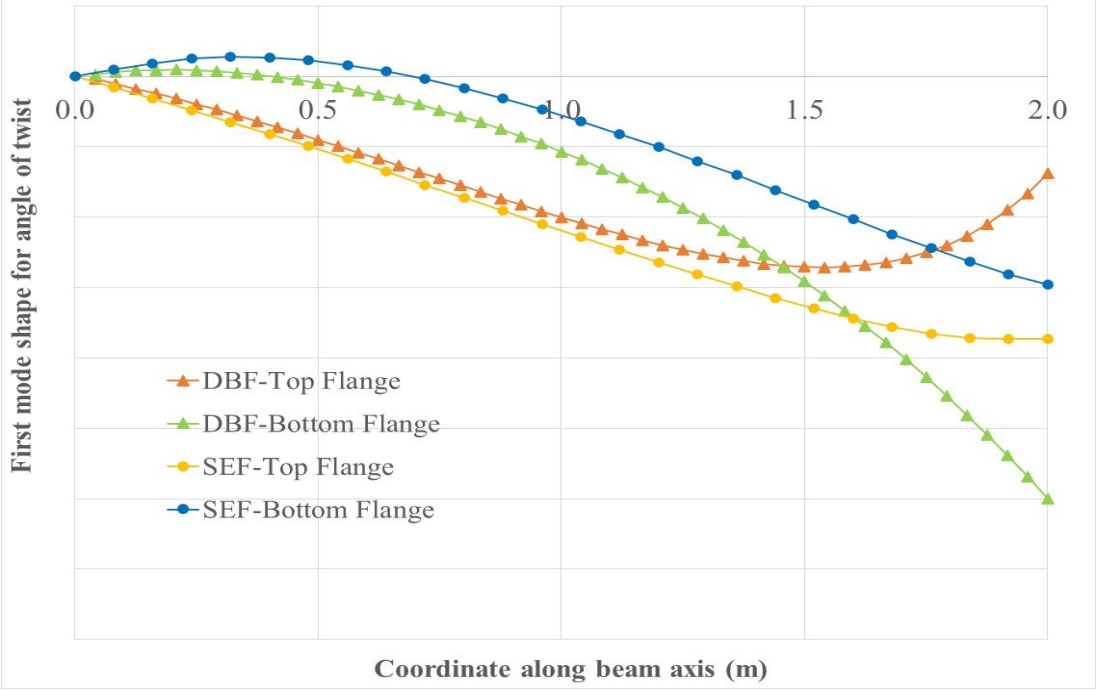

Figure 6.12 First mode shape for L=2m - Top and Bottom flange Angle of Twist (beta=1)

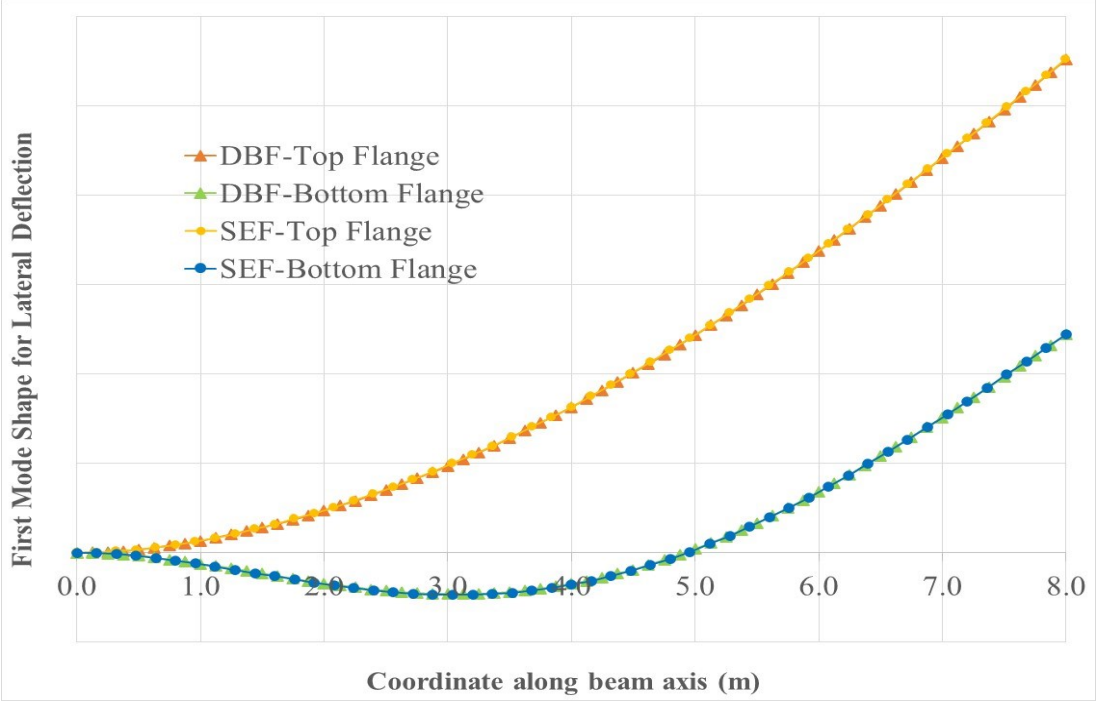

Figure 6.13 First mode shape for L=8m - Top and Bottom flange Lateral Displacement (beta=1)

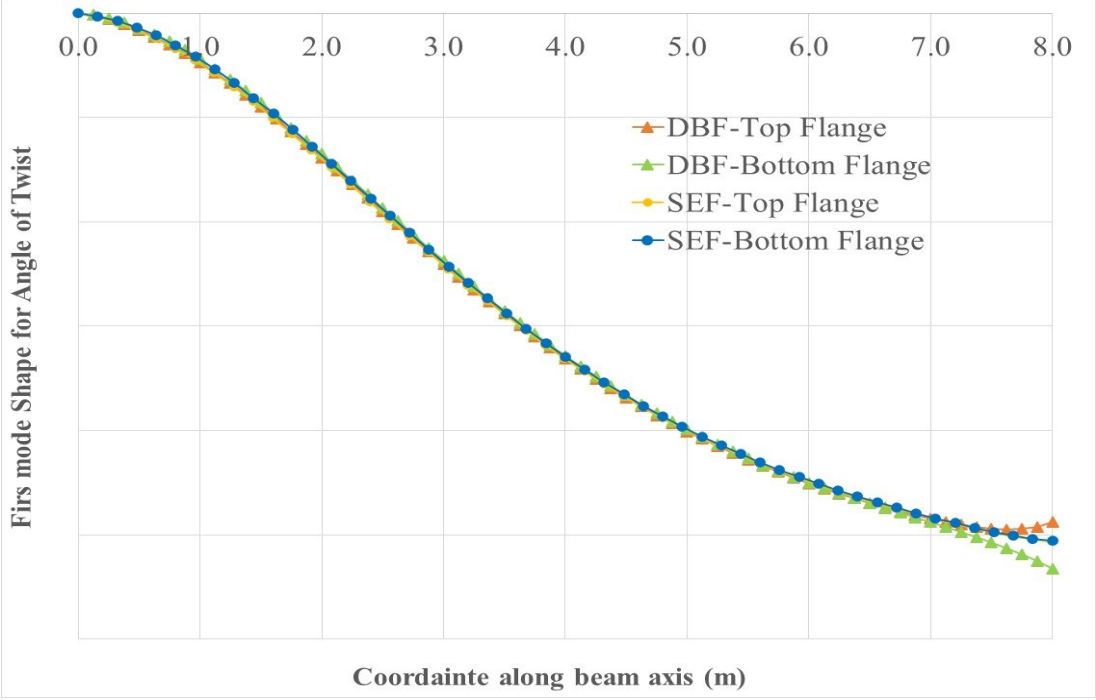

Figure 6.14 First mode shape for L=8m - Top and Bottom flange Angle of Twist (beta=1)

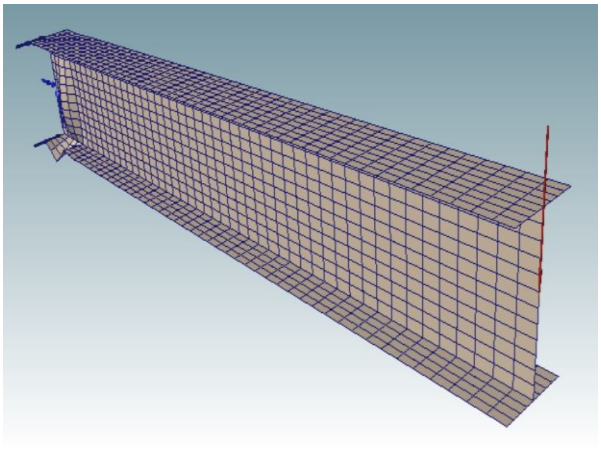

a) DBF for the *L*=2m Cantilever (beta=0.5)

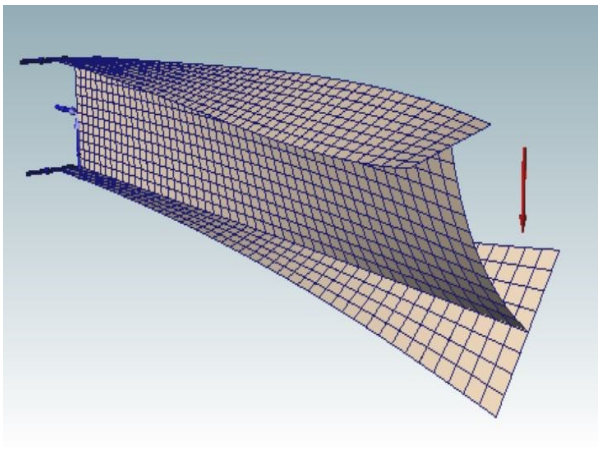

b) DBF for the *L*=2m Cantilever (beta=1)

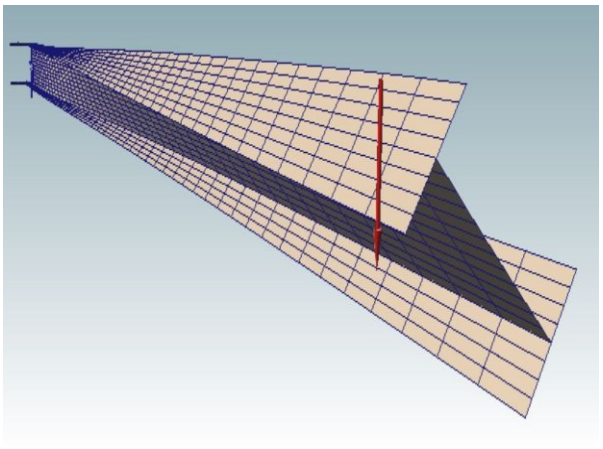

c) DBF for the *L*=8m Cantilever (beta=0.5)

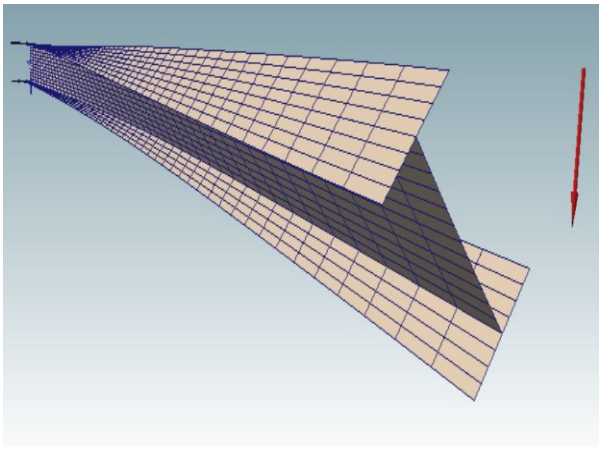

d) DBF for the *L*=8m Cantilever (beta=1)

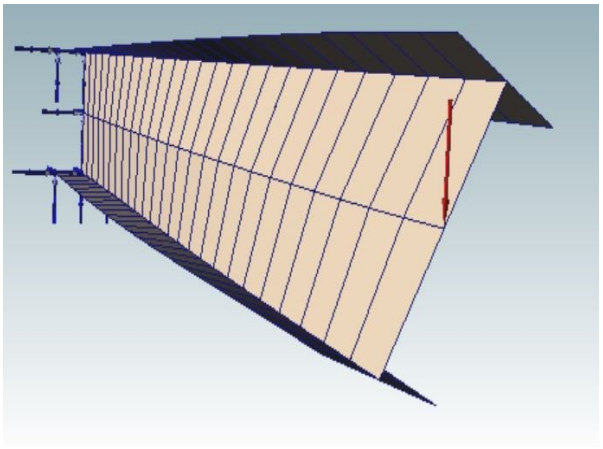

e) SEF for the *L*=2m Cantilever

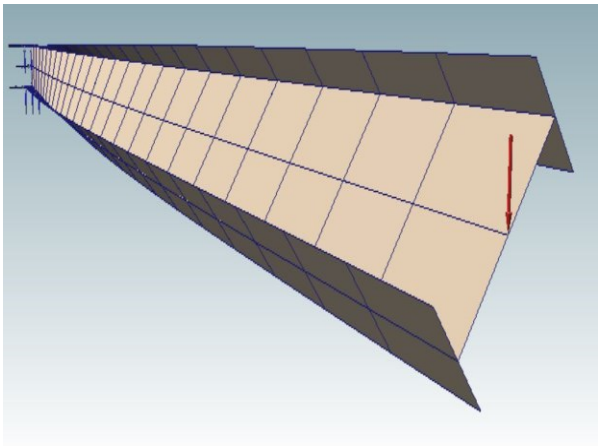

f) SEF for the *L*=8m Cantilever

Figure 6.15 3D Figures for the buckled shapes of the first mode

6.2. Case B: Fixed-fixed beam

Fixed-fixed beams of span 5m and 10m are analyzed using DBF and the results are compared with those of TBF and SEF-based analyses. Vertical load is applied at the mid-span of the beam and a W1000x222 section (class 2) is used for which the cross-sectional dimensions are b_T=b_B=300mm, h=970mm, t=21.1mm and t_w=16mm (see Figure 6.1). In 288-element SEF model, the cross-section is divided into 6 elements by using two elements for the web and two elements for each flange, and the span is divided into 48 elements. In 400 element SEF model, the cross-section is divided into 8 elements by using four elements for the web and two elements for each flanges, and the span is divided into 50 elements. Figure 6.16 shows the critical buckling load predictions of the 5m span beam. Figure 6.17 shows the critical buckling load predictions of the 10m span beam. DBF results are generally in very good agreement with SEF-based results compared to TBF. For the 5m span beam, the web distortion effects in the buckling behavior are significant therefore TBF significantly over-estimates the buckling load and especially. Again, the differences between DBF and TBF formulations reduce as the beam span increases, and all of the analysis are based on the Euler-Rodriguez rotation tensor (beta=0.5).

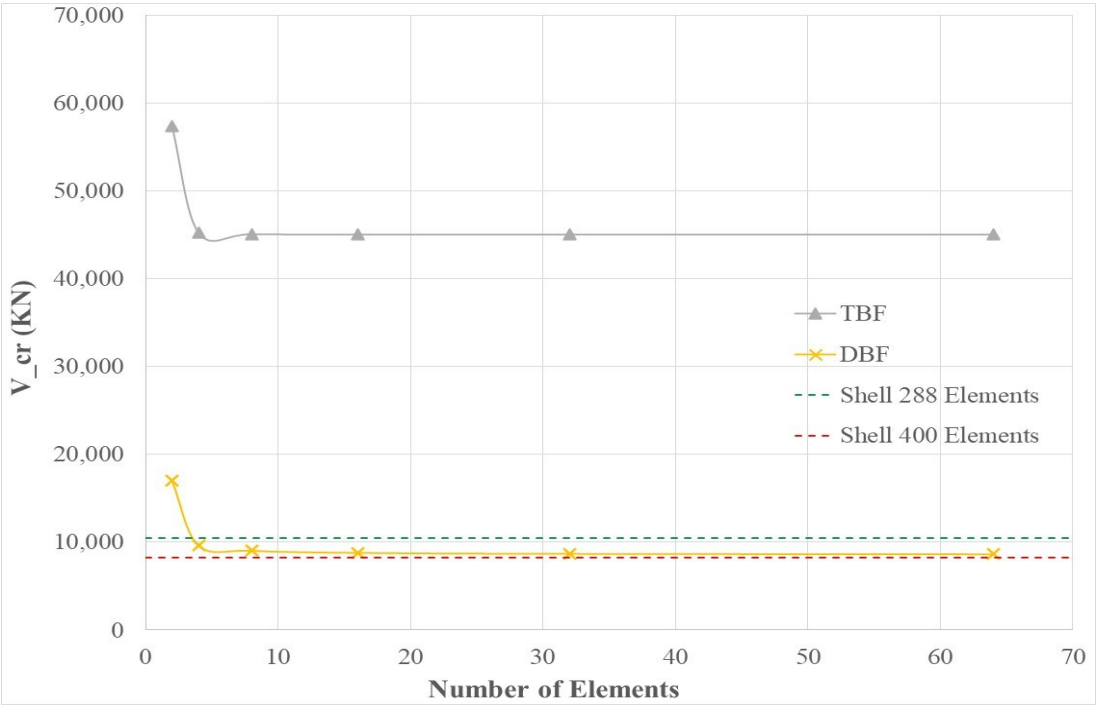

Figure 6.16 Critical mid-span load for the L=5m fixed-fixed beam

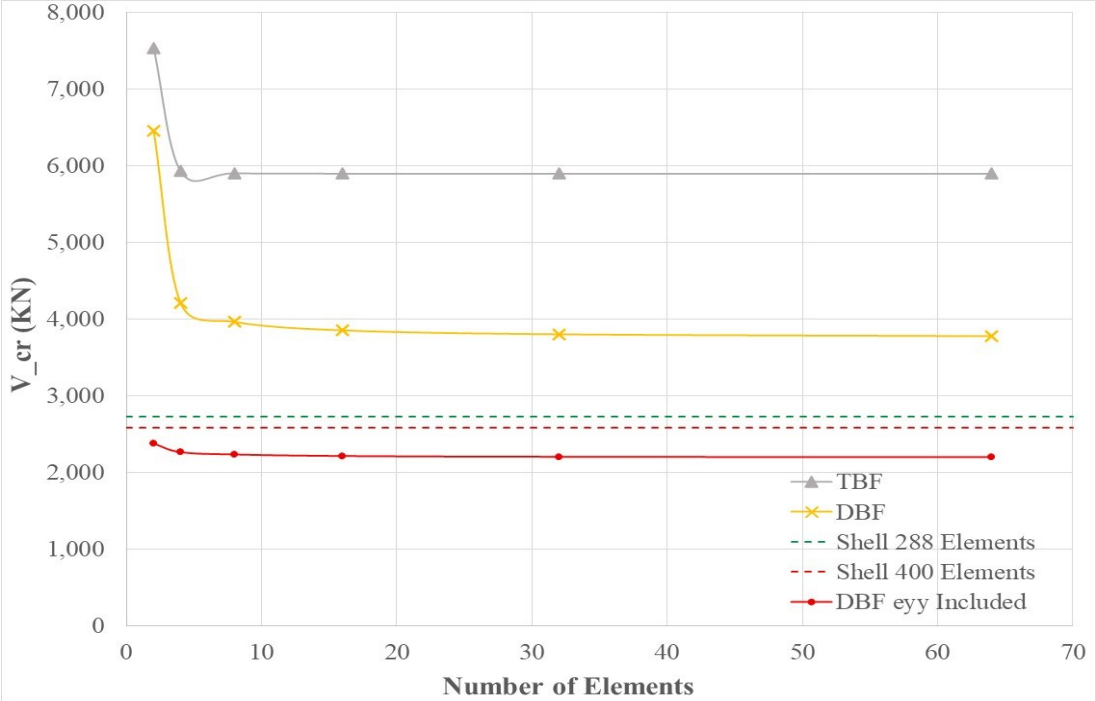

Figure 6.17 Critical mid-span load for the L=10m fixed-fixed beam

Mode shapes are demonstrated for DBF and SEF in Figure 6.18 and Figure 6.19 The agreement of mode shapes between the DBF and SEF is generally good, however gets slightly better as the span increases (see Figure 6.20 and Figure 6.21).

Considering the fact that the angle of twist for the top and bottom flanges show some differences even for the 10 m span, the distortion effects are still involved in the buckling behavior. This is because the height of the web is relatively large in this example, as also can be visually inspected from Figure 6.22.

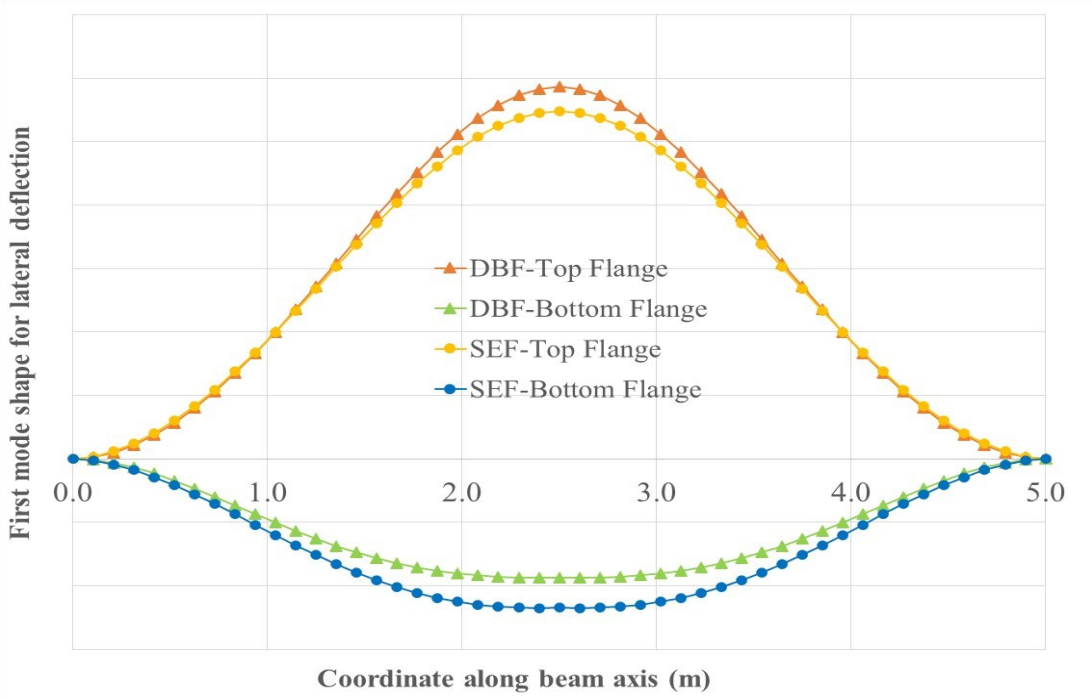

Figure 6.18 First mode shape of the L=5m beam - Top and Bottom flange Lateral Displacement (beta=0.5)

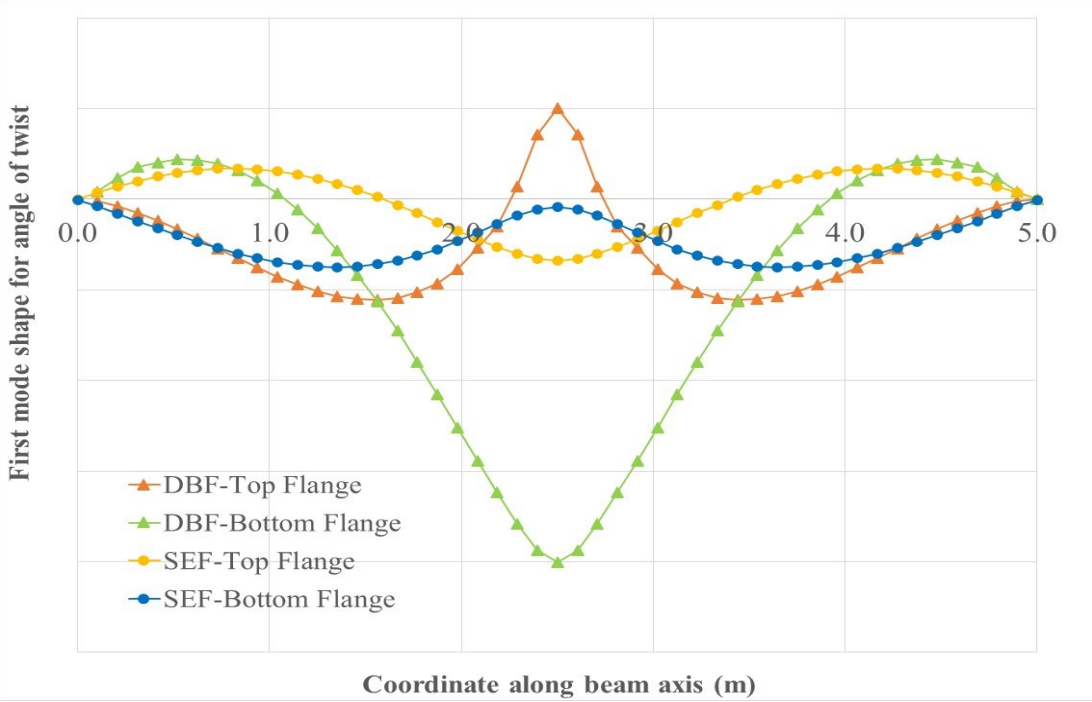

Figure 6.19 First mode shape of the L=5m beam - Top and Bottom flange Angle of Twist (beta=0.5)

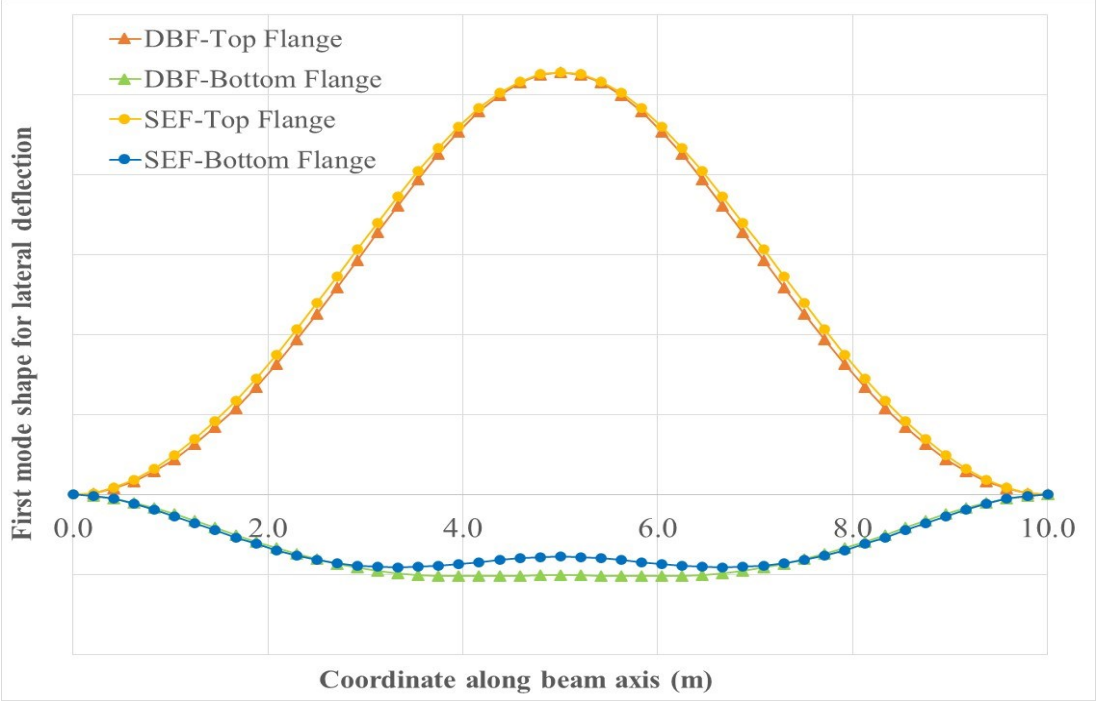

Figure 6.20 First mode shape of the L=10m beam - Top and Bottom flange Lateral Displacement (beta=0.5)

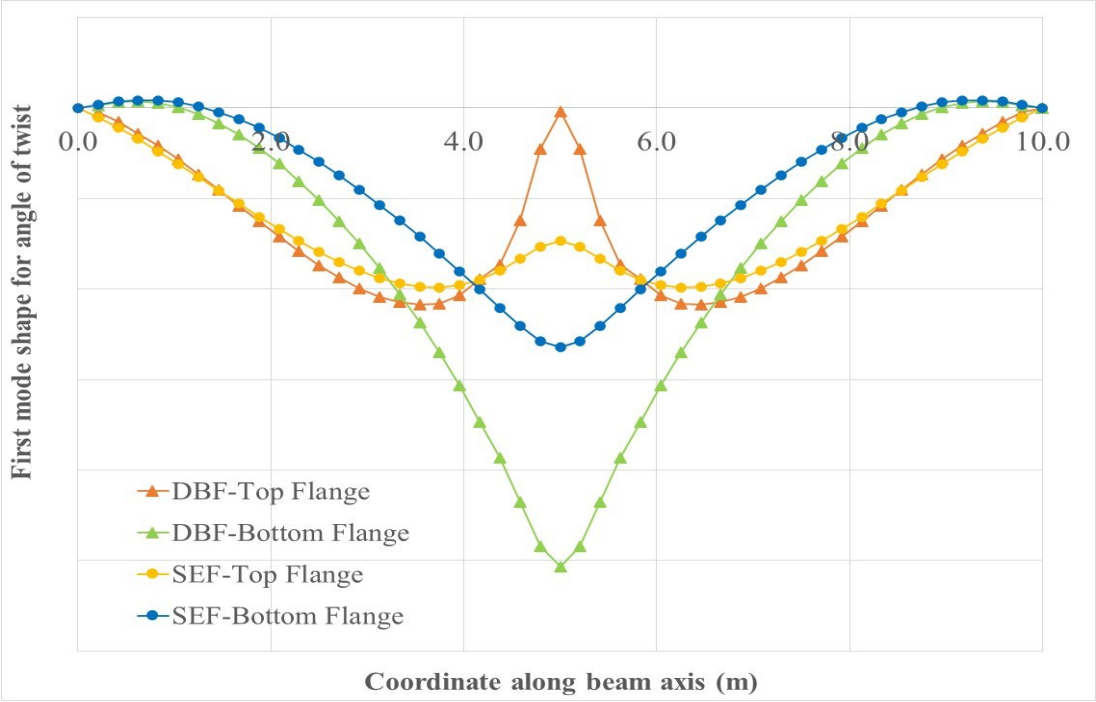

Figure 6.21 First mode shape of the L=10m beam - Top and Bottom flange Angle of Twist (beta=0.5)

In drawing the mode shapes, results of the 16 element and 288 element analyses were used for DBF and SEF, respectively.

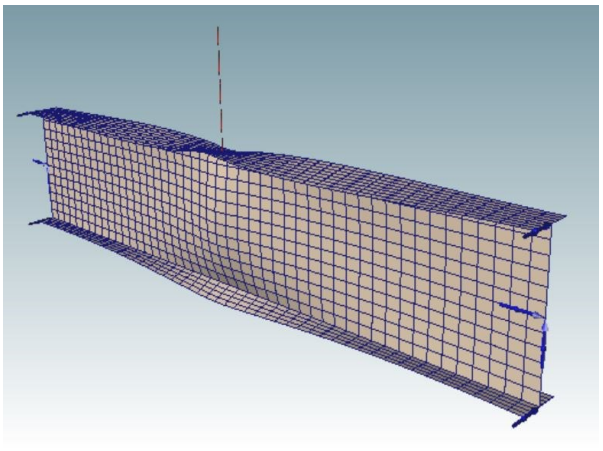

a) DBF for the L=5m fixed-fixed beam (beta=0.5)

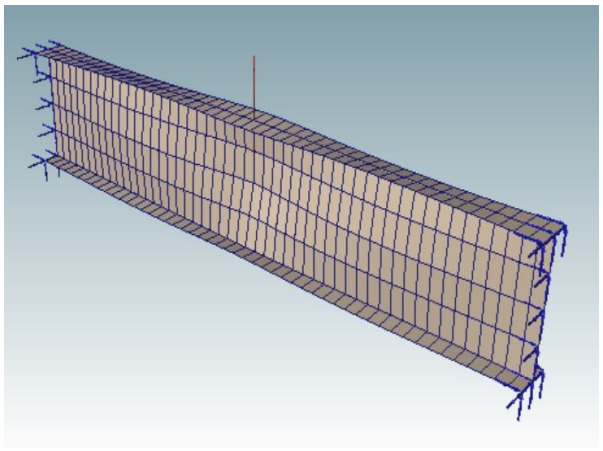

b) SEF for the L=5m fixed-fixed beam

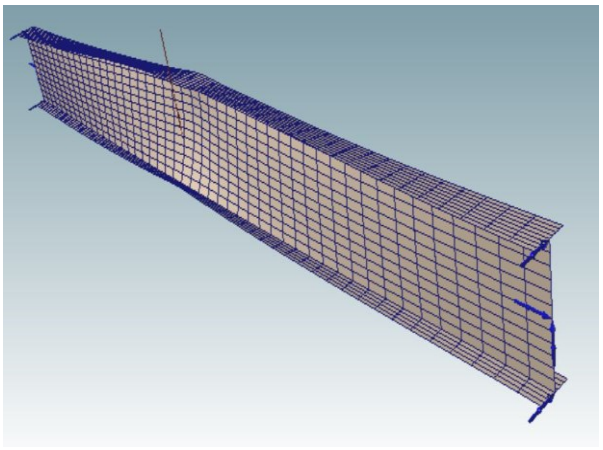

c) DBF for the L=10m fixed-fixed beam (beta=0.5)

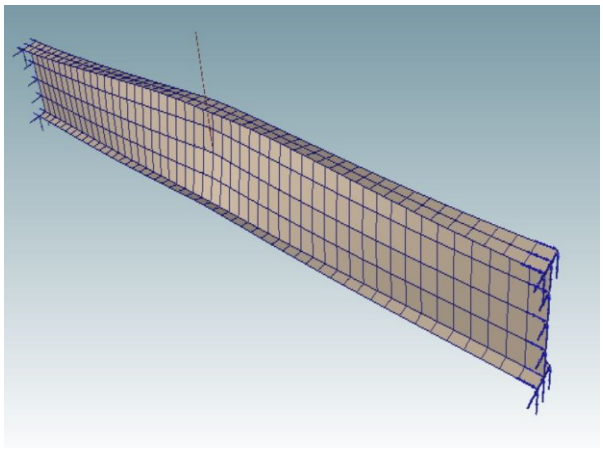

d) SEF for the L=10m fixed-fixed beam

Figure 6.22 3D Figures for the buckled shapes of the first mode

6.3. Case C: Beam restraint continuously at top-flange

A 6m span beam is analyzed under uniformly distributed load q (see Figure 6.1) and the cross-section was selected as W250x33 (class 2) for which the dimensions are b=146mm, h=248.9mm, t=9.1mm and t_w=6.1mm. The beam is pinned at the left end and roller supports are imposed at the mid-span and at the right end of the beam (see Figure 6.1). Also, the top flange of the beam is continuously restraint against lateral deflection and rotation, which is a commonly encountered situation for girders of composite highway bridges as their top flanges are generally connected to concrete decks along the span. The critical uniform load q_{cr} is calculated based on the linearized buckling analysis based on Euler-Rodriguez rotation tensor (beta=0.5) and the results are shown in Figure 6.23 for different number of elements.

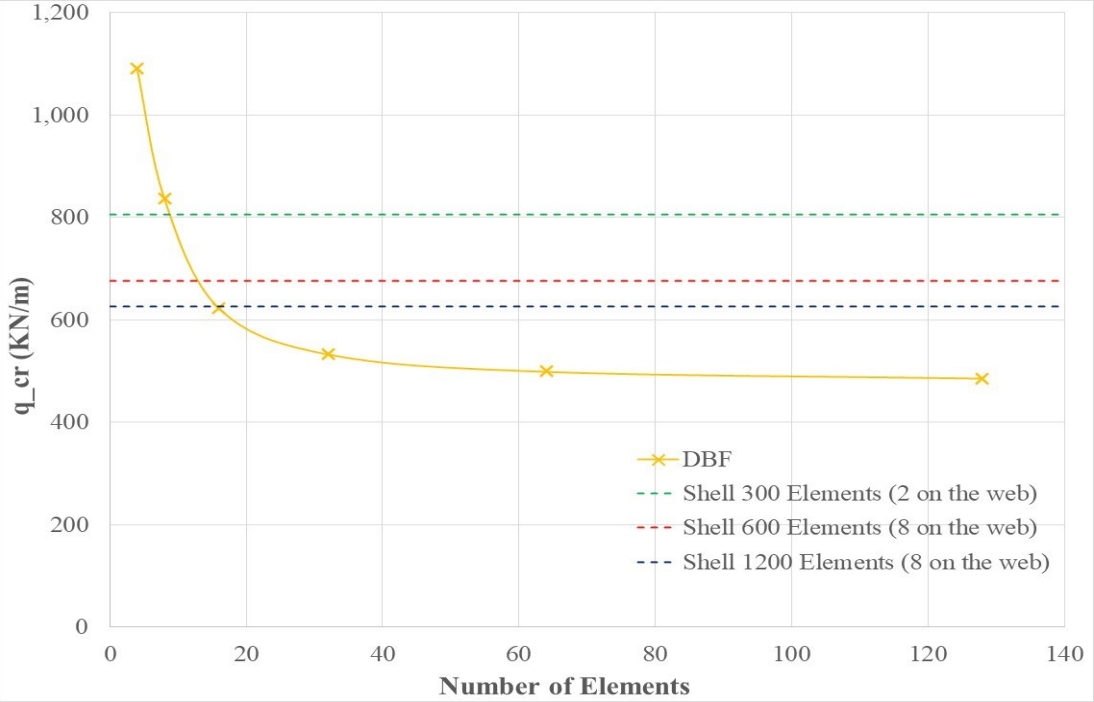

Figure 6.23 Buckling load predictions for the continuous beam under uniform vertical load

Such a case cannot be modelled by using TBF as restraining top flange would also prevent any lateral buckling mode. Therefore, in Figure 6.23, only DBF and SEF results were shown. In this example SEF results are particularly sensitive to the number of elements in the web direction as it can be seen from Figure 6.23 that when 2 elements are used along the web, the results significantly differ that of the 1200 element SEF. On the other hand, it can be verified that the predictions of the distortional beam DBF agree well with those of the SEF-based analysis.

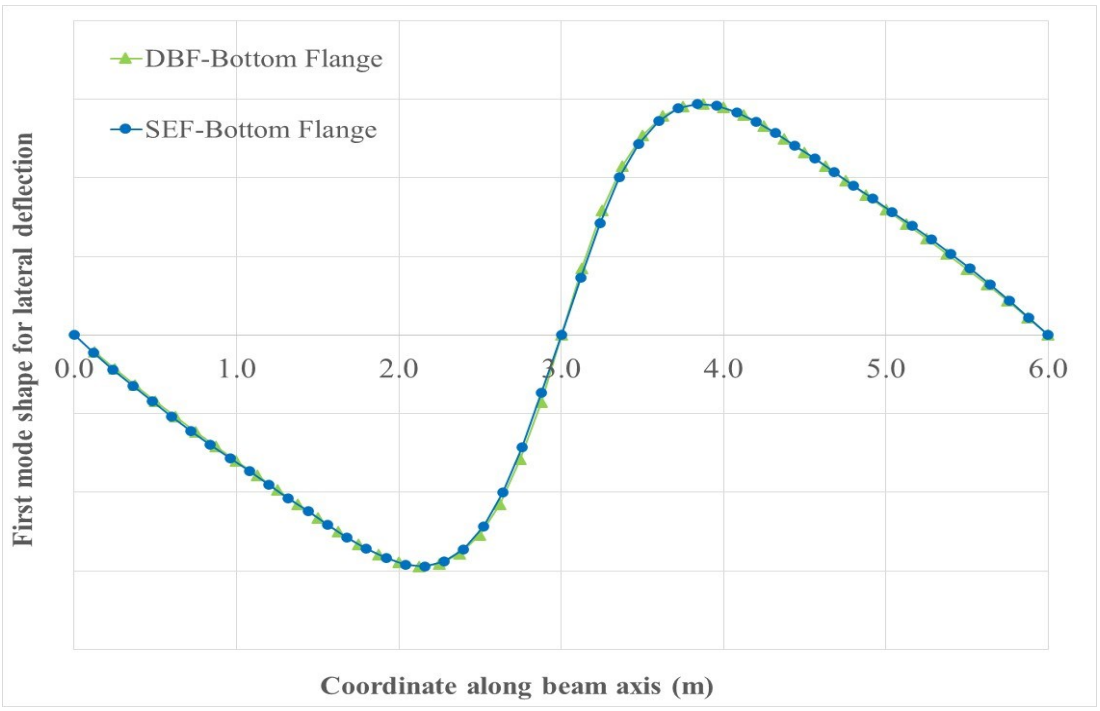

Figure 6.24 First mode of the continuous beam - Bottom flange lateral displacement

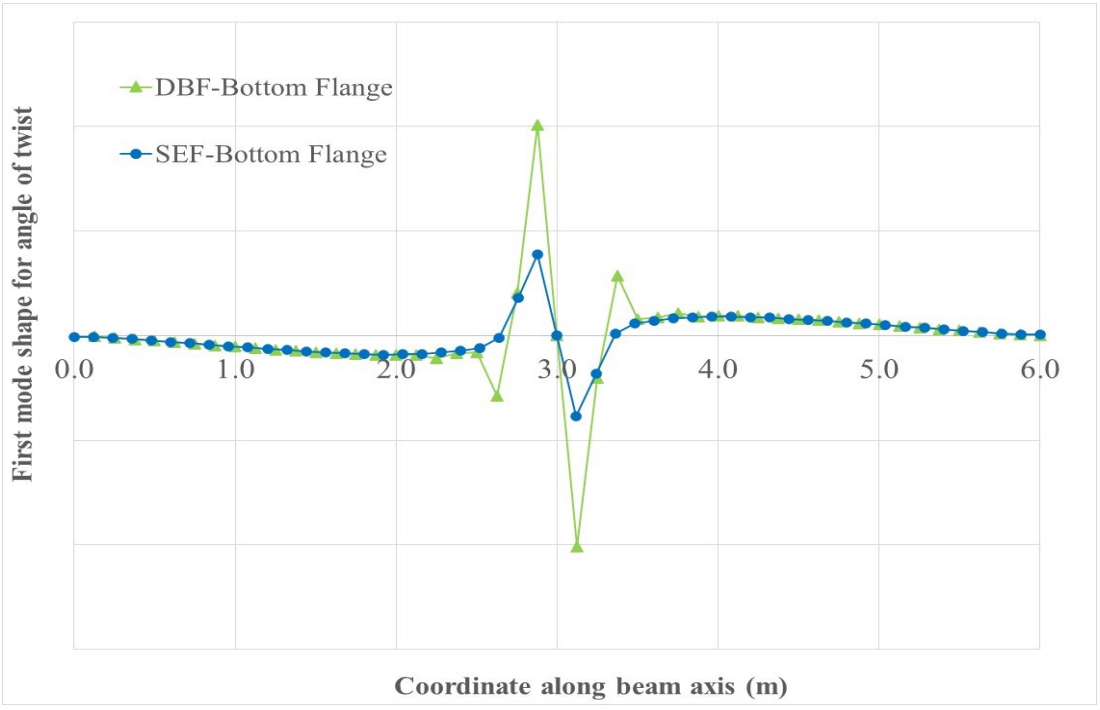

Figure 6.25 First mode shape of the continuous beam - Bottom flange Angle of Twist

The lateral deflected shape and angle of twist of the bottom flange according to the first mode are, respectively shown for both DBF and SEF in Figure 6.24 and Figure 6.25. The agreement between the SEF and DBF mode shapes are very good for the bottom flange lateral deflections in Figure 6.24, while slightly more fluctuations occur in the angle of twist results of DBF compared to that of SEF in Figure 6.25.

Figure 6.26 shows that fluctuations of the web are significant near the middle support.

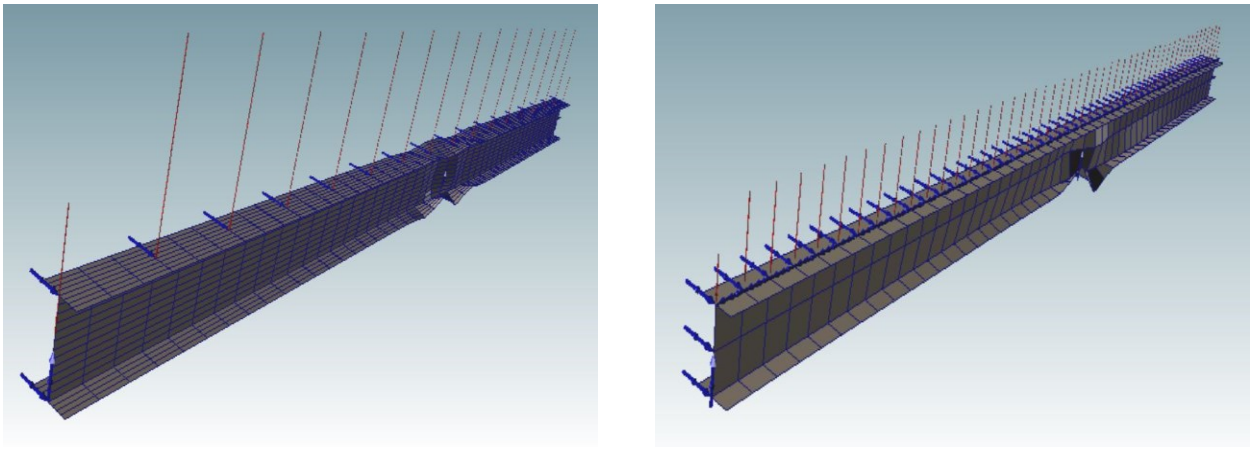

a) DBF for the L=6m beam (beta=0.5) b) SEF for the L=6m beam

Figure 6.26 3D Figures for the buckled shapes of the first mode

6.4. Case D: Mono-symmetric simply supported beam

We analyse mono-symmetric (class 2) simply supported beams with 4m and 8m spans. A vertical load is applied at the mid-span as shown in Figure 6.1. The cross-sectional dimensions are h=300.3mm, t=9.7mm, t_w=5.8mm, b_T =165mm and $b_{B=}$ 85mm (see Figure 6.1). We use 144 and 300 element SEF models. In 144 element model, the cross-section is divided into 6 elements by using two elements for the web and two elements for each flange, and the span is divided into 24 elements. In 300 element SEF model, the cross-section is divided into 6 elements by using two elements for the web and two elements for each flange, and the span is divided into 50 elements. Again, we use Euler-Rodriguez rotation tensor (beta=0.5) in this case study.

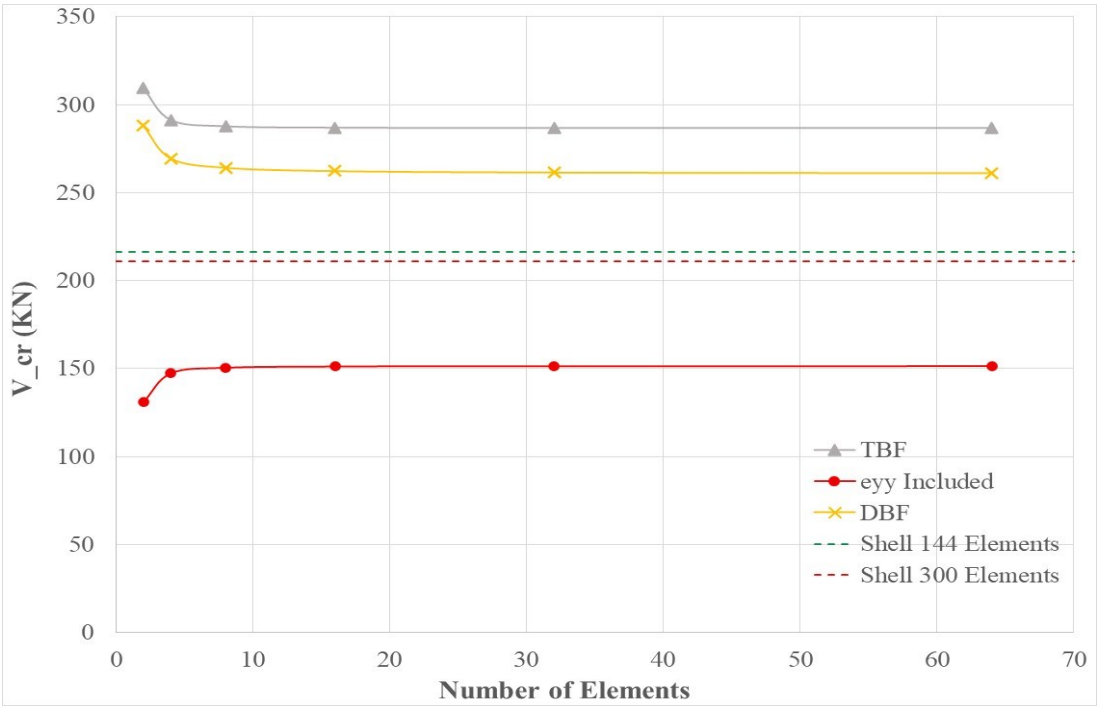

Figure 6.27 Critical mid-span load for the L=4m span

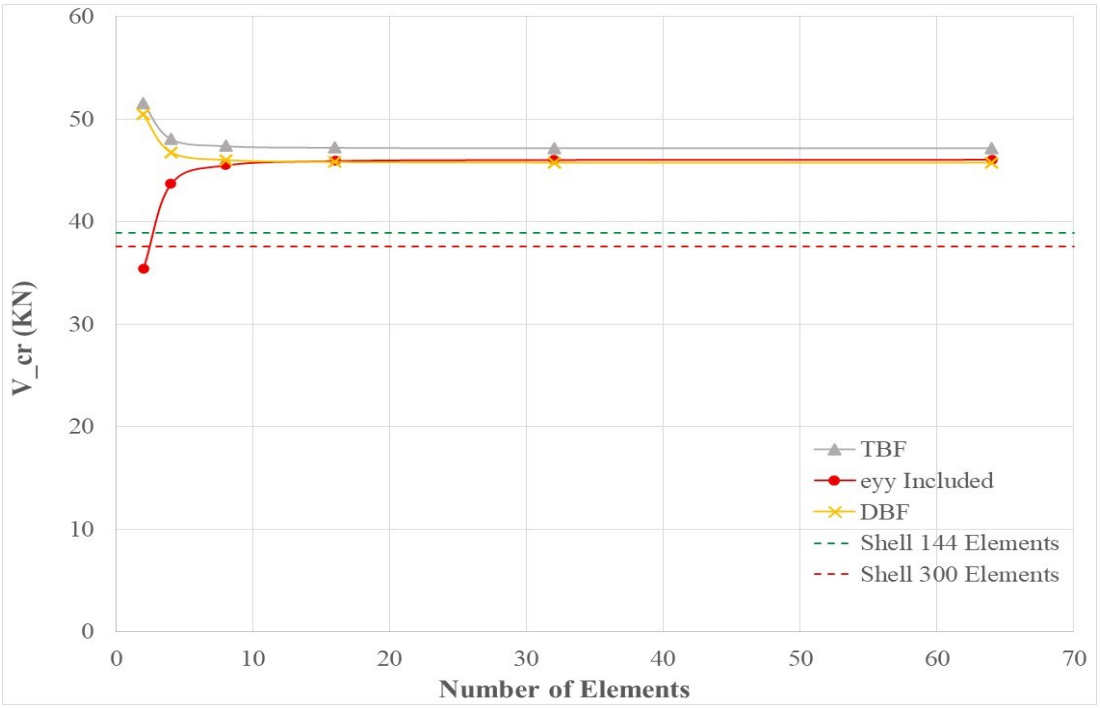

Figure 6.28 Critical mid-span load for the L=8m span

For the 4m beam, it can be verified from Figure 6.29 and Figure 6.30 that DBF lateral deflections and angle of twist agree well with those of SEF. Some discrepancies can be observed; however, they diminish as the beam span is increased to 8m as can be seen in Figure 6.31 and Figure 6.32.

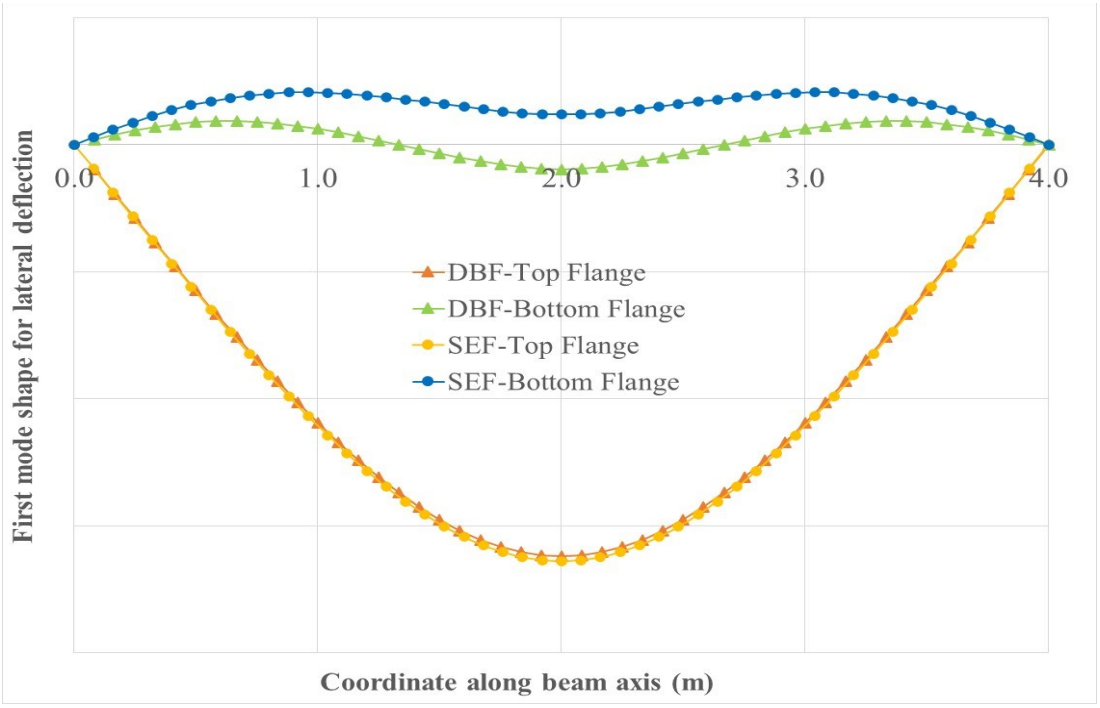

Figure 6.29 First mode shape of the L=4m beam - Top and Bottom flange Lateral Displacement

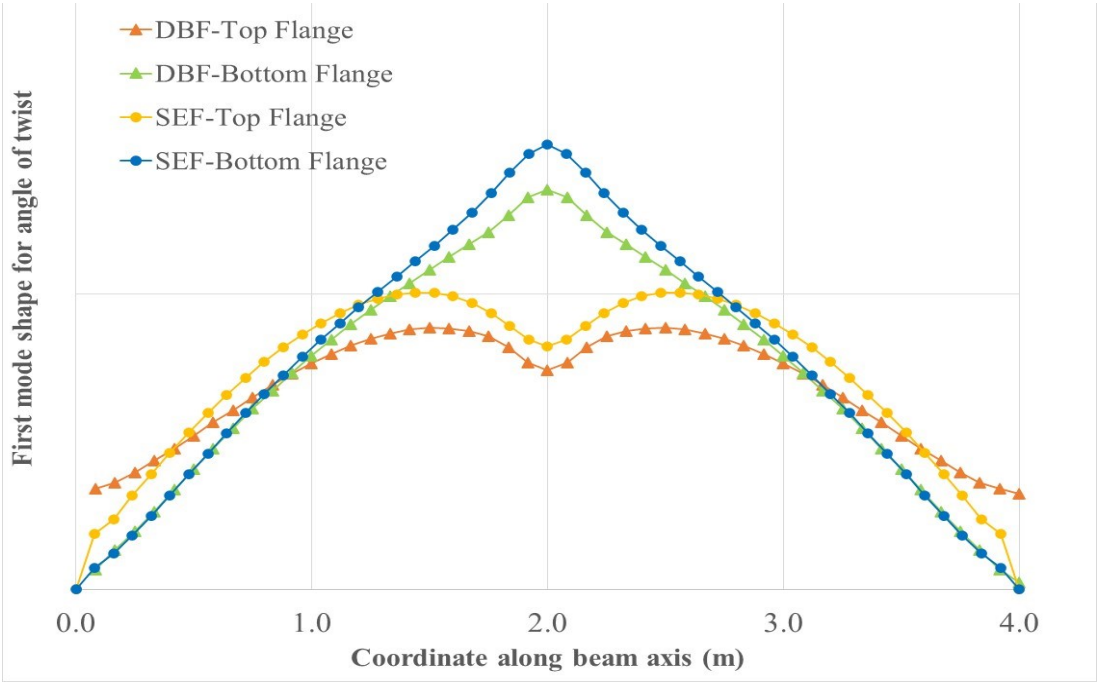

Figure 6.30 First mode shape of the L=4m beam - Top and Bottom flange Angle of Twist

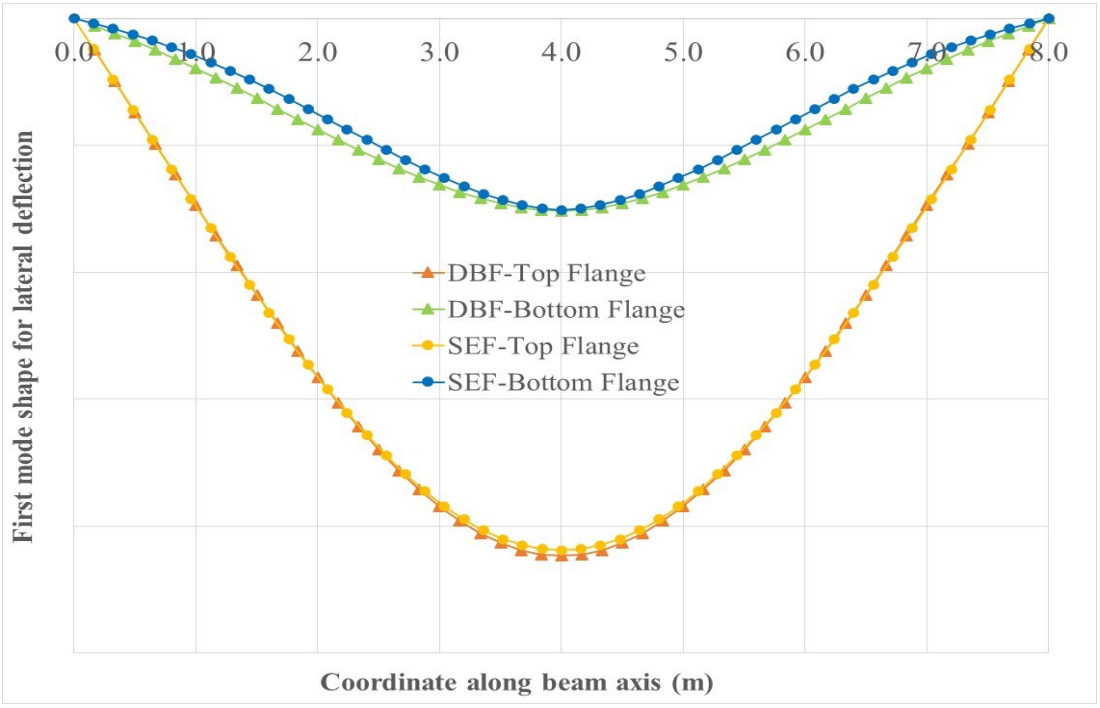

Figure 6.31 First mode shape of the L=8m beam - Top and Bottom flange Lateral Displacement

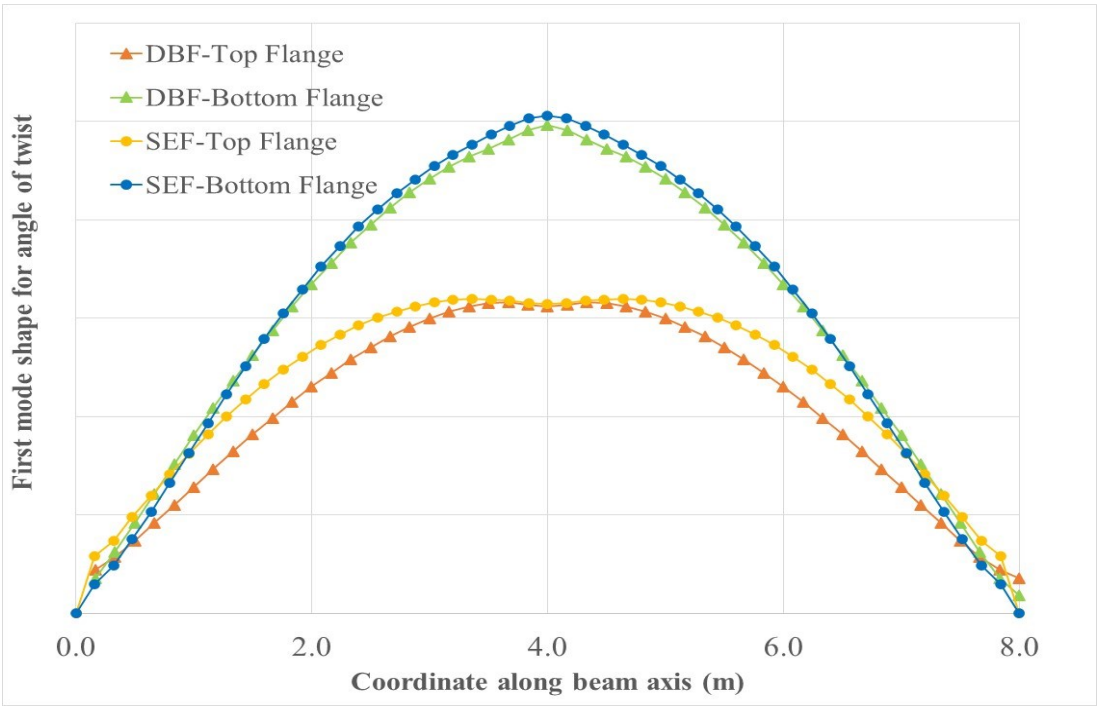

Figure 6.32 First mode shape of the L=8m beam - Top and Bottom flange Angle of Twist

In drawing the mode shapes, results of the 16 element and 175 element analyses were used for DBF and SEF, respectively. Corresponding 3D buckled mode shapes can be seen in Figure 6.33a-d.

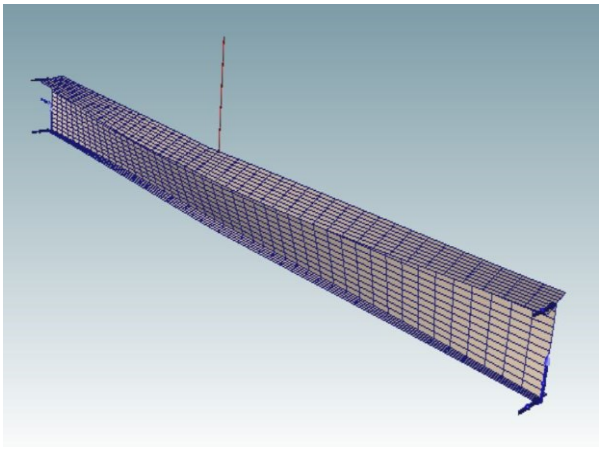

a) DBF for the L=4m beam (beta=0.5)

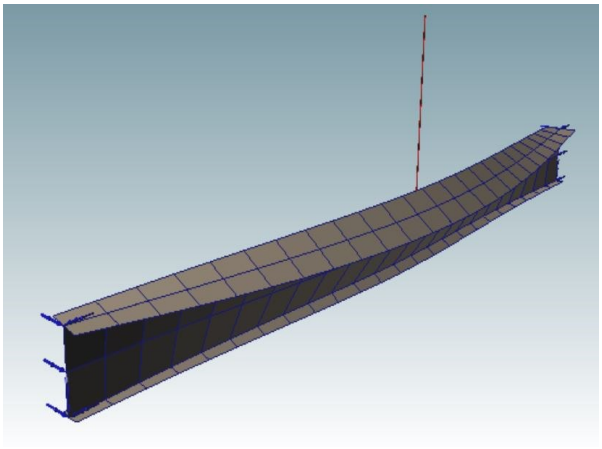

b) SEF for the L=4m beam

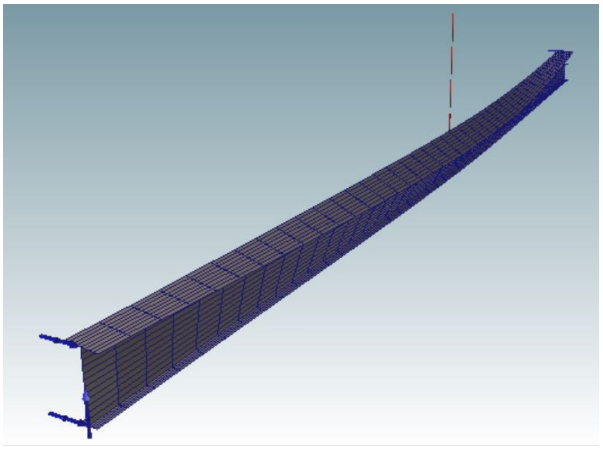

c) DBF for the L=8m beam (beta=0.5)

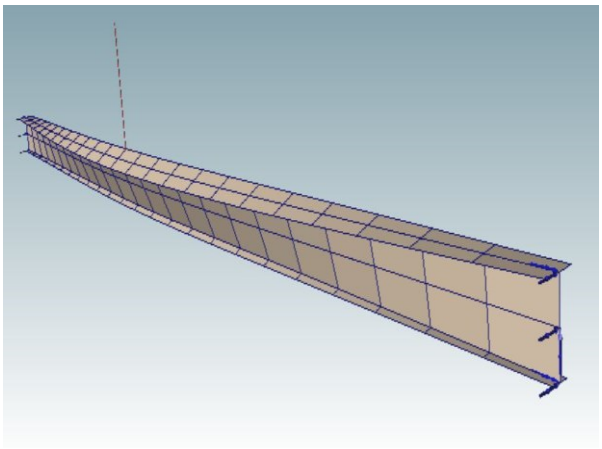

d) SEF for the L=8m beam

Figure 6.33 3D Figures for the buckled shapes of the first mode

6.5. Conclusions

A beam-type Finite Element formulation was developed for the elastic buckling and nonlinear analyses of thin-walled members including web distortion effects. The formulation was validated against shell-element based models and known solutions from the literature. It was shown that the mode shapes and the buckling loads agree very well with the results of shell element models. The applicability of the developed beam formulation was illustrated on practical case studies where web bending mode is the dominant buckling mode. It was illustrated that when using distortional beam formulations, the second order strains in the web contour direction should be included only if the pre-buckling stress analysis includes web extensibility related degrees-of-freedoms, and otherwise, the buckling load predictions considering web bending might be significantly conservative. The developed element was shown to be an accurate and efficient tool and might be especially useful for preliminary analysis when distortional-lateral-torsional buckling is a primary design concern.

6.6. References

1. Timoshenko SP (1953). Einige stabilitats probleme der Elastizitatstheorie., collected papers of Stephen Timoshenko, McGraw-Hill, Book Co. New York, N.Y.
2. Bleich M (1952). Buckling strength of metal structures. McGraw-Hill, New York, N.Y.
3. Krajcinovic D (1969). A consistent discrete elements technique for thin wall assemblages. *International Journal of Solids and Structures*; 5: 639–62.
4. Barsoum RJ, Gallagher RH (1970). Finite element analysis of torsional and torsional–flexural stability problems. *International Journal for Numerical Methods in Engineering*; 2: 335–52.
5. Bazant ZP, El-Nimeri M (1973). Large-deflection spatial buckling of thin-walled beams and frames. *Journal of Engineering Mechanics Division*; 99(6): 1259–81.
6. Roberts TM, Azizian ZG (1983). Instability of thin-walled bars. *Journal of Engineering Mechanics, ASCE*; 109:781–94.
7. Pi YL, Trahair NS (1992). Pre-buckling deflections and lateral buckling I: theory. *Journal of Structural Engineering*, *ASCE*;118(11): 2949–2967.
8. Erkmen RE, Attard MM (2011). Lateral-torsional buckling analysis of thin-walled beams including shear and pre-buckling deformation effects. *International Journal of Mechanical Sciences*; 53: 918-925
9. Schafer BW, Pekoz T (1998). Computational modeling of cold-formed steel: characterizing geometric imperfections and residual stresses. *Journal of Constructional Steel Research*; 47: 193-210.
10. Ashraf M, Gardner L, Nethercot DA (2007). Finite element modelling of structural stainless-steel cross-sections. *Thin-Walled Structures*; 44: 1048-1062.

11. Schafer BW, Li Z, Moen CD (2010). Computational modelling of cold-formed steel. *Thin-Walled Structures*;48: 752–762.
12. Dinis PB, Camotim D (2010). Local/Distortional mode interaction in cold formed steel lipped channel beams. *Thin-Walled Structures*; 48: 771–785.
13. Kalkan I, Buyukkaragoz A (2012). A numerical and analytical study on distortional buckling of doubly-symmetric steel I-beams. *Journal of Constructional Steel Research*;70: 289–97.
14. Hancock GJ (1978). Local, distortional, and lateral buckling of I-beams. *Journal of Structural Division*; 104:1787–98.
15. Adany S, Schafer BW (2008). A full modal decomposition of thin-walled, single-branched open cross-section members via the constrained finite strip method. *Journal of Constructional Steel Research*; 64: 12-29
16. Roberts TM, Jhita PS (1983). Lateral, local and distortional buckling of I-beams. *Thin-Walled Structures*; 1:289–308.
17. Wang CM, Chin CK, Kitipornchai S (1991). Parametric study on distortional buckling of monosymmetric beam-columns. *Journal of Constructional Steel Research*; 18:89–110.
18. Ronagh HR, Bradford MA (1994). Some notes on finite element buckling formulations for beams. *Computers & Structures*; 52:1119–26.
19. Pezeshky P, Mohareb M (2018). Distortional lateral-torsional buckling of beam-columns including pre-buckling deformation effects. *Computers & Structures*; 209:93–116.
20. Davies JM, Leach P (1994). Second order generalized beam theory. *Journal of Constructional Steel Research*; 31:221–241.
21. Camotim D, Silvestre N, Gonçalves R, Dinis (2004). GBT analysis of thin-walled members: New formulations and applications, In: J. Loughlan (Ed.), Thin-Walled Structures: Recent

Advances and Future Trends in Thin-Walled Structures Technology, Canopus Publishing, Bath, pp. 137-168.

22. Goncalves R, Correa R, Camotim D (2010). A new approach to the calculation of cross-sectional deformation modes in the frame-work of generalized beam theory. *Computational Mechanics*; 46: 759-781
23. Silvestre N, Camotim D, Silva NF (2011). Generalised Beam Theory revisited: from the kinematical assumptions to the deformation mode determination. *International Journal of Structural Stability and Dynamics*; 11: 969-997.
24. Oden JT (1981). Mechanics of elastic structures, 2nd ed., McGraw Hill.
25. McGuire W, Gallagher RH, Ziemian RD (2000). Matrix structural analysis. USA: Wiley.
26. Teh LH (2005). Spatial Rotation Kinematics and flexural-torsional buckling. *Journal of Engineering Mechanics, ASCE*; 131: 598–605.
27. Pi Y-L, Trahair N, Rajasekaran S (1992). Energy equations for beam lateral buckling. *Journal of Structural Engineering, ASCE*; 118: 1462–1479.
28. Vlasov VZ (1961). Thin-walled elastic beams. 2nd ed. Jerusalem, Israel: Israel Program for Scientific Translations.
29. Bažant ZP, Cedolin L (2010). Stability of Structures: Elastic, Inelastic, Fracture and Damage Theories, Oxford University Press, New York; and re-publication with updates, Dover, New York.
30. Batoz J-L, Tahar MB (1982). Evaluation of a new quadrilateral thin plate bending element. *International Journal for Numerical Methods in Engineering*; 18: 1655-1677.

31. Ibrahimbegovic A, Taylor RL, Wilson EL (1990). A robust quadrilateral membrane finite element with drilling degrees of freedom. *International Journal for Numerical Methods in Engineering*; 30: 445-457.
32. Afnani A, Erkmen RE (2016). Iterative global-local procedure for the analysis of thin-walled composite laminates. *Steel and Composite Structures*; 20: 693-718.
33. Fafard M, Beaulieu D, Dhatt G (1987). Buckling of thin-walled members by finite elements. *Computers & Structures*; 25:183-190.
34. Erkmen RE, Gottgens B (2018). A shell element for buckling analysis of thin-walled composite laminated members. *International Journal of Structural Stability and Dynamics*; 8(2).
35. Tessler A, Dong SB (1981). An hierarchy of conforming Timoshenko beam elements. *Computers & Structures*; 14:335-344.
36. Reddy JN (1997). "On Locking-free shear deformable beam elements", *Computer Methods in Applied Mechanics and Engineering* 149: 113-132.
37. Erkmen RE (2022). Elastic buckling analysis of thin-walled beams including web distortion. *Thin-walled structures;* Online
38. Mohareb M, Nowzartash F (2003). Exact finite element for nonuniform torsion of open sections. *Journal of Structural Engineering*; 129(2), 215-223.

7. Chapter 7: Including Shear Deformation Effects in Buckling Analysis of Thin-walled Laminated Composite Members

EFFECT OF USING ALTERNATIVE STRESS-STRAIN DEFINITIONS ON THE BUCKLING LOAD PREDICTIONS OF THIN-WALLED MEMBERS

Abstract: Thin-walled structural components are widely used in many industries including aerospace, building, aircraft, and shipbuilding. These types of structures are susceptible to buckling and it is important to predict their response accurately. Effect of shear deformation on buckling behaviour of thin-walled members can become significant, especially for short and stocky sections and/or when materials with relatively low shear modulus are used. There are two well-known approaches in the literature that produce contradictory results when elastic Hooke's material is adopted for the shear deformable buckling analysis of columns. The first one is developed by Engesser and the second one by Haringx. The difference between the two methods has been attributed to different assumptions for the axial force orientation at the deformed state of the column. Engesser assumes that the axial force is parallel to the beam axis in the loading state whereas, in Haringx theory, the axial force is assumed to be perpendicular to the cross-section of the beam. This difference in the assumption of force directions can be traced down to the difference in the definitions of adopted stress-strain pairs within the Doyle-Ericksen family of strains. Although several shear deformable finite element formulations have been proposed for the buckling analysis of thin-walled beams the differences that alternative stress-strain definitions might cause were not identified in the finite element context. In this paper, it is shown that alternative stress-strain definitions lead to changes in the geometric stiffness matrices of thin-walled beam finite element formulations. The effect of changes in the geometric stiffness matrix on buckling capacity predictions of thin-walled beams is illustrated through numerical tests on short FRP pultruded beams with low shear modulus.

7.1. Introduction

The use of fibre-reinforced polymer composite-laminated thin-walled members as a construction material has increased in recent years. The primary reason for this increase is their non-corrosive

nature and long-term durability, high tensile strength-to-weight ratio, electromagnetic neutrality, and resistance to chemical attack. Because of their high strength-to-weight ratios, slender structural components may be formed by using composite laminates. One of the primary design concerns for such components, however, is their susceptibility against buckling due to their slenderness; therefore, it is important to predict their buckling loads accurately for a reliable design. For fibre reinforced laminates, a thin-walled beam formulation was developed by (Bauld and Tzeng 1984), which also includes geometrically nonlinear analysis. Closed-form analytical solutions for various cases of flexural and lateral-torsional type buckling were developed by researchers including (Pandey et al. 1995, Kollar 2001, Sapkas and Kollar 2002, Kim et al 2007, and Roberts 2002 and Roberts et al. 2003). However, these formulations are limited to certain boundary and loading conditions. On the other hand, finite element method can be used to obtain solutions that are applicable to general cases. For the buckling analysis of thin-walled composite beams, finite element formulations were developed by (Omidvar and Ghorbanpoor 1996, Lee et al. 2002, Lee 2006, Back and Will 2008, and Cardoso et al. 2009).

The effect of shear deformation can gain significance in the buckling behaviour of beams when materials with low shear modulus are used, such as FRP pultruded beams. The effect of shear deformation on buckling behaviour of thin-walled members was investigated in displacement-based formulations by (Saade et al. 2004, Kim et al. 2003, Wu and Mohareb 2011, and Erkmen and Attard 2011. In (Erkmen et al. 2009) a complementary energy-based finite element formulation was developed for torsional buckling analysis of thin-walled columns and in (Erkmen and Mohareb 2008a,b) shear deformation effects were included in lateral-torsional buckling analysis by using a complementary energy-based finite element formulation. Based on a Hellinger-Reissner principle adopted for thin-walled beams, hybrid finite element formulations that can capture shear deformation effects in the buckling analysis were developed in (Erkmen 2014 and Erkmen et al. 2020).

One important aspect that is often overlooked in buckling analysis is that the material description for nonlinear strains depends on the choice of strain definition even when the material is elastic. An accurate hyperelastic material description leads to complicated expressions because the material parameters depend on finite deformations. To avoid complications in the material description, a direct adaptation of the generalized Hooke's material, where deformation independent moduli are used, is often justified by assuming that deflections are large, but strains

are small. However, literature has shown that when shear deformations are involved, contradictory buckling predictions can be produced by adopting Hooke's material directly, as in the case of Engesser versus Haringx column buckling formulas. The difference between the two methods has been attributed to different assumptions for the shear force orientations at the deformed state of the column (e.g., Attard 2003). Engesser assumes that the shear force is perpendicular to the beam axis in the loading state whereas, in Haringx theory, the shear force is assumed to be tangential to the cross section of the beam. This difference in the assumption of shear force directions can indeed be traced down to differences in the definitions of adopted strains within the Doyle-Ericksen family of strains and conjugate stresses (e.g., Bazant 2003, Attard and Hunt 2008).

In this study, we develop a shear-deformable finite element formulation that is applicable for the buckling analysis of thin-walled composite beams. The element can be used in the modelling of composite beams of any open section. The element consists of various laminates with different mechanical properties and unidirectional continuous fibres directed in arbitrary directions. The effect of fibre orientation on the buckling behaviour of thin-walled composite beams is illustrated using the developed finite element formulation for the analysis. The formulation is developed in terms of a generic member of the Doyle-Ericksen family of strains, while elastic Hooke's material is adopted for the constitutive relations. As such, the developed formulation is an extension of both Engesser and Haringx buckling formulas to thin-walled beams.

7.2. Methodology

7.2.1 Strains

The strain components can be written in terms of deflections $u(z)$, $v(z)$ and $w(z)$ of the beam axis that are parallel to *x*, *y*, *z* directions respectively, and the angle of twist $\phi_z(z)$ of the cross-section (Figure 7.1a) and additionally $\phi_x(z)$ and $\phi_y(z)$ are rotation angles around the x and y axes respectively and $\psi(z)$ is the Vlasov warping function for thin-walled beams

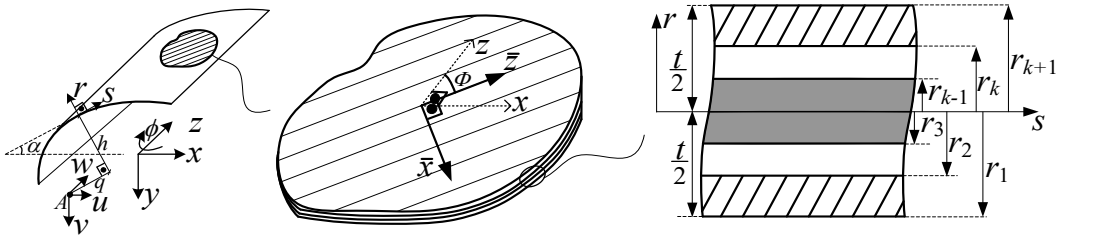

(a) Thin-walled beam **(b) Fibre orientations** **(c) Laminates across the thickness**

Figure 7.1 Thin-walled beam composed of fiber-reinforced laminates

For the Doyle-Ericksen finite strain tensor definition in continuum, we refer to (Bazant and Cedolin 2010), i.e. $\boldsymbol{\varepsilon}_m = \frac{(\boldsymbol{U}^m - \boldsymbol{I})}{m}$,, where *m* is a real parameter deciding on which member of the family, **I** is the unit tensor, and **U** is the right-stretch tensor of polar decomposition of the deformation gradient. In particular, *m*=2 produces the commonly used Green-Lagrange strain tensor, *m*=1 produces the Biot strain tensor, *m*=0 produces Hencky strain tensor and *m*=−2 produces the Almansi strain tensor. For calculating the critical loads in buckling, only the second-order approximations to the strain tensor matters. Therefore, we limit ourselves to second order accuracy in which case the strains can express as $\boldsymbol{\varepsilon}_m = \boldsymbol{\varepsilon} + \boldsymbol{e} - \eta\boldsymbol{\varepsilon}^T\boldsymbol{\varepsilon}$ which consists of six components in 3D and contains a first order strain tensor $\boldsymbol{\varepsilon}$, a second order strain tensor $\boldsymbol{e}$, and $\boldsymbol{\xi} = \boldsymbol{\varepsilon}^T\boldsymbol{\varepsilon}$ where $\eta = 1 - 0.5m$ determines which member of the Doyle-Erickson family is chosen. The formulation is restricted to prismatic thin-walled members of arbitrary cross-sections and it is based on the kinematic assumptions that; cross-section does not change its shape during deformation. Therefore, some of the strain components that causes deformations within the plane of the cross-section can be eliminated directly, i.e., $\varepsilon_{xy} = 0,\ \varepsilon_{xx} = 0,\ \varepsilon_{yy} = 0$. As a result, only the axial strain in the z direction $\varepsilon_{zz}$and the shear strains γ_{xz} on the flanges andγ_{yz} on the web survive. We define a common shear strain considering the orientation of the thin-walled segments, $\gamma = \gamma_{xz}\, cos\,\alpha + \gamma_{yz}\, sin\,\alpha$ where a is shown in Figure 7.1. Accordingly, the non-zero components of the linear strain $\boldsymbol{\varepsilon} = \langle \varepsilon_{zz} \quad \gamma \rangle^T$ can be written as

$$\varepsilon_{zz} = w' - x\phi_y' + y\phi_x' - \omega\psi' \tag{7.1}$$

$$\gamma = \left(u' - \phi_y\right) cos\,\alpha - (v' + \phi_x)\, sin\,\alpha + h(\phi_z' - \psi) - 2r\phi_z' \tag{7.2}$$

In equations 7.1 and 7.2, *x* and *y* identify coordinates of a point on the cross-section, and *r* is the normal distance from the mid-surface (Figure 7.1a). Sectorial area coordinate of the Vlasov theory was used, i.e. $\omega = \int h ds$ in which *h* is the normal distance to the tangent of the point on the section contour from the arbitrarily located pole *A* with *x* and *y* coordinates (a_x, a_y), i.e. $h = (x - a_x)\sin\alpha - \left(y - a_y\right)\cos\alpha$ (Figure 7.1a), where α is the angle between *x* and *s* axes. As shown in Figure 7.1a, *s* axis is tangent to the mid-surface of the cross-section and directed along the contour line. In equations 7.1 and 7.2, prime denotes derivative with respect to the axial

coordinate z, i.e. $()' = d()/dz$ .The non-zero components of the nonlinear strain tensor $\boldsymbol{e} = \langle e_{zz} \quad g \rangle^T$ can be written as

$$e_{zz} = \frac{1}{2}(u'^2 + v'^2) - xv''\phi_z - a_{Gx}v'\phi_z' + yu''\phi_z + a_{Gy}u'\phi_z' + \frac{1}{2}\left[(x - a_{Gx})^2 + \left(y - a_{Gy}\right)^2\right]\phi_z'^2 \tag{7.3}$$

$$g = \left(v'\phi_z - \phi_y w'\right) cos\,\alpha\ - (u'\phi_z - \phi_x w')\,sin\,\alpha\ + q\phi_z\phi_z' \tag{7.4}$$

where $q = (x - a_x)\,cos\ \alpha + (y - a_y)\,sin\ \alpha$. The non-zero components of the nonlinear strain tensor $\boldsymbol{\xi} = \langle \xi_{zz} \quad \varphi \rangle^T$ can be written as

$$\xi_{zz} = \frac{1}{4}\left(u' - \phi_y\right)^2 + \frac{1}{4}(v' + \phi_x)^2 \tag{7.5}$$

$$\varphi = w'\left(u' - \phi_y\right) cos\,\alpha\ + w'(v' + \phi_x)\,sin\,\alpha \tag{7.6}$$

7.2.2 Constitutive relations

For a laminate composed of n orthotropic layers, the orientation of the local $\overline{x}_k\overline{z}_k$-plane with respect to the global xz-plane is determined by angle ϕ about the y-axis (Figure 7.1b). Assuming that perfect interlaminar bond exists between the layers, the stress-strain relationship for the k^{th} layer can be written as follows;

$$\boldsymbol{\sigma}^{(k)} = \begin{Bmatrix} \sigma_z^{(k)} \\ \tau^{(k)} \end{Bmatrix} = \bar{\boldsymbol{Q}}^{(k)}\boldsymbol{\varepsilon}_m \tag{7.7}$$

where

$$\bar{\boldsymbol{Q}}^{(k)} = \begin{bmatrix} \bar{Q}_{11}^{*(k)} & \bar{Q}_{16}^{*(k)} \\ \bar{Q}_{16}^{*(k)} & \bar{Q}_{66}^{*(k)} \end{bmatrix} \tag{7.8}$$

in which

$$\bar{Q}^{*(k)}_{11} = \bar{Q}^{(k)}_{11} - \frac{\bar{Q}^{(k)2}_{12}}{\bar{Q}^{(k)}_{22}} \qquad \bar{Q}^{*(k)}_{16} = \bar{Q}^{(k)}_{16} - \frac{\bar{Q}^{(k)}_{12}\bar{Q}^{(k)}_{26}}{\bar{Q}^{(k)}_{22}} \qquad \bar{Q}^{*(k)}_{66} = \bar{Q}^{(k)}_{66} - \frac{\bar{Q}^{(k)2}_{26}}{\bar{Q}^{(k)}_{22}} \tag{7.9}$$

$$\overline{Q}_{11}^{(k)} = Q_{11}^{(k)} cos^4 \phi_k + 2\left(Q_{12}^{(k)} + 2Q_{66}^{(k)}\right) sin^2 \phi_k cos^2 \phi_k + Q_{22}^{(k)} sin^4 \phi_k \quad 7.10$$

$$\overline{Q}_{16}^{(k)} = \left(Q_{11}^{(k)} - Q_{12}^{(k)} - 2Q_{66}^{(k)}\right) sin \phi_k cos^3 \phi_k + \left(Q_{12}^{(k)} - Q_{22}^{(k)} + 2Q_{66}^{(k)}\right) sin^3 \phi_k cos \phi_k \quad 7.11$$

$$\overline{Q}_{66}^{(k)} = \left(Q_{11}^{(k)} + Q_{22}^{(k)} - 2Q_{12}^{(k)} - 2Q_{66}^{(k)}\right) sin^2 \phi_k cos^2 \phi_k + Q_{66}^{(k)}(sin^4 \phi_k + cos^4 \phi_k) \quad 7.12$$

and

$$Q_{11}^{(k)} = \frac{E_1^{(k)}}{1-v_{12}^{(k)} v_{21}^{(k)}} \qquad Q_{12}^{(k)} = \frac{v_{12}^{(k)} E_2^{(k)}}{1-v_{12}^{(k)} v_{21}^{(k)}} \qquad Q_{22}^{(k)} = \frac{E_2^{(k)}}{1-v_{12}^{(k)} v_{21}^{(k)}} \qquad Q_{66}^{(k)} = G_{12}^{(k)} \quad 7.13$$

where $E_1^{(k)}$ and $E_2^{(k)}$ are Young's moduli of the k^{th} layer in the local $\overline{z}_k$ and $\overline{x}_k$ directions, respectively, $G_{12}^{(k)}$is the shear moduli in $\overline{x}_k \overline{z}_k$ plane of the k^{th} layer, $v_{12}^{(k)}$ is the Poisson's ratio defined as the ratio of the transverse strain in the $\overline{x}_k$ direction to the axial strain in $\overline{z}_k$ direction, and $v_{21}^{(k)}$ is the Poisson's ratio defined as the ratio of the transverse strain in the $\overline{z}_k$ direction to the axial strain in $\overline{x}_k$ direction. The laminate configuration is limited to symmetric angle-ply stacking sequence with respect to mid-plane (Figure 7.1c). Moreover, in this research work it is assumed that all the layers are perfectly bond together and there is no delamination.

7.3. Energy functional for static and buckling analyses

For the buckling analysis herein the pre-buckling deformations are neglected. In this case the analysis can be performed in two steps. Firstly; linear static analysis is performed under applied loads for which the equilibrium equations can be obtained from the first variation of the total potential energy functional, i.e. $\delta\Pi = 0$. Secondly; the internal forces obtained from the linear static analysis are used in the stability condition, which can be obtained from the second variation of the total potential energy functional, i.e. $\delta^2\Pi = 0$.

7.3.1 Energy functional for static analysis

The equilibrium equations for linear static analysis can be obtained in the weak form using the total potential energy functional, i.e.

$$\delta\Pi = \int_L \int_A \delta \boldsymbol{\varepsilon}_m^T \underbrace{\bar{\boldsymbol{Q}}^{(k)} \boldsymbol{\varepsilon}}_{\boldsymbol{\sigma}^{(k)}} dA\, dz - \int_L \delta \boldsymbol{\Delta}^T \boldsymbol{p}\, dz \tag{7.14}$$

where the first integral term is due to strain energy stored, $\boldsymbol{p}$ is the vector of applied loads, $\boldsymbol{\Delta}$ is the displacement vector of the load application point and δ denotes variation. Note that in equation 7.14, only the linear part of the strain tensor was used and based on which the stress distribution $\boldsymbol{\sigma}^{(k)}$ can be obtained.

7.3.2 Energy functional for buckling analysis

The neutral equilibrium equations for buckling analysis can be obtained from the vanishing of the second variation of the total potential energy functional [17], i.e. $\delta^2\Pi = 0$, where

$$\delta^2\Pi = \int_L \int_A \delta \boldsymbol{\varepsilon}^T \bar{\boldsymbol{Q}}^{(k)} \delta\boldsymbol{\varepsilon} dA\, dz + \int_L \int_A \delta^2 \boldsymbol{e}^T \underbrace{\bar{\boldsymbol{Q}}^{(k)} \boldsymbol{\varepsilon}}_{\boldsymbol{\sigma}^{(k)}} dA\, dz - \eta \int_L \int_A \delta^2 \boldsymbol{\xi}^T \underbrace{\bar{\boldsymbol{Q}}^{(k)} \boldsymbol{\varepsilon}}_{\boldsymbol{\sigma}^{(k)}} dA\, dz \tag{7.15}$$

in which pre-buckling deformations are ignored. Note that $\boldsymbol{\sigma}^{(k)}$ has been obtained from the linear static analysis in equation 7.14 and substituted into equation 7.15. The first term in equation 7.15, leads to the elastic stiffness matrix, while the second and third terms leads to the geometric stiffness matrix.

7.4. Finite element formulation

The finite element formulation is obtained by interpolating the displacement fields *u*, *v*, *w*, rotation fields ϕ_x, ϕ_y and ϕ_z, and the warping function ψ using polynomial functions of the axial coordinate *z*, i.e.,

$$\begin{Bmatrix} w(z) \\ v(z) \\ \phi_x(z) \\ u(z) \\ \phi_y(z) \\ \phi_z(z) \\ \psi(z) \end{Bmatrix} = \begin{bmatrix} \boldsymbol{N} & \boldsymbol{0} & \boldsymbol{0} & \boldsymbol{0} \\ \boldsymbol{0} & \boldsymbol{L}_f & \boldsymbol{0} & \boldsymbol{0} \\ \boldsymbol{0} & \boldsymbol{M}_f & \boldsymbol{0} & \boldsymbol{0} \\ \boldsymbol{0} & \boldsymbol{0} & \boldsymbol{L}_t & \boldsymbol{0} \\ \boldsymbol{0} & \boldsymbol{0} & \boldsymbol{M}_t & \boldsymbol{0} \\ \boldsymbol{0} & \boldsymbol{0} & \boldsymbol{0} & \boldsymbol{L}_t \\ \boldsymbol{0} & \boldsymbol{0} & \boldsymbol{0} & \boldsymbol{M}_t \end{bmatrix} \begin{Bmatrix} \boldsymbol{W} \\ \boldsymbol{\Omega} \\ \boldsymbol{\Lambda} \\ \boldsymbol{\Gamma} \end{Bmatrix} \tag{7.16}$$

where, $\boldsymbol{W} = \langle w_1 \quad w_2 \rangle^T, \boldsymbol{\Omega} = \langle v_1 \quad \phi_{x1} \quad v_2 \quad \phi_{x2} \rangle^T$, $\boldsymbol{\Lambda} = \langle u_1 \quad \phi_{y1} \quad u_2 \quad \phi_{y2} \rangle^T$, $\boldsymbol{\Gamma} = \langle \phi_{z1} \quad \psi_1 \quad \phi_{z2} \quad \psi_2 \rangle^T$ are the vectors of nodal values and $\boldsymbol{N} = \langle N_1 \quad N_2 \rangle$, $\boldsymbol{L}_f = \langle L_{f_1} \quad L_{f2} \quad L_{f3} \quad L_{f4} \rangle$, $\boldsymbol{M}_f = \langle M_{f_1} \quad M_{f2} \quad M_{f3} \quad M_{f4} \rangle$, $\boldsymbol{L}_t = \langle L_{t_1} \quad L_{t2} \quad L_{t3} \quad L_{t4} \rangle$, $\boldsymbol{M}_t = \langle M_{t_1} \quad M_{t2} \quad M_{t3} \quad M_{t4} \rangle$ are the vectors of corresponding interpolation functions in which

$$N_1 = \frac{L-z}{L} \qquad N_2 = \frac{z}{L} \tag{7.17}$$

$$L_{f1} = 1 - \frac{z\alpha_f}{L(1+\alpha_f)} - \frac{3z^2}{L^2(1+\alpha_f)} + \frac{2z^3}{L^3(1+\alpha_f)} \tag{7.18}$$

$$L_{f2} = \frac{z(1+0.5\alpha_f)}{(1+\alpha_f)} - \frac{2z^2(1+0.25\alpha_f)}{L(1+\alpha_f)} + \frac{z^3}{L^2(1+\alpha_f)} \tag{7.19}$$

$$L_{f3} = \frac{z\alpha_f}{L(1+\alpha_f)} + \frac{3z^2}{L^2(1+\alpha_f)} - \frac{2z^3}{L^3(1+\alpha_f)} \tag{7.20}$$

$$L_{f4} = -\frac{0.5z\alpha_f}{(1+\alpha_f)} + \frac{z^2(0.5\alpha_f - 1)}{L(1+\alpha_f)} + \frac{z^3}{L^2(1+\alpha_f)} \tag{7.21}$$

$$M_{f1} = -\frac{6z}{L^2(1+\alpha_f)} + \frac{6z^2}{L^3(1+\alpha_f)} \tag{7.22}$$

$$M_{f2} = 1 - \frac{z(4+\alpha_f)}{L(1+\alpha_f)} + \frac{3z^2}{L^2(1+\alpha_f)} \tag{7.23}$$

$$M_{f3} = \frac{6z}{L^2(1+\alpha_f)} - \frac{6z^2}{L^3(1+\alpha_f)} \tag{7.24}$$

$$M_{f4} = \frac{z(\alpha_f - 2)}{L(1+\alpha_f)} + \frac{3z^2}{L^2(1+\alpha_f)} \tag{7.25}$$

where α_f is a shear parameter approximated as $\alpha_f = \frac{12EI_x}{GA_yL^2}$ where $EI_x$is the bending rigidity of the composite cross-section around the *x* axis and GA_y is the shear rigidity in direction y. Components of the vectors $\boldsymbol{L_t}$ and $\boldsymbol{M_t}$ in equation 7.17 are identical to those given for $\boldsymbol{L_f}$ and $\boldsymbol{M_f}$ in equations 7.18 to 7.25 except the fact that α_f should be replaced with α_t which is approximated as $\alpha_t = \frac{12EI_y}{GA_xL^2}$. As a result of the interpolation scheme, one obtains equation 7.15 in the discretised form as

$$[\boldsymbol{K} + \lambda \boldsymbol{K}_G]\delta \boldsymbol{d_b} = 0 \tag{7.26}$$

in which λ is the buckling load factor, $\boldsymbol{K}$ and $\boldsymbol{K}_G$ are the assembled elastic stiffness and geometric stiffness matrices, respectively, and $\delta\boldsymbol{d_b}$ is the vector of buckle mode shape. It should be noted that the solution for λ and the corresponding $\delta\boldsymbol{d_b}$ depends on the selected strain parameter η.

7.5. Applications

7.5.1 Lateral-torsional buckling of mono-symmetric thin-walled beam under uniform moment

A simply supported mono-symmetric section under uniform bending moment is analysed herein for validation purposes. Figure 7.2 shows the loading and boundary conditions of a 4m span beam, and the dimensions of the cross-section of the analysed beam.

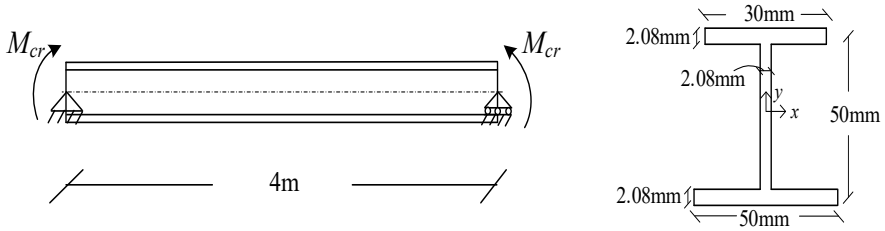

(a) Simply supported beam **(b) Cross-section**

Figure 7.2 Mono-symmetric beam under uniform bending moment

Flanges and the web are laminated symmetrically with respect to their mid-plane using 16 layers of equal thickness. For the examples considered herein the material of the beams is glass-epoxy and the values of material properties are provided in Table 7-1.

Table 7-1. Values of material properties for glass-epoxy composite (GPa)

E_1	E_2	G_{12}	υ_{12}	υ_{21}
53.78	17.93	8.96	0.25	0.25

Stacking sequence of the layers and the corresponding buckling moments based on the current study and those based on ABAQUS shell element model used in (Kim et al. 2007) are shown in Table 7-2. It can be verified that the results are in good agreement and thus lateral buckling behaviour can be captured with the proposed finite element formulation without requiring sophisticated shell element models.

Table 7-2. Critical moments for the simply supported beam in Figure 7.2 (Nmm)

Stacking sequence	This study sixteen elements-No shear effect	This study sixteen elements-Shear effect with m=2	This study sixteen elements-Shear effect with m=-2	Kim et al (2007)
$[0]_{16}$	47.30	47.30	47.30	46.560
$[15/-15]_{4S}$	46.76	46.76	46.76	48.794

$[30/-30]_{4S}$	42.9	42.90	42.90	49.624
$[45/-45]_{4S}$	36.57	36.57	36.57	44.611
$[60/-60]_{4S}$	32.6	32.6	32.6	37.730
$[75/-75]_{4S}$	30.1	30.1	30.1	31.359
$[0/90]_{4S}$	39.48	39.48	39.48	38.792
$[0/-45/90/45]_{2S}$	38.44	38.44	38.44	41.970

It should be noted that by selecting m=2 or m=-2, one obtains Green-Lagrange or Almansi strains, respectively. Effect of fibre-orientation on the buckling moment predictions of both simply supported beam is illustrated in Figure 7.3.

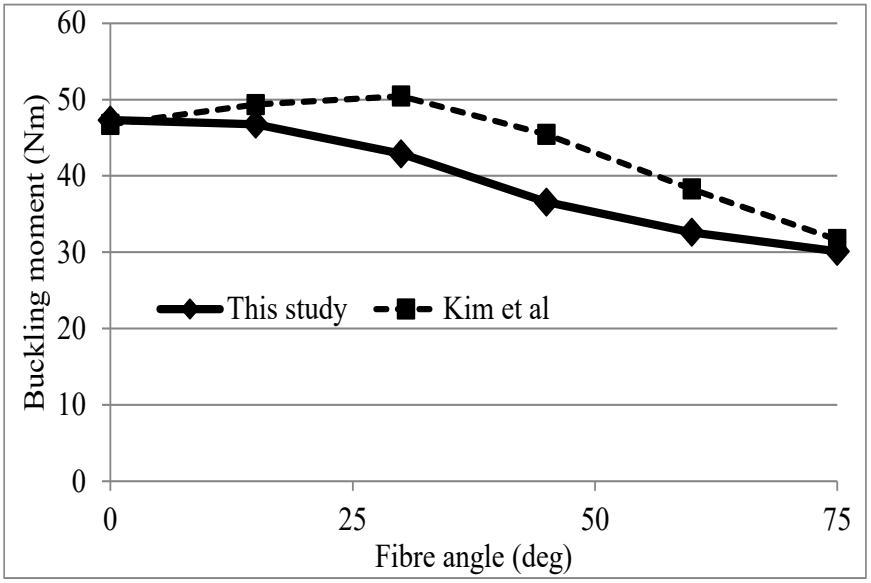

Figure 7.3 Critical buckling moments according to lay-up [±Φ]4S

7.5.2 Lateral-torsional buckling of simply supported symmetric I-section under uniform load

In this example the buckling predictions are illustrated by using the developed formulation for the analysis of a simply supported symmetric I-section under uniform distributed load as shown in Figure 7.4.

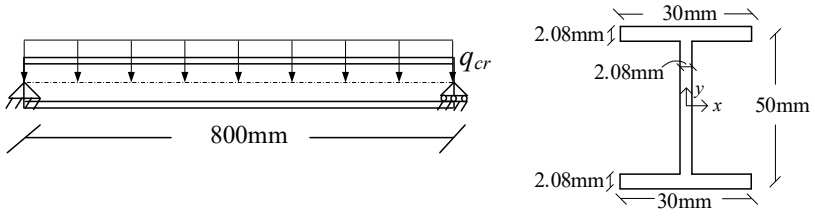

(a) Boundary conditions and loading **(b) Cross-section**

Figure 7.4 Symmetric simply supported beam under distributed load

The material properties are same as in the previous example and given in Table 7-1. The distributed load is applied at the beam's centroidal axis. Results are compared with those based on (Sapkas and Kollar 2002) in which a formulation was suggested as

$$q_{cr} = \frac{8}{L^2} \times 1.13 M_{yz} \qquad 7.27$$

where $M_{yz} = \sqrt{(\pi^2 EI_y/L^2)(GJ_d + \pi^2 EI_w/L^2)}$. Results are shown for various different stacking sequences in Table 7-3.

Table 7-3. Critical uniform loads for the simply supported beam in Figure 7.4 (N/m)

Stacking sequence	This study sixteen elements-No shear effect	This study sixteen elements-Shear effect with *m*=2	This study sixteen elements-Shear effect with *m*=-2	Eq.7.27
$[0]_{16}$	3.60	3.59	3.59	3.88
$[15/-15]_{4S}$	3.35	3.35	3.35	3.78
$[30/-30]_{4S}$	2.70	2.70	2.70	3.42
$[45/-45]_{4S}$	2.06	2.06	2.06	2.85
$[60/-60]_{4S}$	1.76	1.76	1.76	2.26
$[75/-75]_{4S}$	1.63	1.63	1.63	1.85
$[0/90]_{4S}$	2.61	2.61	2.61	2.81
$[0/-45/90/45]_{2S}$	2.34	2.34	2.34	2.80

Effect of fibre orientation is shown in Figure 7.5.

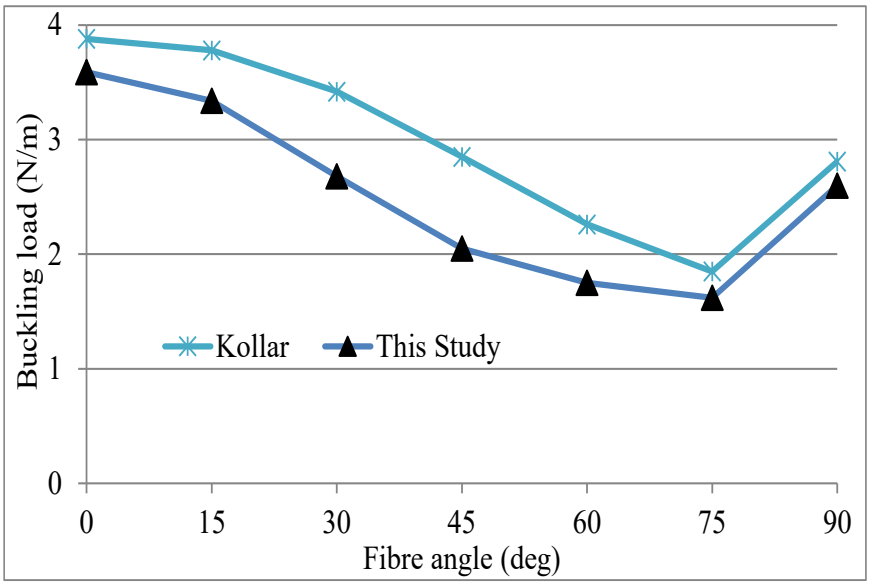

Figure 7.5 Critical buckling loads according to lay-up [±Φ]4S

7.5.3 Flexural buckling of simply supported symmetric I-section under compressive load

In the literature one can find two different classical formulas suggested for the buckling analysis of shear deformable columns, namely by Engesser and Haringx. The buckling predictions based on Engesser P_E and Haringx P_H can be expressed, respectively as follows:

$$P_E = \frac{P_s P_b}{P_s + P_b} \tag{7.28}$$

and

$$P_H = \frac{1}{2}\left(\sqrt{P_s^2 + 4P_s P_b} - P_s\right) \tag{7.29}$$

in which

$$P_b = \pi^2 EI/L^2 \tag{7.30}$$

is the Euler buckling load where EI is the flexural rigidity and L is the effective length, and $P_s = GA$ is the shear buckling load in which GA is the shear rigidity. For very large shear rigidity cases, the critical load will approach P_b in both methods. However, in shear-weak cases, Engesser solution yields $P_E = P_s$ and Haringx theory obtains a significantly different result as $P_H = \sqrt{P_s P_b}$.

In this example, the simply supported beam shown in Figure 7.6 below is analysed under compressive load. The material properties are the same as in the previous examples as given in Table 7-1. The span is 100mm and buckling occurs around the y axis. The flexural buckling load predictions based on the proposed solution strategy herein are compared with those based on Euler, Engesser and Haringx column buckling solutions in Table 7-4.

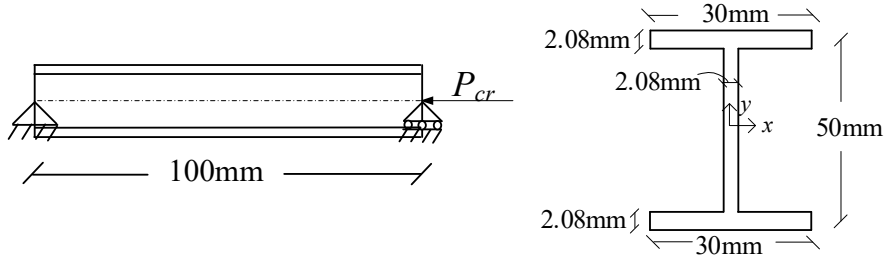

(a) Boundary conditions and loading **(b) Cross-section**

Figure 7.6 Symmetric simply supported beam under compressive load

Table 7-4. Critical compressive loads for the simply supported beam in Figure 7.6 (N)

Stacking sequence	This study-sixteen elements-Shear effect with m=2	This study-sixteen elements-Shear effect with m=-2	This study-sixteen elements-No shear effect	Engesser P_E Eq. 7.28	Haringx P_H Eq. 7.29	Euler P_b Eq. 7.30
$[0]_{16}$	352.24	383.03	513.77	351.97	382.69	513.68
$[15/-15]_{4S}$	333.38	356.34	462.50	333.11	356.03	462.16
$[30/-30]_{4S}$	269.38	279.48	338.85	269.23	279.30	338.80
$[45/-45]_{4S}$	197.40	201.27	231.40	197.35	201.21	231.43
$[60/-60]_{4S}$	161.79	164.05	184.51	161.70	163.95	184.45
$[75/-75]_{4S}$	150.92	153.13	172.75	150.84	153.04	172.71
$[0/90]_{4S}$	262.34	275.08	342.48	262.15	274.87	342.46
$[0/-45/90/45]_{2S}$	232.74	240.18	286.94	232.60	240.02	286.89

The effect of fibre orientation is shown in Figure 7.7.

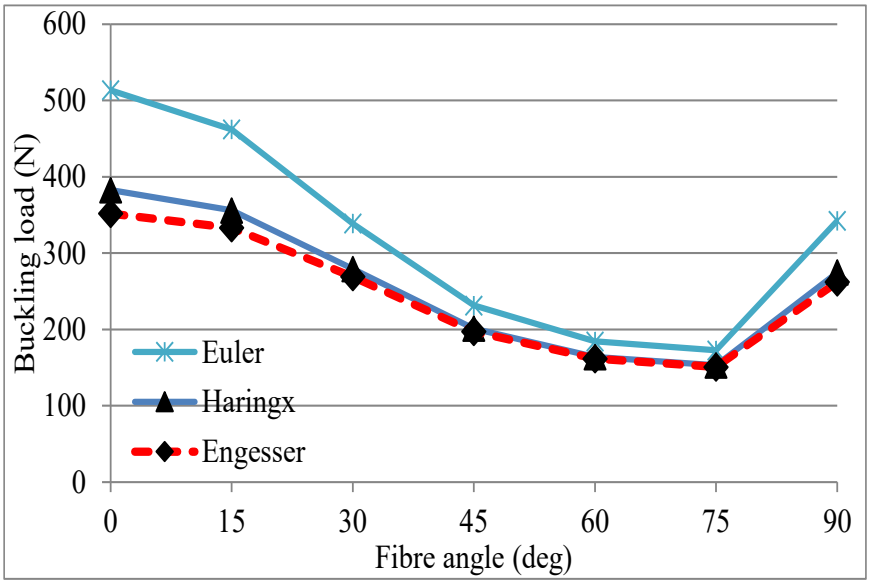

Figure 7.7 Critical buckling loads according to lay-up [±Φ]4S

7.6. Conclusions, and Recommendations

7.6.1 Conclusions

The proposed formulation for buckling analysis of thin-walled beams was validated against known solutions from the literature. In the case of long slender beams under uniform bending moment loading the results agree well with those of a shell-type model from literature and including shear deformations have no effect on the results. The effect of shear deformation and stress-strain definitions in buckling load predictions were not significant in the analysed lateral-torsional buckling problems. However, in the case of a short column problem, it was shown that Engesser

and Haringx solutions lead to significantly different result. In the finite element analysis context, this difference is due to differences in the definitions of adopted stresses which affect the geometric stiffness matrix within the linearized eigenvalue problem. The finite element results based on the proposed methodology exactly match with those based on the analytical results of Engesser, Haringx, and Euler when corresponding stress-strain definitions are used. That confirms that the formulation is capable of capturing the shear deformation effects very accurately. The Engesser's formula provided more conservative results comparison to that of the Haringx and as Euler's formula neglects shear deformation effects, it is unconservative when shear deformations are significant. The effect of the fiber orientation on the buckling predictions was also illustrated in all three cases studied herein.

7.6.2 Recommendations for Future Work

Recommendations for future work include:

1. The present distortional theory can be utilized for thin-walled beams to consider the effect of pre-buckling deformation and shear deformation effects in buckling analysis which can lead to improved design rules.
2. The present finite element solution can be applied to determine the distortional buckling response of fibre-reinforced polymer composite-laminated thin-walled members which was limited to rigid web assumption in chapter 7.
3. The developed formulation can be extended for tapered beams and thin-walled channels.
4. The formulation can be extended for inelastic nonlinear analysis of thin-walled beams.

7.7. References

Bauld Jr, N. R., & Lih-Shyng, T. 1984. A Vlasov theory for fiber-reinforced beams with thin-walled open cross sections. *International Journal of Solids and Structures*, **20**(3): 277-297.

Pandey, M. D., Kabir, M. Z., & Sherbourne, A. N. 1995. Flexural-torsional stability of thin-walled composite I-section beams. *Composites Engineering*, **5**(3): 321-342.

Sapkás, Á., & Kollár, L. P. 2002. Lateral-torsional buckling of composite beams. *International Journal of Solids and Structures*, **39**(11): 2939-2963.

Kim, N. I., Shin, D. K., & Kim, M. Y. 2007. Exact lateral buckling analysis for thin-walled composite beam under end moment. *Engineering Structures*, **29**(8): 1739-1751.

Roberts, T. M. 2002. Influence of shear deformation on buckling of pultruded fiber reinforced plastic profiles. *Journal of Composites for Construction*, **6**(4): 241-248.

Roberts, T. M., & Masri, H. M. K. J. A. H. 2003. Section properties and buckling behavior of pultruded FRP profiles. *Journal of reinforced plastics and composites*, **22**(14): 1305-1317.

Omidvar, B., & Ghorbanpoor, A. 1996. Nonlinear FE solution for thin-walled open-section composite beams. *Journal of Structural Engineering*, **122**(11): 1369-1378.

Lee, J., Kim, S. E., & Hong, K. 2002. Lateral buckling of I-section composite beams. *Engineering Structures*, **24**(7): 955-964.

Lee, J. 2006. Lateral buckling analysis of thin-walled laminated composite beams with monosymmetric sections. *Engineering structures*, **28**(14): 1997-2009.

Back, S. Y., & Will, K. M. 2008. Shear-flexible thin-walled element for composite I-beams. *Engineering Structures*, **30**(5): 1447-1458.

Cardoso, J. B., Benedito, N. M., & Valido, A. J. 2009. Finite element analysis of thin-walled composite laminated beams with geometrically nonlinear behavior including warping deformation. *Thin-Walled Structures*, **47**(11): 1363-1372.

Saadé, K., Espion, B., & Warzée, G. 2004. Non-uniform torsional behavior and stability of thin-walled elastic beams with arbitrary cross sections. *Thin-walled structures*, **42**(6): 857-881.

Moon-Young, K., Nam II, K., & Hee-Taek, Y. 2003. Exact dynamic and static stiffness matrices of shear deformable thin-walled beam-columns. *Journal of sound and vibration*, **267**(1): 29-55.

Wu, L., & Mohareb, M. 2011. Buckling formulation for shear deformable thin-walled members—II. Finite element formulation. *Thin-walled structures*, **49**(1): 208-222.

Erkmen, R. E., & Attard, M. M. 2011. Lateral–torsional buckling analysis of thin-walled beams including shear and pre-buckling deformation effects. *International journal of mechanical sciences*, **53**(10): 918-925.

Erkmen, R. E., Mohareb, M., & Bradford, M. A. 2009. Complementary energy based formulation for torsional buckling of columns. *Journal of engineering mechanics*, **135**(12): 1420-1426.

Erkmen, R. E., & Mohareb, M. 2008. Buckling analysis of thin-walled open members—a complementary energy variational principle. *Thin-walled structures*, **46**(6): 602-617.

Erkmen, R. E., & Mohareb, M. 2008. Buckling analysis of thin-walled open members—a finite element formulation. *Thin-walled structures*, **46**(6): 618-636.

Erkmen, R. E. 2014. Shear deformable hybrid finite-element formulation for buckling analysis of thin-walled members. *Finite Elements in Analysis and Design*, **82**: 32-45.

List of Symbols

x, y, z	Cartesian coordinates
s	Coordinate in the tangential direction of the plate segment
r	Coordinate in the thickness direction of the plate segment
α	Angle between x and s directions
a_G	Global pole
$u(y,z)$	Horizontal displacement of a point
$\bar{u}(z)$	Horizontal displacement of the global pole
$v(x,y,z)$	Vertical displacement of a point
$\bar{v}(z)$	Vertical displacement of the global pole
$w(x,y,z)$	Axial displacement of a point
$\bar{w}(z)$	Axial displacement of the global pole
φ_x	Rotation angle around the x-axis
φ_y	Rotation angle around the y-axis
$\phi_z(y,z)$	Angle of twist around the z-axis
$\psi(y,z)$	Generalized global warping displacement
β	Parameter to decide on the contribution of the second order rotation
$\hat{\omega}$	Local warping function
$\tilde{\omega}$	Global warping function
q	Coordinate in the tangential direction of the plate segment *w.r.t.* the pole
h	Coordinate in the thickness direction of the plate segment *w.r.t.* the pole
$\mathbf{I}$	Unit tensor
$\mathbf{U}$	Right stretch tensor
$\boldsymbol{\varepsilon}_m$	Green-Lagrange strain tensor
$\boldsymbol{\varepsilon}$	First order strain tensor
$\mathbf{e}$	Second order strain tensor

$\varepsilon_{zz}, \varepsilon_{yy}, \varepsilon_{xz}, \varepsilon_{yz}$	Non-zero components of the strain tensor
γ	Shear strain
κ	Switch of interpolation functions along the web direction.
ρ	Twist curvature of the plate segment
ϕ	Angle of rotation of the plate segment around *z*-axis
ϖ	Angle of rotation of the plate segment around *q*-axis
$\theta,\ r_{sk}$	Angle of rotation of the plate segment around *r*-axis
J	Torsional constant of the plate segment around *z*-axis
M_t	Twisting moment acting on the plate segment around *z*-axis
b	Width of the plate segment
t	Thickness of the plate segment
h_w	Height of the web
μ	Parameter to decide on the contribution of ε_{yy}
δ	Variation operator
$\bar{\mathbf{s}}$	Matrix of cross-sectional coordinates
$\boldsymbol{\chi}_L, \boldsymbol{\chi}_A$	Vector of displacement derivatives
$\mathbf{A}$	Matrix of displacement derivatives to compute first variations of strains
$\mathbf{t}_1, \mathbf{t}_2,\ \mathbf{t}_{G2}$	Matrices to re-order displacement derivatives
$\mathbf{G}_1, \mathbf{G}_2$	Matrix of displacement derivatives to compute second variations of strains
$\boldsymbol{\sigma}_m$	Stress tensor
$\mathbf{E}_a, \mathbf{E}_b$	Constitutive matrices
A	Cross-sectional area
L	Element span
Π	Total potential energy functional
W^{int}	Internal strain energy functional
W^{ext}	External load potential functional

$\widehat{\Pi}$	Modified energy functional
$\mathbf{P}^{\text{ext}}$	External load vector
$\mathbf{B}_n, \mathbf{B}_l, \mathbf{B}_G$	Matrices of discrete strain-displacement relations
$\mathbf{M}_G$	Matrix relating displacements and strains
$\mathbf{N}_B$, $\tilde{\mathbf{N}}$, **L**, **M**, **N**	Matrices of interpolation functions
H_1, H_2, H_3, H_4	Hermitian functions
$\widehat{H}_1, \widehat{H}_2, \widehat{H}_3, \widehat{H}_4$	Modified Hermitian functions
$\mathbf{K}_l, \mathbf{K}_e, \mathbf{K}_g$	Stiffness matrices
$\tilde{\mathbf{T}}$	Matrix to impose rigid web constraint
u	Vector of displacement functions
$\mathbf{d}, \tilde{\mathbf{d}}$	Nodal displacement vectors
w_1, w_2	Nodal axial displacements
v_1, v_2	Nodal vertical displacements
ϕ_{x1}, ϕ_{x2}	Nodal rotations around *x*-axis
u_{B1}, u_{B2}	Nodal horizontal displacements of the bottom flange
ϕ_{yB1}, ϕ_{yB2}	Nodal rotations around *y*-axis of the bottom flange
ϕ_{zB1}, ϕ_{zB2}	Nodal rotations around *z*-axis of the bottom flange
ψ_{B1}, ψ_{B2}	Nodal generalized warping displacements of the bottom flange
u_{T1}, u_{T2}	Nodal horizontal displacements of the top flange
ϕ_{yT1}, ϕ_{yT2}	Nodal rotations around *y*-axis of the top flange
ϕ_{zT1}, ϕ_{zT2}	Nodal rotations around *z*-axis of the top flange
ψ_{T1}, ψ_{T2}	Nodal generalized warping displacements of the top flange
w	Vector of nodal axial displacements
$\mathbf{\Omega}$	Vector of nodal vertical displacements and rotations around *x*-axis
$\mathbf{\Lambda}_B$, $\mathbf{\Lambda}_T$	Vector of nodal horizontal displacements and rotations around *y*-axis

$\boldsymbol{\Gamma}_B$, $\boldsymbol{\Gamma}_T$	Vector of nodal angle of twist and global warping